



# **NAVAL POSTGRADUATE SCHOOL**

**MONTEREY, CALIFORNIA**

## **DISSERTATION**

**WIRELESS SOURCE LOCALIZATION AND SIGNAL  
COLLECTION FROM AN AIRBORNE SYMMETRIC  
LINE ARRAY SENSOR NETWORK**

by

Tan A. Ngo

September 2014

Dissertation Co-Supervisors:

Murali Tummala  
John McEachen

**Approved for public release; distribution is unlimited**

THIS PAGE INTENTIONALLY LEFT BLANK

<b>REPORT DOCUMENTATION PAGE</b>			<i>Form Approved OMB No. 0704-0188</i>	
Public reporting burden for this collection of information is estimated to average 1 hour per response, including the time for reviewing instruction, searching existing data sources, gathering and maintaining the data needed, and completing and reviewing the collection of information. Send comments regarding this burden estimate or any other aspect of this collection of information, including suggestions for reducing this burden, to Washington headquarters Services, Directorate for Information Operations and Reports, 1215 Jefferson Davis Highway, Suite 1204, Arlington, VA 22202-4302, and to the Office of Management and Budget, Paperwork Reduction Project (0704-0188) Washington DC 20503.				
<b>1. AGENCY USE ONLY (Leave blank)</b>		<b>2. REPORT DATE</b> September 2014	<b>3. REPORT TYPE AND DATES COVERED</b> Dissertation	
<b>4. TITLE AND SUBTITLE</b> WIRELESS SOURCE LOCALIZATION AND SIGNAL COLLECTION FROM AN AIRBORNE SYMMETRIC LINE ARRAY SENSOR NETWORK			<b>5. FUNDING NUMBERS</b>	
<b>6. AUTHOR(S)</b> Tan A. Ngo				
<b>7. PERFORMING ORGANIZATION NAME(S) AND ADDRESS(ES)</b> Naval Postgraduate School Monterey, CA 93943-5000			<b>8. PERFORMING ORGANIZATION REPORT NUMBER</b>	
<b>9. SPONSORING /MONITORING AGENCY NAME(S) AND ADDRESS(ES)</b> N/A			<b>10. SPONSORING/MONITORING AGENCY REPORT NUMBER</b>	
<b>11. SUPPLEMENTARY NOTES</b> The views expressed in this dissertation are those of the author and do not reflect the official policy or position of the Department of Defense or the U.S. Government. IRB Protocol number ____N/A____.				
<b>12a. DISTRIBUTION / AVAILABILITY STATEMENT</b> Approved for public release; distribution is unlimited			<b>12b. DISTRIBUTION CODE</b>	
<b>13. ABSTRACT (maximum 200 words)</b>  Wireless communication technology has become a critical aspect in many civilian and military applications. With regard to remote sensing, search and rescue, disaster relief operations and signals intelligence, there exists an interest in developing capabilities to collect these signals-of-interest. The objective of this dissertation is to maximize signal collection performance in the presence of signal measurement and sensor related errors. To accomplish this objective, we proposed a signal collection scheme that exploits an elevated, mobile network to maximize the collaborative collection of a target signal.  The proposed scheme begins with source localization. This technique consists of an initial weighted least-squares estimate followed by a maximum-likelihood estimate. Implemented on an elevated, mobile network, this technique is able to obtain an optimal localization. To enhance localization robustness, we developed an outlier rejection process that mitigates the effects of measurement and sensor position errors.  To collect the signal, this research quantified the effects of sensor position errors on beamforming and proposed a novel signal collection scheme that combines signal estimation and collaborative beamforming. Using all these techniques in concert, we were able to show that the proposed scheme outperforms standard collaborative beamforming in the presence of sensor position errors.				
<b>14. SUBJECT TERMS</b> Source localization, TDOA, beamforming, signal estimation			<b>15. NUMBER OF PAGES</b> 153	
			<b>16. PRICE CODE</b>	
<b>17. SECURITY CLASSIFICATION OF REPORT</b> Unclassified	<b>18. SECURITY CLASSIFICATION OF THIS PAGE</b> Unclassified	<b>19. SECURITY CLASSIFICATION OF ABSTRACT</b> Unclassified	<b>20. LIMITATION OF ABSTRACT</b> UU	

THIS PAGE INTENTIONALLY LEFT BLANK

**Approved for public release; distribution is unlimited**

**WIRELESS SOURCE LOCALIZATION AND SIGNAL COLLECTION FROM  
AN AIRBORNE SYMMETRIC LINE ARRAY SENSOR NETWORK**

Tan A. Ngo

Captain, United States Air Force

B.S., California State Polytechnic University, Pomona, 2003

M.S., California State University, Long Beach, 2008

Submitted in partial fulfillment of the  
requirements for the degree of

**DOCTOR OF PHILOSOPHY IN ELECTRICAL ENGINEERING**

from the

**NAVAL POSTGRADUATE SCHOOL  
September 2014**

Author: Tan A. Ngo

Approved by:	John McEachen Professor of Electrical and Computer Engineering Dissertation Co-Advisor	Frank Kragh Associate Professor of Electrical and Computer Engineering
--------------	---	--

James Scrofani Associate Professor of Electrical and Computer Engineering	James Newman Professor, Space Systems Academic Group
---	--

Murali Tummala  
Professor of Electrical and Computer Engineering  
Dissertation Committee Chair  
and Dissertation Co-Advisor

Approved by: R. C. Robertson, Chair, Dept. of Electrical and Computer Engineering

Approved by: Douglas Moses, Vice Provost for Academic Affairs

THIS PAGE INTENTIONALLY LEFT BLANK

## ABSTRACT

Wireless communication technology has become a critical aspect in many civilian and military applications. With regard to remote sensing, search and rescue, disaster relief operations and signals intelligence, there exists an interest in developing capabilities to collect these signals-of-interest. The objective of this dissertation is to maximize signal collection performance in the presence of signal measurement and sensor related errors. To accomplish this objective, we proposed a signal collection scheme that exploits an elevated, mobile network to maximize the collaborative collection of a target signal.

The proposed scheme begins with source localization. This technique consists of an initial weighted least-squares estimate followed by a maximum-likelihood estimate. Implemented on an elevated, mobile network, this technique is able to obtain an optimal localization. To enhance localization robustness, we developed an outlier rejection process that mitigates the effects of measurement and sensor position errors.

To collect the signal, this research quantified the effects of sensor position errors on beamforming and proposed a novel signal collection scheme that combines signal estimation and collaborative beamforming. Using all these techniques in concert, we were able to show that the proposed scheme outperforms standard collaborative beamforming in the presence of sensor position errors.

THIS PAGE INTENTIONALLY LEFT BLANK

# TABLE OF CONTENTS

<b>I.</b>	<b>INTRODUCTION.....</b>	<b>1</b>
<b>A.</b>	<b>OBJECTIVE .....</b>	<b>2</b>
<b>B.</b>	<b>RELATED WORK.....</b>	<b>3</b>
<b>C.</b>	<b>ORGANIZATION .....</b>	<b>5</b>
<b>II.</b>	<b>BACKGROUND .....</b>	<b>7</b>
<b>A.</b>	<b>WIRELESS SENSOR NETWORKS .....</b>	<b>7</b>
1.	Ground-based, Stationary Wireless Sensor Network System Architecture.....	8
2.	Network Time Synchronization.....	9
3.	Elevated, Mobile Wireless Sensor Networks.....	10
4.	Multicopter UAV as an Elevated, Mobile WSN Sensor Node .....	11
a.	<i>Multicopter UAV Station Keeping.....</i>	<i>11</i>
<b>B.</b>	<b>HYPERBOLIC SOURCE LOCALIZATION .....</b>	<b>12</b>
1.	Weighted Least-Squares Estimation .....	14
2.	Maximum-Likelihood Estimation .....	15
3.	Optimal Formations for Source Localization.....	18
4.	The Airborne Symmetrical Line Array Network Configuration ..	21
5.	TDOA Outlier Measurement Diagnostics .....	22
<b>C.</b>	<b>BEAMFORMING.....</b>	<b>24</b>
1.	Phase Shift Beamforming.....	25
2.	Adaptive Beamforming .....	26
3.	Error Effects in Beamforming .....	30
4.	Sidelobe Control via Array Tapering .....	31
a.	<i>Tapering Methods for Uniform Linear Arrays.....</i>	<i>31</i>
b.	<i>Comparison of the Taper Methods.....</i>	<i>33</i>
5.	Grating Lobe Control via Virtual Filling .....	34
<b>III.</b>	<b>SOLUTION APPROACH.....</b>	<b>37</b>
<b>A.</b>	<b>PROPOSED SCHEME .....</b>	<b>37</b>
1.	Source Localization.....	39
2.	Sensor Node Position Error .....	40
3.	Collaborative Signal Collection .....	41
<b>B.</b>	<b>PERFORMANCE METRICS .....</b>	<b>42</b>
<b>IV.</b>	<b>ROBUST TWO-STAGE SOURCE LOCALIZATION FROM AN AIRBORNE SYMMETRIC LINE ARRAY NETWORK.....</b>	<b>45</b>
<b>A.</b>	<b>TWO-STAGE HYPERBOLIC LOCALIZATION .....</b>	<b>45</b>
1.	Hyperbolic Localization via Weighted Least-Squares .....	45
2.	Hyperbolic Localization via Maximum-Likelihood Estimation ....	48
<b>B.</b>	<b>LOCALIZATION PERFORMANCE .....</b>	<b>49</b>
1.	Performance of the Localization Scheme in the Presence of Uniform Position Errors.....	54
<b>C.</b>	<b>ROBUST SIGNAL LOCALIZATION VIA MEASUREMENT OUTLIER REJECTION.....</b>	<b>58</b>

1.	Robust Hyperbolic Localization via Measurement Outlier Rejection .....	58
a.	Measurement Outlier Rejection via the Mahalanobis Distance .....	58
b.	Distribution of the Mahalanobis Distance .....	59
c.	Outlier Rejection Threshold .....	61
2.	Performance of the Robust Localization in the Presence of Measurement Outliers .....	62
D.	PERFORMANCE OF THE ROBUST LOCALIZATION IN THE PRESENCES OF MEASUREMENT OUTLIERS AND UNIFORM POSITION ERRORS .....	68
V.	ROBUST SIGNAL COLLECTION FROM AN AIRBORNE SEMI-STATIONARY NETWORK.....	71
A.	EFFECTS OF UNIFORM POSITION ERROR ON THE ARRAY FACTOR.....	71
1.	Effects of Uniform Position Error in the Special Case when the ASLA Formation Is Normal to the Target Source .....	74
2.	Simulation Results on the Effects of Uniform Position Errors on the Array Factor .....	75
B.	EFFECTS OF GAUSSIAN POSITION ERROR ON THE ARRAY FACTOR.....	77
1.	Simulation Results of the Effects of Gaussian Position Errors on the Array Factor .....	79
C.	SIGNAL COLLECTION FROM AIRBORNE SYMMETRIC LINE ARRAY NETWORK IN THE PRESENCE OF UNIFORM POSITION ERRORS .....	80
1.	Signal Collection in the Presence of Thermal Noise and Uniform Sensor Position Error.....	88
D.	SIGNAL COLLECTION FROM AIRBORNE SYMMETRIC LINE ARRAY NETWORK IN THE PRESENCE OF GAUSSIAN POSITION ERROR.....	93
1.	Mean Value of the In-Phase and Quadrature Components with Gaussian Position Errors .....	96
2.	Phase Estimates Using Sampled Base Band Signals.....	98
3.	Performance of the Signal Collection Scheme in the Presence of Gaussian Sensor Position Errors.....	99
E.	GRATING LOBE SUPPRESSION VIA VIRTUAL FILLING .....	103
VI.	CONCLUSION .....	109
A.	SIGNIFICANT CONTRIBUTIONS.....	110
B.	FUTURE RESEARCH.....	111
	APPENDIX. SELECTED SIMULATION CODE.....	113
	LIST OF REFERENCES.....	121
	INITIAL DISTRIBUTION LIST .....	129

## LIST OF FIGURES

Figure 1.	Wireless sensor network concept.....	8
Figure 2.	Key components of a sensor node. ....	9
Figure 3.	Simulated quadrotor station keeping in the presence of Dryden modeled wind, a) UAV three-dimensional (3D) motion, b) histogram of two-dimensional (2D) position errors, from [48].....	12
Figure 4.	Iterative performance of a hyperbolic maximum-likelihood estimator in the presence of an inaccurate $\omega_r$ estimate. ....	17
Figure 5.	Optimum array geometries for position estimation (minimum uncertainty area) using TDOA localization. $J$ = number of sensor groups, $M$ = total number of sensor, from [17]. ....	20
Figure 6.	Illustration of the ASLA formation.....	21
Figure 7.	Accuracy of position estimate for fixed linear formation (blue) and fixed circular formation (red).....	22
Figure 8.	Scatter plot of 200 hyperbolic location estimates. ....	23
Figure 9.	Plane wave impinging on a uniform linear array.....	24
Figure 10.	Array factor of a 15 isotropic node linear array with $d = \lambda / 2$ . ....	26
Figure 11.	Transmitted signal-of-interest. ....	28
Figure 12.	Response of 15 node phase shift beamformer with two 10 dB interfering signals at DOA of 30 and 50 degrees.....	29
Figure 13.	Output signal of the MVDR beamformer in the presence of a target signal at $\theta_t = 45\text{deg}$ and two interfering signals at $\theta_i = 30$ and $50\text{ deg}$ . ....	29
Figure 14.	Comparison between the MVDR and phase shift beamformers in the presence of a target signal at $\theta_t = 45\text{deg}$ and two interfering signals at $\theta_i = 30$ and $50\text{ deg}$ . ....	30
Figure 15.	Beam width and sidelobe level tradeoff for four different tapering methods using a 15 node ULA. The beamwidth $-3\text{ dB}$ line is shown in red, from [70]. ....	34
Figure 16.	Operational concept of an elevated, mobile sensor network deployed in an ASLA formation. ....	38
Figure 17.	Process flow for propose signal collection scheme. ....	39
Figure 18.	Network reorientation operation for the two-stage localization technique.....	40
Figure 19.	Root mean-square error $\xi_{loc}$ of the initial (black) and refined (red) localizations versus RDOA noise. Result based on 10,000 trials, $N_s = 5$ , $r_a = 200\text{ m}$ , and $\omega_t = [2500\text{ m}, 45\text{ deg}]^T$ . ....	50
Figure 20.	RMSE $\xi_\theta$ of the initial (black) and refined (red) localizations versus RDOA noise. Result based on 10,000 trials, $N_s = 5$ , $r_a = 200\text{ m}$ , and $\omega_t = [2500\text{ m}, 45\text{ deg}]^T$ . ....	51

Figure 21.	Root mean-square error $\xi_{loc}$ of the initial (black) and refined (red) localizations versus $N_s$ . Results based on 10,000 trials with $\sigma_{RD}^2 = 0$ dB, $N_s = 5$ , $r_a = 200$ m, and $\omega_t = [2000 \text{ m}, 30 \text{ deg}]^T$ . ....	52
Figure 22.	Root mean-square error $\xi_\theta$ of the initial (black) and refined (red) localizations versus $N_s$ . Results based on 10,000 trials with $\sigma_{RD}^2 = 0$ dB, $N_s = 5$ , $r_a = 200$ m, and $\omega_t = [2000 \text{ m}, 30 \text{ deg}]^T$ . ....	53
Figure 23.	Root mean-square error $\xi_{loc}$ of the initial (o) and refined (*) localizations versus $\theta_t$ . Results based on 10,000 trials with $\sigma_{RD}^2 = 0$ dB, $N_s = 5$ , $r_a = 200$ m, and $r_t = 2000$ m. ....	54
Figure 24.	Initial localization's root mean-square error $\xi_{loc}$ with no position errors (black) and with position errors (red) versus maximum uniform position error $\delta_p$ . Results based on 10,000 trials with $\sigma_{RD}^2 = 0$ dB, $N_s = 5$ , $r_a = 200$ m, and $\omega_t = [2000 \text{ m}, 30 \text{ deg}]^T$ . ....	55
Figure 25.	Initial localization's root mean-square error $\xi_\theta$ with no position errors (black) and with position errors (red) versus maximum uniform position error $\delta_p$ . Results based on 10,000 trials with $\sigma_{RD}^2 = 0$ dB, $N_s = 5$ , $r_a = 200$ m, and $\omega_t = [2000 \text{ m}, 30 \text{ deg}]^T$ . ....	56
Figure 26.	Refined localization's root mean-square error $\xi_{loc}$ with no position errors (black) and with position errors (red) versus maximum uniform position error $\delta_p$ . Results based on 10,000 trials with $\sigma_{RD}^2 = 0$ dB, $N_s = 5$ , $r_a = 200$ m, and $\omega_t = [2000 \text{ m}, 30 \text{ deg}]^T$ . ....	57
Figure 27.	Refined localization's root mean-square error $\xi_\theta$ with no position errors (black) and with position errors (red) versus maximum uniform position error $\delta_p$ . Results based on 10,000 trials with $\sigma_{RD}^2 = 0$ dB, $N_s = 5$ , $r_a = 200$ m, and $\omega_t = [2000 \text{ m}, 30 \text{ deg}]^T$ . ....	57
Figure 28.	Comparison of histogram and Chi-squared probability density function of Mahalanobis distances. ....	61
Figure 29.	Root mean-square error $\xi_{loc}$ of the weighted least-squares (red) and robust weighted least-squares (blue) versus RDOA noise variance. No outliers. Results based on 10,000 trials with $N_s = 5$ , $r_a = 200$ m, and $\omega_t = [2000 \text{ m}, 30 \text{ deg}]^T$ . ....	63
Figure 30.	Root mean-square error $\xi_{loc}$ of the weighted least-squares estimator with outliers (red), weighted least-squares estimator without outliers (black), and robust weighted least-squares estimator with outliers (blue) versus RDOA noise variance. Results based on 10,000 trials with $N_s = 5$ , ....	

	$r_a = 200$ m, and $\omega_t = [2000 \text{ m}, 30 \text{ deg}]^T$ . In the outlier cases there were two random outliers present at a RDOA noise variance five times $\sigma_{RD}^2$ .....64
Figure 31.	Root mean-square error $\xi_{loc}$ of the weighted least-squares estimator with outliers (red), weighted least-squares estimator without outliers (black), and robust weighted least-squares estimator with outliers (blue) versus number of outliers. Results based on 10,000 trials with $N_s = 5$ , $r_a = 200$ m, and $\omega_t = [2000 \text{ m}, 30 \text{ deg}]^T$ . In the outlier cases their RDOA noise variance is five times $\sigma_{RD}^2$ .....65
Figure 32.	Root mean-square error $\xi_{loc}$ of the weighted least-squares estimator with outliers (red), weighted least-squares estimator without outliers (black), and robust weighted least-squares estimator with outliers (blue) versus RDOA noise gain. Results based on 10,000 trials with $N_s = 5$ , $r_a = 200$ m, and $\omega_t = [2000 \text{ m}, 30 \text{ deg}]^T$ . In the outlier cases there were 2 random outliers present.....66
Figure 33.	Root mean-square error $\xi_{loc}$ of the weighted least-squares estimator (circle) and robust weighted least-squares estimator (diamond) versus $\theta_t$ . Results based on 3,000 trials with $\sigma_{RD}^2 = 0$ dB, $N_s = 5$ , $r_a = 200$ m, and $r_t = 2000$ m. In both cases there were 2 random outliers present at a RDOA noise variance five times $\sigma_{RD}^2$ .....67
Figure 34.	Root mean-square error $\xi_{loc}$ of the weighted least-squares estimate (red) and robust weighted least-squares estimate (blue) versus $\delta_p$ . For comparison the no error case is shown in black. Results based on 10,000 trials with $\sigma_{RD}^2 = 0$ dB, $N_s = 5$ , $r_a = 200$ m, and $\omega_t = [2000 \text{ m}, 30 \text{ deg}]^T$ .....68
Figure 35.	Root mean-square error $\xi_{loc}$ of the weighted least-squares estimate (red) and robust weighted least-squares estimate (blue) versus $\delta_p$ . For comparison the no error case is shown in black. Results based on 10,000 trials with $\sigma_{RD}^2 = 0$ dB, $N_s = 5$ , $r_a = 200$ m, and $\omega_t = [2000 \text{ m}, 30 \text{ deg}]^T$ .....69
Figure 36.	Mean normalized main beam gain of an $N_s = 5$ ASLA versus $\delta_p$ . Results based on 1,000 trials with $r_a = 200$ m, and $\theta_t = 45 \text{ deg}$ .....75
Figure 37.	Variance of the normalized main beam gain for $N_s = 5$ ASLA versus $\delta_p$ . Results based on 1,000 trials with $r_a = 200$ m, and $\theta_t = 45 \text{ deg}$ .....76
Figure 38.	Average $\psi_\varepsilon$ for an $N_s = 5$ ASLA versus $\delta_p$ . Results based on 1,000 trials with $\lambda = 1$ , $r_a = 200$ m, and $\theta_t = 45 \text{ deg}$ .....77

Figure 39.	Normalized values of magnitude $\{\mu_{MB}\}$ versus position error variance $\sigma_g^2 = (\beta\sigma_p)^2$ . In this simulation $N_s = 30$ , $\theta_t = 0\text{deg}$ , $\lambda = 1$ , $r_a = 200\text{ m}$ , and all data points are the result of 1,000 trials. ....	79
Figure 40.	Values of angle $\{\mu_{MB}\}$ versus position error variance $\sigma_g^2 = (\beta\sigma_p)^2$ . In this simulation $N_s = 30$ , $\theta_t = 0\text{deg}$ , $\lambda = 1$ , $r_a = 200\text{ m}$ , and all data points are the result of 1,000 trials. ....	80
Figure 41.	Root mean-square error $\xi_v$ at different levels of RDOA noise versus SNR per node. Results based on 10,000 trials with $N_s = 10$ , $r_a = 200\text{ m}$ , $\delta_p = .05\text{ m}$ , and $\omega_t = [2000\text{ m}, 45\text{ deg}]^T$ .....	89
Figure 42.	Root mean-square error $\xi_\phi$ at different levels of RDOA noise versus SNR per node. Results based on 10,000 trials with $N_s = 10$ , $r_a = 200\text{ m}$ , $\delta_p = .05\text{ m}$ , and $\omega_t = [2000\text{ m}, 45\text{ deg}]^T$ .....	89
Figure 43.	Root mean-square error $\xi_\phi$ at different levels of RDOA noise under increase maxed uniform position error $\delta_p$ . Results based on 10,000 trials with, $N_s = 10$ , $r_a = 200\text{ m}$ , SNR = 5 dB, and $\omega_t = [2000\text{ m}, 45\text{ deg}]^T$ .....	90
Figure 44.	Root mean-square error $\xi_\phi$ at different levels of RDOA noise under increase maxed uniform position error $N_s$ . Results based on 10,000 trials with, $\delta_p = 1/10\text{ m}$ , $r_a = 200\text{ m}$ , SNR = 5 dB, and $\omega_t = [2000\text{ m}, 45\text{ deg}]^T$ ...	90
Figure 45.	Signal $\xi_v$ of proposed scheme compared with the no-estimation case versus SNR per node values. Results based on 10,000 trials with $\delta_p = 1/10\text{ m}$ , $r_a = 200\text{ m}$ , and $\omega_t = [2000\text{ m}, 45\text{ deg}]^T$ .....	91
Figure 46.	Average signal normalized gain at different levels of RDOA noise versus signal frequencies. Results based on 10,000 trials with $\sigma_{RD}^2 = 0\text{ dB}$ , $\delta_p = 1/10\text{ m}$ , $r_a = 200\text{ m}$ , and $\omega_t = [2000\text{ m}, 45\text{ deg}]^T$ .....	92
Figure 47.	Comparison of measured and theoretical probability density function (pdf) of $n_{C_i}$ . Signal phase $\phi_t = 0$ and measured pdf based on histogram using 10,000 points and 50 bins. ....	95
Figure 48.	Root mean-square error of normalize magnitude versus the standard deviation of Gaussian position error $\sigma_g$ . Results based on 10,000 trials with $N_s = 10$ , $r_a = 200\text{ m}$ , and $\omega_t = [2000\text{ m}, 15\text{ deg}]^T$ .....	100
Figure 49.	Root mean-square error phase $\xi_\phi$ versus the standard deviation of Gaussian position error $\sigma_g$ . Results based on 10,000 trials with $N_s = 10$ , $r_a = 200\text{ m}$ , and $\omega_t = [2000\text{ m}, 15\text{ deg}]^T$ .....	101

Figure 50.	Root mean-square error of normalize magnitude versus RDOA noise. Results based on 10,000 trials with, $N_s=10$ , $r_a=200$ m, and $\omega_t=[2000 \text{ m}, 15 \text{ deg}]^T$ .....	102
Figure 51.	Root mean-square error Phase $\xi_\phi$ versus RDOA noise. Results based on 10,000 trials with, $N_s=10$ , $r_a=200$ m, and $\omega_t=[2000 \text{ m}, 15 \text{ deg}]^T$ . .....	103
Figure 52.	Normalized Array factor of an $N_s=5$ ASLA phase shift beamformer before virtual filling process. Simulation based on $r_a=200$ m, and $\omega_t=[2000 \text{ m}, 45 \text{ deg}]^T$ .....	105
Figure 53.	Normalized Array factor of an $N_s=5$ ASLA phase shift beamformer with virtual filling process with binomial tapering. Simulation based on, $r_a=200$ m, and $\omega_t=[2000 \text{ m}, 45 \text{ deg}]^T$ . .....	105
Figure 54.	Signal Estimation without virtual filling. Simulation based on, $r_a=100$ m, target signal's $\theta_t=0 \text{ deg}$ , $V_s=1$ , and $\phi_s=60 \text{ deg}$ . The interfering signal's $\theta_t=55 \text{ deg}$ , $V_s=1$ , and $\phi_s=25 \text{ deg}$ . The true signal phase and magnitude is shown in red. ....	106
Figure 55.	Signal estimation with virtual filling. Simulation based on, $r_a=100$ m, target signal's $\theta_t=0 \text{ deg}$ , $V_s=1$ , and $\phi_s=60 \text{ deg}$ . The interfering signal's $\theta_t=55 \text{ deg}$ , $V_s=1$ , and $\phi_s=25 \text{ deg}$ . The true signal phase and magnitude is shown in red. ....	107
Figure 56.	Proposed scheme's $\xi_\phi$ with virtual filling (blue) and without (black) versus maximum uniform position error $\delta_p$ in the presence of one interfering signal. In this simulation, $r_a=100$ m, the target signal's $\theta_t=0 \text{ deg}$ , $V_t=1$ , and $\phi_t=60 \text{ deg}$ , the interfering signal's $\theta_t=55 \text{ deg}$ , $V_t=1$ , and $\phi_t=25 \text{ deg}$ , and all data points are the result of 1,000 trials.....	108

THIS PAGE INTENTIONALLY LEFT BLANK

## LIST OF ACRONYMS AND ABBREVIATIONS

ASLA	airborne symmetric line array
AWGN	additive white Gaussian noise
BPSK	binary phase-shift keying
CRLB	Cramer-Rao lower bound
dB	decibel
DOA	direction-of-arrival
GDOP	geometric dilution of precision
MVDR	minimum variance distortionless response
QPSK	quadrature phase-shift keying
RDOA	range difference-of-arrival
RMSE	root mean-squared error
SNR	signal-to-noise ratio
TDOA	time-difference-of-arrival
TOA	time-of-arrival
UAV	unmanned aerial vehicle
WSN	wireless sensor networks

THIS PAGE INTENTIONALLY LEFT BLANK

## EXECUTIVE SUMMARY

Wireless communication technology has penetrated many aspects of both civilian and military applications. With cellular technology constantly evolving and proliferating, we now see wireless communications as an integral part of daily life. With regard to remote sensing, search and rescue, disaster relief operations and signals intelligence, there exists an interest in developing capabilities to collect these signals. The objective of this dissertation is to maximize signal collection performance in the presence of various signal- and sensor-related errors. To accomplish this objective, we proposed a signal collection scheme that exploits an elevated, mobile network to maximize the collaborative collection of a target signal.

With its roots dating back to the development of radar during World War II, beamforming has found a prominent place in modern wireless communications. In its classical use, through the manipulation of array weights, beamforming coherently amplifies a signal in a given direction, while reducing undesirable signals in others. Although, beamforming is a powerful technique that enables spatial filtering, it has a strong dependence on the *a priori* knowledge of the target signal's direction of arrival [1]. Because of this dependency, beamforming is often initialized by source localization.

Our proposed scheme begins with a source localization technique; this technique is used to determine the signal's position and direction of arrival. This knowledge is then used by a collaborative beamformer to maximize and collect the target signal. Both of these techniques are enhanced through the use of an elevated, mobile network. This mobility allows for the reconfiguration of the sensor network's topology to create an ideal sensor-target geometry. This geometry minimizes any geometric dilutions of precision, thus allowing for an optimal location estimate to be achieved [2]. The network's elevation increases signal power and range while enabling unique sensor formations for signal collection that is robust against sensor position errors.

The proposed scheme begins with a localization technique. In this localization, we propose a two-stage technique capable of obtaining an accurate localization in the

presence of signal noise and sensor position errors. This technique consists of an initial weighted least-squares estimate followed by a refining maximum-likelihood estimate. Here, the initial estimate is used to reconfigure the network's topology. This reconfiguration is used to create an optimal sensor network to target geometry, thus creating the necessary conditions for the refining estimation to deliver an optimal location estimate. Our simulation results show the proposed localization technique to be efficient, i.e., it approaches the Cramer-Rao lower bound in the small error region [2].

To enhance the localization performance, we developed a measurement outlier rejection process to mitigate the effects of measurement and sensor position errors. This technique uses a combination of single case diagnostics and the Mahalanobis distance to identify and remove specious measurements for the least-squares estimate [3]. Through simulation, we demonstrated this technique to be effective in the presence of both measurement and position errors.

To develop the proposed signal collection scheme, we began by analyzing the effects of sensor position errors on the array factor. We derived an expression for the effects of position error on the array's main beam gain. Through simulation, we validated our results and showed that the mean value of the main beam signal phase was unaffected by position errors. To enhance the collection performance in the presence of these errors, we developed a signal estimator for both uniform and Gaussian position errors. Our simulation results showed a maximum improvement in array gain of approximately 37 percent for the standard deviation of position error values greater than 0.4 m. Other results demonstrated that our approach of combining a signal estimation technique with collaborative beamforming is a viable means of collecting a target signal from an elevated, mobile wireless sensor network.

Taking advantage of the concept of a unique elevated, mobile wireless sensor network realized through the use of multirotor UAVs, our scheme used two existing localization techniques to deliver a precise source location estimate. Using this information with statistical knowledge of the sensor position errors in a signal estimator, we were able to derive a novel collaborative signal collection scheme. This scheme was shown to be capable of collecting and amplifying a target signal in the presence of such

errors. With all these techniques in concert, the objective of this dissertation to maximize signal collection performance in the presence of various signal- and sensor-related errors was achieved.

## LIST OF REFERENCES

- [1] B. D. Steinberg, *Principles of Aperture and Array System Design*, New York: John Wiley and Sons, 1976.
- [2] K. C. Ho and L. M. Vicente, "Sensor allocation for source localization with decoupled range and bearing estimation," *IEEE Trans. Signal Process.*, vol. 56, no. 12, pp. 5773–5789, Dec. 2008.
- [3] P. J. Rousseeuw and A. M. Leroy, *Robust Regression and Outlier Detection*, New York: John Wiley and Sons, 1987.

THIS PAGE INTENTIONALLY LEFT BLANK

## **ACKNOWLEDGMENTS**

I would like to sincerely thank my wife, Claire; it was your enduring support and love that has sustained me through this challenging dissertation process.

To my parents, Trinh and Yen Ngo, I am forever grateful. If not for your lifetime of care and support, I would not be the man I am today.

I would also like to express my sincere gratitude to my advisor, Professor Tummala. It was the foundation you helped me build that allowed me to weather the storm that is the PhD program, and without your mentorship, I would simply be lost in a virtual forest of my own design. To my committee members: Professor Murali Tummala, Professor John McEachen, Professor Frank Kragh, Professor James Scrofani, and Professor James Newman, your insights and guidance for this dissertation were invaluable, and for that I am very grateful.

THIS PAGE INTENTIONALLY LEFT BLANK

## I. INTRODUCTION

Wireless communication technology has penetrated many aspects of both civilian and military applications. The International Telecommunications Union (ITU) estimates that there are approximately seven billion cellular subscribers worldwide [1]. This translates to a global penetration rate of 95.5 percent and is expected to increase each year. Clearly, wireless communications has become a common aspect of human life. With regard to remote sensing, search and rescue, disaster relief operations and/or signals intelligence, there exists an interest in developing capabilities to collect these signals. One such solution is collaborative beamforming [2].

With its roots dating back to the development of radar during World War II, beamforming has found a prominent place in modern wireless communications. Beamforming is much akin to the matched filter but from a spatial perspective [3]. Instead of linearly weighting a time domain signal for signal filtering, a beamformer linearly weights spatial array data for spatial filtering. In its classical use, beamforming coherently amplifies a signal in a given direction while reducing undesirable signals in other directions. Although beamforming is a powerful technique that enables spatial filtering, it has a strong dependence on *a priori* knowledge of the target signal's direction of arrival [4]. Because of this sensitivity, beamforming is often preceded by a direction of arrival estimation phase.

With regard to direction-of-arrival estimates, hyperbolic localization [5] has appealing qualities of interest to this research. Of particular interest is hyperbolic localization performed from an elevated, mobile wireless sensor network (WSN). The term hyperbolic is used to denote the use of signal time-difference-of-arrival measurement and calculations. The network is elevated to promote a line-of-sight communication link for better range and reliability, while the mobility allows for the reconfiguration of sensor-target geometries for more precise direction-of-arrival estimates.

The extension of beamforming to wireless sensor networks has given rise to the concept of collaborative beamforming. Here, a fully synchronized network of sensors is used to coherently collect and combine multiple received signals. These signals along with network topology information are used to form a distributed beamforming array. This technique coupled with recent advances in micro sensor and multirotor unmanned aerial vehicle (UAV) technologies has led to the concept of a semi-stationary airborne sensor network. Such a network is capable of providing both the elevation and mobility needed for highly accurate hyperbolic localization while providing a suitable network platform for collaborative signal collection.

## **A. OBJECTIVE**

The dissertation objective is to maximize signal collection performance in the presence of various signal and sensor related errors. To accomplish this task, we propose a new scheme for signal collection that is preceded by a localization phase.

To improve the scheme's localization accuracy, we propose the use of an optimally positioned two-stage localization technique. This technique consists of an initial weighted least-squares estimate followed by a refined maximum-likelihood estimate. Here, the initial estimate is used to reconfigure the network's topology, thereby creating an optimally configured network to obtain the refined hyperbolic estimate. To combat the effects of noise, we propose the use of measurement outlier diagnostics in concert with the two-stage technique. Here, we postulate that the identification and removal of specious time-difference-of-arrival measurements will improve the robustness of localization in the presence of noise.

To maximize the signal collection performance in the presence of noise, we propose the use of signal estimation in conjunction with collaborative beamforming. Using the concept of sensor stacks with knowledge of the sensor positional error statistics, we can derive a signal estimator to combat the effects of sensor position errors. To further enhance the collection capability for noise and interference rejection, we also propose the use of virtual filling to increase the array's ability to reject interfering signals.

## B. RELATED WORK

Beamforming has been shown to be an effective method for signal collection and interference rejection [6], but it has been shown to be highly susceptible to array steering vector errors [7]. This is when an array steering vector is not in line with that of the target signal. To make beamforming more robust against these array mismatch errors, Ahmed and Evans [8] suggest the use of inequality constraints on the array weights while Er and Cantoni [9] suggest the use of derivative constraints. Both of these approaches, although effective, also decrease the array's interference rejection capabilities. Li, Stoica and Wang [10] developed a robust beamformer that minimized the effects of non-random steering errors using a diagonal loading method. Lee and Lee [11] proposed a robust beamformer for signal collection, which minimizes a cost function based on received signal data and knowledge of steering error statistics. The signal collection scheme proposed in this research uses elevated, mobile sensor network formations and signal estimation in the context of collaborative beamforming. Preceded by a localization phase that creates a unique sensor network-to-target formation, the scheme is able to isolate the effects of phase perturbations due to position errors. It then compensates for them through the use of sensor formations, signal estimation, and knowledge of sensor position error statistics. Unlike the schemes of Ahmed and Evans [8] and Er and Cantoni [9], our scheme does not require any constraints on the beamformer weights. Similar to that of Lee and Lee [11], our scheme utilizes sampled array data and knowledge of error statistics to compensate for array phase errors. The difference being that our scheme uses the sampled data in a signal estimation context with consideration to array formation rather than an array weight optimization problem with no consideration to array formation.

One of the earliest hyperbolic location systems was investigated by Carson [12] in 1972. He proposed a system of hydrophones to collect signal arrival times, with a goal to estimate the location of subsurface acoustic emitters. Today, numerous extensions and breakthroughs have been made to adapt these concepts for radio frequency (RF) signals. Fang [13] provides a closed form solution, but the estimator is not efficient, i.e., it does not achieve the Cramer-Rao lower bound [14], [15]. Hahn and Tretter [16] used the

hyperbolic equations in a maximum-likelihood estimation scheme that is unbiased and asymptotically efficient. Being a linearized system of non-linear equations, the maximum-likelihood estimator requires an initial reference estimate to avoid local minima. Chan and Ho [5] propose a weighted least-squares approach that yields an efficient estimator in the small error region. Our approach will combine the maximum-likelihood estimate of Hahn and Tretter [16] and the weighted least-squares estimate of Chan and Ho [5] to create a two-stage localization technique. Furthermore, this technique will use optimal sensor network formations as outlined by Ho and Vicente [17]. This combination of hyperbolic estimation and optimal sensor network formations will be used to provide highly accurate localization from an elevated, mobile WSN platform.

Rousseeuw and Leroy [18] provided the first comprehensive review of robust estimation and the effects of statistical outlier measurements. Key contributions by Mahalanobis [19] and Cook [20] helped quantify the effects of outliers in estimation by defining the Mahalanobis and Cook distance. Picard and Weiss [21] coupled these findings with the concept of sparse representation to derive a bound on the number of outliers that can be identified in a hyperbolic localization problem. Many researchers have contributed techniques to combat the effects of outlier measurements. McGuire, Plataniotis and Venetsanopoulos [22] proposed the use of data fusion techniques. Yang, Wang and Luo [23] showed that convex relaxation methods can be used to overcome outliers induced by both measurement noise and sensor position errors. Choi, et al. [24] used recursive filtering to deal with errors from incorrect stochastic information in location estimators. With the proposed localization technique implemented on an elevated, mobile sensor network, there will be increased measurement noise due to sensor position errors. To minimize the effects of these errors as well as measurement outliers, we propose an outlier rejection process based on single case diagnostics [18] and the squared-Mahalanobis distance [19]. Overall, a robust localization scheme that combines the proposed two-stage localization technique and the outlier rejection process is achieved.

## C. ORGANIZATION

This dissertation is organized as follows.

The fundamental principles involved with hyperbolic localization and beamforming is the focus of Chapter II. Localization based on the time-difference-of-arrival measurements, weighted least-squares estimator, maximum-likelihood estimator, and robust signal outlier detection techniques are discussed in the localization section. With collaborative signal collection as the end goal, we also provide an introduction to beamforming and its extension to collaborative beamforming.

The proposed two-phase scheme is presented in Chapter III. This includes a description of the scheme's process flow as it moves through the two phases of localization and collection. A discussion of the deployment and operating concepts is provided to give context to the proposed scheme. The many figures of merit used to evaluate the scheme's performance are also detailed.

The detailed analysis in support of the robust localization phase of our scheme is included in Chapter IV. Additional robust signal processing techniques that are implemented in both estimators to combat the effects of measurement outliers and sensor position errors are also included. The performance of the robust localization phase is then examined using simulation.

The signal collection phase of the proposed scheme is described in Chapter V. This includes an analysis of sensor position errors and their effects on an array's array factor. Based on these findings, we derive a novel signal estimator to combat the effects of uniform and Gaussian sensor position errors. The performance of the resulting collection scheme is then investigated using simulation.

In conclusion, a summary of the dissertation, a discussion of the research's significant contributions, and a list of potential future research topics are given in Chapter VI. An appendix is also included, which contains selected MATLAB simulation scripts.

THIS PAGE INTENTIONALLY LEFT BLANK

## II. BACKGROUND

To perform signal collection, we must understand the different processes involved in source localization and collection. In this section, we provide the necessary background material to properly present our research and results. We begin with a brief discussion on WSN that forms the basis of the proposed signal collection scheme. With the premise of sensor networks explored, we discuss the principles of hyperbolic/TDOA source localization and collaborative beamforming.

Throughout the dissertation, the following notation is used. Bold lower-case font indicates a vector, while bold upper-case font indicates a matrix,  $\Pr(*)$  indicates the probability of an event,  $E\{*\}$  indicates the expected value,  $(*)^T$  indicates the transpose operation,  $(*)^H$  indicates the Hermitian transpose operation,  $\|*\|$  indicates the 2-norm operation,  $\mathbf{I}$  is the identity matrix,  $\mathbf{1}_i$  indicates a column vector of length  $i$ ,  $\text{tr}(*)$  indicates the trace of a matrix,  $j$  indicates an imaginary quantity,  $c$  is the signal propagation speed, and  $\lambda$  is the signal wavelength.

### A. WIRELESS SENSOR NETWORKS

Advances in wireless communications coupled with low cost multifunctional sensors have given rise to the growth of WSNs. A WSN is a network comprised of many sensor nodes deployed in or near a phenomenon to be observed. Typical implementations have identical sensor nodes collecting data and routing it through a shared channel to a sink node for processing/storage. An illustration of this concept is shown in Figure 1. Often, the deployment mechanisms are not predetermined, thus requiring arbitrary deployment schemes in inaccessible locations. The sensor network nodes collaborate to achieve a common goal. Some examples of this collaboration can be found in [25]. For example, sensor nodes can be distributed across a geographic region to monitor rainfall to support flood predictions, covert sensors could be deployed along known supply lines to monitor enemy troop movements, or RFID sensors could be

deployed throughout a warehouse for inventory control [25]. A few other notable research areas where WSNs have been applied are environmental monitoring [26], military applications such as acoustic detection of helicopters and chemical weapons detection [27], and logistical applications such as global shipment tracking [28].

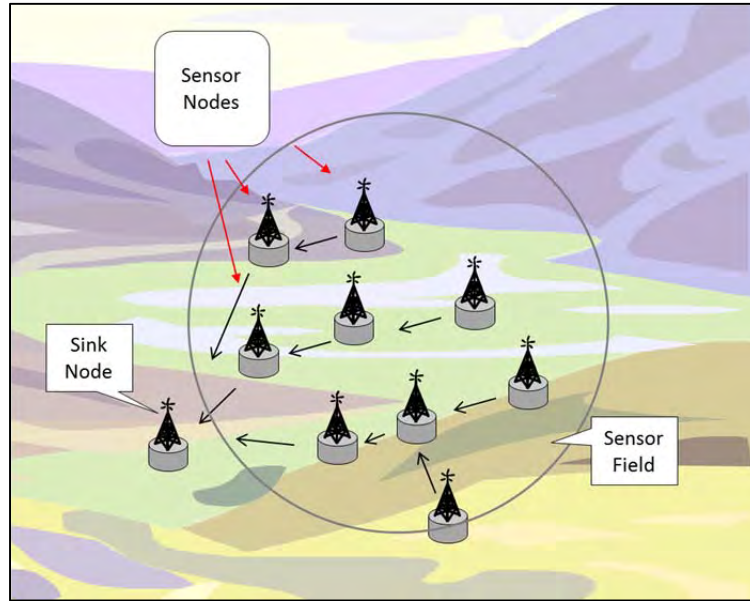


Figure 1. Wireless sensor network concept.

## 1. Ground-based, Stationary Wireless Sensor Network System Architecture

Sensor networks have many benefits, but the realization of an actual network can be complex with many design factors to consider. Some key factors are fault tolerance, scalability, production cost, hardware constraints, sensor network topology, operating environment, transmission media, power consumption, and protocol stack [29].

A major aspect of WSNs is the hardware components of each sensor node. A typical sensor node has four basic components: a sensor, processor, transceiver, and power source. There can also be some application dependent components, such as localization, power, and mobility systems. Each system plays a key role in this body of research. The key components of such a sensor node are shown in Figure 2.

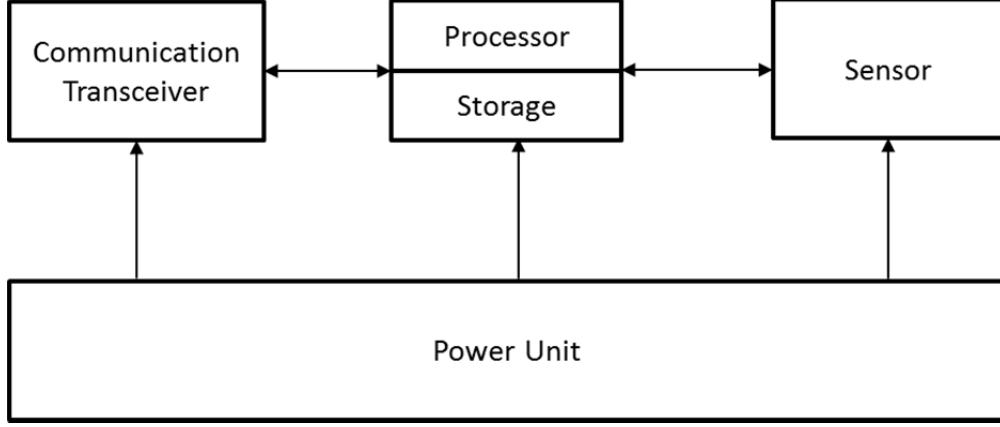


Figure 2. Key components of a sensor node.

## 2. Network Time Synchronization

Clock synchronization is an underlying requirement for many WSN applications. A key support function, time synchronization is vital to such applications as data fusion, transmission time synchronization, time-based channel scheduling, and node sleep/wake scheduling [30]. Most studies on clock synchronization have revolved around protocol design [31], but at its core clock synchronization is a parameter estimation problem, thus meriting a signal processing approach. The clock in each WSN node can be defined as

$$c(t) = t, \quad (1)$$

where  $t$  is the ideal reference time. Realistic systems deviate from the ideal clock due to imperfect clock oscillators, resulting in the general clock function

$$c(t) = s_c t + o_c, \quad (2)$$

where  $s_c$  is the clock skew and  $o_c$  is the offset. From (2), we can see that if not addressed, clock error can grow linearly over time. For example, a typical crystal-quartz oscillator commonly used in WSNs can have frequencies that vary up to 40 ppm, causing potential clock errors up to  $\pm 40 \mu s$  per second [30]. Although, clock synchronization is

a concern in many WSN applications, this research does not address this problem and assumes perfect synchronization across the network.

### 3. Elevated, Mobile Wireless Sensor Networks

It is well known that placing a received antenna on an elevated platform improves signal reception. By elevating the antenna, the communication link is less likely to be obstructed while promoting a line-of-sight signal path. From [32], the received power at an antenna over a reflective surface can be expressed as

$$P_r = \left[ \frac{h_r h_t}{d^2} \right]^2 \frac{G_r G_t}{L_0} P_t, \quad (3)$$

where  $P_t$  is the transmitted power,  $h_r$  is the receiver antenna height,  $h_t$  is the transmitter's antenna height,  $d$  is the distance,  $G_r$  is the gain of the receive antenna,  $G_t$  is the gain of the transmit antenna, and  $L_0$  is other associated losses. From this expression, we can see that an increase in receiver or transmitter height significantly decreases the signal path loss, i.e., increases the ratio of  $P_r$  to  $P_t$ . For example, given a scenario in which  $h_r = h_t = 2$  m,  $G_r = G_t = L_0 = 0$  dB and  $d = 5000$  m, the resulting path loss is 136 dB. By increasing both  $h_r$  and  $h_t$  to 100 m, the path loss is decreased to 68 dB.

Mobility in sensor networks has many advantages with regard to source localization and collection. In this research, it is not the velocity of a node that is important but its ability to reposition and maintain position. For example, in collaborative beamforming, a mobile sensor network can be reconfigured to achieve a desirable array factor [2], [33]. In hyperbolic localization, a sensor network can be reconfigured to obtain optimal sensor to target formations for increased location estimation accuracy [17], [34].

To leverage the advantage of both elevation and mobility, the proposed scheme is developed in the context of an elevated, mobile WSN; elevated to promote a LOS signal

path for increased received power and range, and mobile for control over sensor-target geometry for increased localization accuracy.

#### **4.      Multirotor UAV as an Elevated, Nobile WSN Sensor Node**

Sensor nodes for WSNs have been developed for different operating environments, such as stationary ground networks [35], ground mobile networks [36], and airborne networks [37]. For signal collection, the ideal operating environment is elevated above physical obstructions and noisy surface environments. Such a vantage point extends communications range and promotes a line-of-sight signal path. For this research, we propose the use of an elevated, mobile WSN. A possible realization of this network is via the use of multirotor unmanned aerial vehicles (UAVs) [38], [39]. These UAVs can provide a mobile sensor platform that in contrast to fixed-wing UAVs can maintain a given position. This research does not undertake sensor network implementation using multirotor UAVs; however, the simulations in this dissertation utilize the concept of an elevated and mobile sensor node realized by multirotor UAVs.

Although the modern multirotor UAV has only recently been developed, it remains a relatively simple machine. For instance, a quadrotor has four rotors held together with a rigid frame [40]. Control of such vehicles is basically accomplished through the differential manipulation of each rotor's thrust [38], [39]. In contrast to fixed-wing UAVs, multirotor UAVs are under-actuated, with the remaining degrees of freedom controlled through system dynamics. Having demonstrated their effectiveness in many applications, such as environment mapping and monitoring [41], [42], transportation and construction [43], and wireless communication/networking [44], they have become a popular research platform. For more information regarding multirotor UAVs, see [38], [39].

##### ***a.      Multirotor UAV Station Keeping***

There are many aspects to multirotor UAVs to consider when used as a sensor node. Of key concern is its ability to station keep a given position, for any deviation from its given position due to system errors and/or wind results in sensor position errors. The station keeping performance of a standard proportional-integral-derivative (PID)

controlled quadrotor in the presence of wind is found in Figure 3. Here, the wind is modeled using a Dryden model [45]. From the illustration, we can see the observed position errors due to station keeping operations do not easily conform to any standard distribution. The actual position errors of a multirotor UAV are mainly governed by wind, GPS accuracy, and flight controller scheme [46], [47], [48]. In the absence of such knowledge, we resort to two basic position error distributions, uniform and Gaussian.

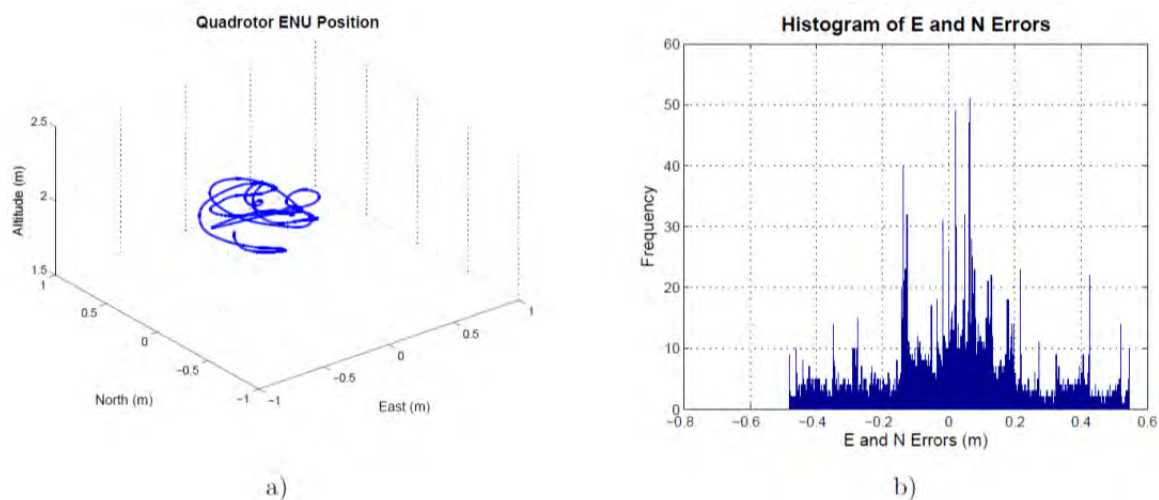


Figure 3. Simulated quadrotor station keeping in the presence of Dryden modeled wind, a) UAV three-dimensional (3D) motion, b) histogram of two-dimensional (2D) position errors, from [48].

## B. HYPERBOLIC SOURCE LOCALIZATION

Hyperbolic localization is the process of determining the location of a signal emitter based on difference of a signal's time-of-arrival (TOA) across an array of sensor nodes. Because of its dependence on the difference in TOA, it is also called localization via time-difference-of-arrival (TDOA) measurements. Hyperbolic localization has been studied extensively and can be found in many applications [49], [50], [51]. Hyperbolic location is commonly applied in WSN as a passive technique; passive in the sense that the receiving sensors require little information or synchronization with the transmitter. Two-dimensional (2D) hyperbolic localization begins when a signal is received by three

or more synchronized sensors [5]. The transmitter's location is then determined by a set of hyperbolic equations that are derived from the TDOA measurements.

To derive this system of hyperbolic equations, let us consider a signal's TOA at the  $i^{\text{th}}$  node of an  $M$  node WSN as

$$t_i = t_0 + d_i / c, \quad (4)$$

where  $t_0$ ,  $d_i$ , and  $c$  are the signal's time-of-emission, distance from the transmitter to the  $i^{\text{th}}$  node, and signal propagation speed, respectively. Typically, these TOA measurements are obtained using the cross-correlation method [16]. By taking the difference between a pair of nodes' measured TOA, we eliminate  $t_0$  and can obtain a set of TDOA equations as

$$t_{i+1} - t_1 = (d_{i+1} - d_1) / c, \quad (5)$$

with  $i = 2, 3, \dots, M$ . This can be rewritten to generate hyperbolic equations that include the transmitter's and the  $i^{\text{th}}$  sensor's location in Cartesian coordinates as [52]

$$c(t_{i+1} - t_1) = \sqrt{(x_{i+1} - x_t)^2 + (y_{i+1} - y_t)^2} - \sqrt{(x_1 - x_t)^2 + (y_1 - y_t)^2} \quad (6)$$

where  $(x_i, y_i)$  is the  $i^{\text{th}}$  node's location and  $(x_t, y_t)$  is the transmitter's location. With a minimum of three sensor nodes yielding two simultaneous equations in the form of (6), a two-dimensional location estimate can be determined [5].

Since the system of equations governing this reconstruction is non-linear, solving them becomes a non-trivial matter. There are two ways to deal with this issue. One is to avoid the non-linear equations altogether by selectively setting the coordinate system [34], [5], and the other linearizes the function through Taylor series expansion about a reference point [17], [52]. Additionally, the research in this dissertation is focused on elevated, mobile networks with an emphasis on a line-of-sight (LOS) signal path and does not address the non-LOS case. For non-LOS solutions, see [53] and [54].

## 1. Weighted Least-Squares Estimation

The least-squares method is the standard approach for parameter estimation, given a set of measurements that are derived from a linear function of inputs and parameters [55]. The least-squares solution is obtained as a set of  $N_\omega$  parameters that minimizes the sum of the squared errors:

$$E_{LS} = \sum_{i=1}^{N_m} \left( y_i - f(x_i, \boldsymbol{\omega}_{LS}) \right)^2, \quad (7)$$

where  $N_m$  is the number of noisy measurements,  $f(x_i, \boldsymbol{\omega}_{LS})$  is a linear function of the  $i^{\text{th}}$  input variable  $x_i$  and the  $N_\omega \times 1$  solution parameter vector  $\boldsymbol{\omega}_{LS}$ , and  $y_i$  is the  $i^{\text{th}}$  noisy measurement defined as

$$y_i = f(x_i, \boldsymbol{\omega}_{LS}) + \varepsilon_w, \quad (8)$$

with  $\varepsilon_w$  being the zero mean Gaussian measurement error. It is important to clarify the linear nature of  $f(x_i, \boldsymbol{\omega}_{LS})$ . This function is considered a linear model, when the relationship between the input variable and the output is a linear parameterization of  $\boldsymbol{\omega}_{LS}$ . When the measurements are taken at different levels of uncertainty, the weighted least-squares approach has been shown to be optimal [56], [57]. The weighted least-squares solution minimizes the sum of weighted squared-errors:

$$E_{WLS} = \sum_{i=1}^{N_m} w_{LS,i} \left( y_i - f(x_i, \boldsymbol{\omega}_{WLS}) \right)^2, \quad (9)$$

where  $w_{LS,i}$  is the  $i^{\text{th}}$  weight and  $\boldsymbol{\omega}_{WLS}$  is the  $N_\omega \times 1$  parameter vector. The weighted least-squares estimate in matrix form is expressed as [56]

$$\hat{\omega}_{WLS} = \left( \mathbf{X}^T \mathbf{W} \mathbf{X} \right)^{-1} \mathbf{X}^T \mathbf{W} \mathbf{y}, \quad (10)$$

where  $\mathbf{y}$  is  $N_m \times 1$  vector of noisy measurements, the  $N_m \times N_m$  weighting matrix is

$$\mathbf{W} = \begin{bmatrix} \frac{1}{\sigma_{y,1}^2} & \cdots & 0 \\ \vdots & \ddots & \vdots \\ 0 & \cdots & \frac{1}{\sigma_{y,N_m}^2} \end{bmatrix}, \quad (11)$$

where  $\sigma_y^2$  is the measurement variance and the  $N_\omega \times N_m$  input variable matrix is [56]

$$\mathbf{X} = \frac{\partial f(x_i, \omega_{LS})}{\partial \omega_{LS}} = \begin{bmatrix} \frac{\partial f(x_1, \omega_{LS})}{\partial \omega_1} & \cdots & \frac{\partial f(x_1, \omega_{LS})}{\partial \omega_{N_\omega}} \\ \vdots & \vdots & \vdots \\ \frac{\partial f(x_{N_m}, \omega_{LS})}{\partial \omega_1} & \cdots & \frac{\partial f(x_{N_m}, \omega_{LS})}{\partial \omega_{N_\omega}} \end{bmatrix}. \quad (12)$$

## 2. Maximum-Likelihood Estimation

The maximum-likelihood estimator also requires the system of equations to be linear. The term “maximum-likelihood” is used because the solution maximizes the likelihood, i.e., the statistical model of the estimate matches that of the measurements. Since the maximum-likelihood estimator is both asymptotically unbiased and efficient, i.e., achieves the Cramer-Rao lower bound (CRLB) [15], [58], it has become widely adopted in the field of parameter estimation.

To derive the maximum-likelihood solution, we consider an  $M \times 1$  noisy measurement vector given by

$$\mathbf{y} = \mathbf{z}(\boldsymbol{\omega}, \mathbf{x}) + \boldsymbol{\varepsilon}, \quad (13)$$

where  $\boldsymbol{\omega}$  is the  $N_{\omega} \times 1$  vector of unknown but nonrandom set of parameters to be estimated,  $\mathbf{z}(\boldsymbol{\omega}, \mathbf{x})$  is a function of  $\boldsymbol{\omega}$  and the input vector  $\mathbf{x}$ , and  $\boldsymbol{\varepsilon}$  is the zero mean Gaussian measurement error. The likelihood of  $\mathbf{y}$  for a given  $\boldsymbol{\omega}$  is governed by its conditional probability density function and is expressed as [52]

$$f_{\mathbf{y}|\boldsymbol{\omega}}(\mathbf{y}|\boldsymbol{\omega}) = \frac{1}{(2\pi)^{M/2} \sqrt{|\mathbf{C}_{\varepsilon}|}} \exp\left(-\frac{1}{2} [\mathbf{y} - \mathbf{z}(\boldsymbol{\omega}, \mathbf{x})]^T \mathbf{C}_{\varepsilon}^{-1} [\mathbf{y} - \mathbf{z}(\boldsymbol{\omega}, \mathbf{x})]\right), \quad (14)$$

where  $|\cdot|$  denotes the determinant of a matrix, and  $\mathbf{C}_{\varepsilon}$  is the covariance matrix of the measurement error  $\boldsymbol{\varepsilon}$  and is defined as

$$\mathbf{C}_{\varepsilon} = E\left\{\left(\boldsymbol{\varepsilon}_{ML} - E\{\boldsymbol{\varepsilon}_{ML}\}\right)\left(\boldsymbol{\varepsilon}_{ML} - E\{\boldsymbol{\varepsilon}_{ML}\}\right)^T\right\}. \quad (15)$$

Finally, the maximum-likelihood estimator of  $\boldsymbol{\omega}$  can be obtained by minimizing the exponent quadratic of (14) [52]

$$\mathbf{Q}_{ML} = [\mathbf{y} - \mathbf{z}(\boldsymbol{\omega}, \mathbf{x})]^T \mathbf{C}_{\varepsilon}^{-1} [\mathbf{y} - \mathbf{z}(\boldsymbol{\omega}, \mathbf{x})].$$

We now encounter the same problem as with the weighted least-squares estimator, where  $\mathbf{z}(\boldsymbol{\omega}, \mathbf{x})$  is nonlinear, i.e., the relationship between  $\mathbf{y}$  and  $\mathbf{x}$  is not a linear parameterization of  $\boldsymbol{\omega}$ . The standard solution is then to linearize the functions through a Taylor series expansion about a reference point  $\boldsymbol{\omega}_r$ . Using only the first two terms of the expansion, we have the following approximation [52]

$$\mathbf{z}_T(\boldsymbol{\omega}, \mathbf{x}) \approx \mathbf{z}(\boldsymbol{\omega}_r, \mathbf{x}) + \mathbf{G}_{\text{ts}}(\boldsymbol{\omega} - \boldsymbol{\omega}_r), \quad (16)$$

where  $\mathbf{G}_{ts}$  is the  $M \times N_{ML}$  gradient matrix given by

$$\mathbf{G}_{ts} = \begin{bmatrix} \left. \frac{\partial z_1}{\partial \omega_1} \right|_{\omega=\omega_r} & \dots & \left. \frac{\partial z_1}{\partial \omega_{N_{ML}}} \right|_{\omega=\omega_r} \\ \vdots & & \vdots \\ \left. \frac{\partial z_M}{\partial \omega_1} \right|_{\omega=\omega_r} & \dots & \left. \frac{\partial z_M}{\partial \omega_{N_{ML}}} \right|_{\omega=\omega_r} \end{bmatrix}. \quad (17)$$

The maximum-likelihood estimator can then be obtained as [52]

$$\hat{\omega}_{ML} = \omega_r + \left( \mathbf{G}_{ts}^T \mathbf{C}_\varepsilon^{-1} \mathbf{G}_{ts} \right)^{-1} \mathbf{G}_{ts}^T \mathbf{C}_\varepsilon^{-1} (\mathbf{y} - \mathbf{z}(\omega_r, \mathbf{x})). \quad (18)$$

It is important to note that the maximum-likelihood estimator can be iteratively processed if there are multiple sets of  $\mathbf{y}_{TD}$ . These iterations can be used to overcome the effects of an inaccurate  $\omega_r$  or compensate for increased measurement noise. The iterative performance of a 15 node maximum-likelihood estimator initialized with an inaccurate  $\omega_r$  is shown in Figure 4. With  $\omega_r$  set 1100 meters away from the true location, we can see that the estimator quickly approaches the asymptotic optimal minimum error value [59].

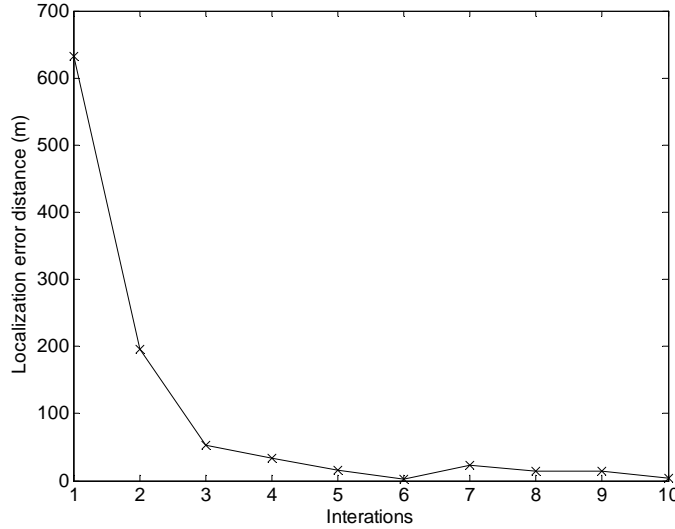


Figure 4. Iterative performance of a hyperbolic maximum-likelihood estimator in the presence of an inaccurate  $\omega_r$  estimate.

### 3. Optimal Formations for Source Localization

To derive the optimal formations for hyperbolic localization, we first determine its Cramer-Rao lower bound (CRLB) [17]. For localization using polar coordinates, the CRLB is derived using the Fisher information matrix of the hyperbolic localization. The Fisher information matrix is given by [17]

$$\Phi(\omega) = \begin{bmatrix} X_F & Y_F \\ Y_F & Z_F \end{bmatrix} = \begin{bmatrix} \frac{\partial \mathbf{d}^0}{\partial r} & \frac{\partial \mathbf{d}^0}{\partial \theta} \end{bmatrix}^T \mathbf{C}_\varepsilon^{-1} \begin{bmatrix} \frac{\partial \mathbf{d}^0}{\partial r} & \frac{\partial \mathbf{d}^0}{\partial \theta} \end{bmatrix}, \quad (19)$$

where  $r$  is range,  $\theta$  is bearing,  $\mathbf{d}^0$  is the  $(M-1) \times 1$  true TDOA vector, and the  $(M-1) \times (M-1)$  covariance matrix of the TDOA measurement error  $\mathbf{C}_\varepsilon$  is expressed as [17]

$$\mathbf{C}_\varepsilon = \frac{\sigma_R^2}{2} (\mathbf{I} + \mathbf{1}_{M-1} \mathbf{1}_{M-1}^T), \quad (20)$$

where  $\sigma_R^2$  is the range measurement error variance,  $\mathbf{I}$  is the  $(M-1) \times (M-1)$  identity matrix, and  $\mathbf{1}_{M-1}$  is a column vector of  $(M-1)$  ones. The elements of the Fisher information matrix from (19) are [17]

$$X_F = \frac{1}{2M\sigma_R^2 c^2 r_t^4} \left\{ M \sum_{i=1}^M r_i^4 \sin^4(\theta_t - \theta_i) - \left[ \sum_{i=1}^M r_i^2 \sin^2(\theta_t - \theta_i) \right]^2 \right\}, \quad (21)$$

$$Y_F = \frac{-1}{M\sigma_R^2 c^2 r_t^2} \left\{ M \sum_{i=1}^M r_i^3 \sin^3(\theta_t - \theta_i) - \left[ \sum_{i=1}^M r_i^2 \sin^2(\theta_t - \theta_i) \right] \left[ \sum_{i=1}^M r_i \sin(\theta_t - \theta_i) \right] \right\}, \quad (22)$$

and

$$Z_F = \frac{2}{M \sigma_R^2 c^2} \left\{ M \sum_{i=1}^M r_i^2 \sin^2(\theta_i - \theta_i) - \left[ \sum_{i=1}^M r_i \sin(\theta_i - \theta_i) \right]^2 \right\}, \quad (23)$$

where  $c$  is the signal propagation speed and  $(r_i, \theta_i)$  is the  $i^{\text{th}}$  sensor's polar location. Based on the use of the maximum-likelihood estimator, which is asymptotically efficient, the objective is to choose a sensor formation that will decouple the range and bearing estimates, i.e., a formation that makes the element  $Y_F = 0$ . In [17], it is shown that a system of concentric circles satisfies this condition. From within this concentric circle formation, we can select a sub-formation that either maximizes  $X_F$  or  $Z_F$ , i.e., minimizes the CRLB of range or bearing

$$r_{\text{CRLB}} = \frac{1}{X_F} = \left[ \frac{M r_a^4}{8 \sigma_R^2 c^2 r_t^4} \sin^4 \theta_t \right]^{-1} \quad \text{and} \quad (24)$$

$$\theta_{\text{CRLB}} = \frac{1}{Z_F} = \left[ \frac{2 M r_a^2}{\sigma_R^2 c^2} \sin^2 \theta_t \right]^{-1}$$

In [52], Torrieri showed that the formation of the sensors in relation to the signal emitter affects the localization accuracy. This degradation in accuracy is termed the geometric dilution of precision (GDOP). For the maximum-likelihood estimator, it is given by [52]

$$\Gamma_{ML} = \sqrt{\text{tr} \left( \left( \mathbf{G}_{ts}^T \mathbf{C}_{\mathcal{E}}^{-1} \mathbf{G}_{ts} \right)^{-1} \right)} / (c \sigma_s), \quad (25)$$

where

$$\sigma_s^2 = \frac{1}{N_M} \sum_{i=1}^{N_M} \sigma_{t,i}^2 \quad (26)$$

is the average variance of the arrival times with  $\sigma_{t,i}^2$  being the variance of the TOA measurements at the  $i^{\text{th}}$  node. To combat this degradation, we employ optimal sensor formations that minimize the effects of GDOP [17]. Through inspection of the CRLB, it can be shown that the sensor formations from Figure 5 minimize GDOP [34], [17].

Each of the three formations in Figure 5 is suited to different applications depending on the estimated parameter of interest. Here,  $J$  is the number of sensor groups and  $M$  is the total number of sensors. The circular formation ( $J = 3$  or  $J \geq 5$ ) provides optimal bearing and range estimates, independent of the targets bearing. The line formation ( $J = 2$ ) delivers the best range and bearing estimates but is dependent on the target's bearing [17], [34]. The cross formation ( $J = 4$ ) delivers performance comparable to the circular formation with minor dependence on the target's bearing. Although some of the formations in Figure 5 may not look like concentric circles, like the linear or cross formations, they are indeed two concentric circles. One large circle surrounding a smaller one whose radius is zero.

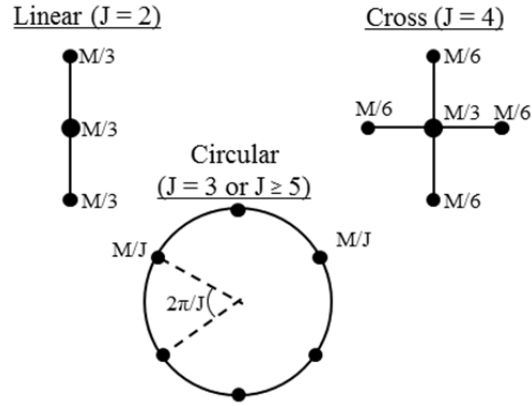


Figure 5. Optimum array geometries for position estimation (minimum uncertainty area) using TDOA localization.  $J$  = number of sensor groups,  $M$  = total number of sensor, from [17].

For more information regarding these optimal formations see [17] and [34].

#### 4. The Airborne Symmetrical Line Array Network Configuration

In this section, we describe the term airborne symmetric line array (ASLA) formation. The ASLA formation consists of multiple elevated, mobile sensors in a line formation symmetric about the origin. This formation is based on the linear formation in Figure 5 and is illustrated in Figure 6. It consists of three sensor stacks that contain  $N_s = M / 3$  sensors each. The center stack is located at the origin, with two outer stacks flanking the center at a distance of  $r_a$ . For hyperbolic localization, this formation has been show to minimize the maximum-likelihood error variance [17]. Note that each sensor in a stack must be separated by  $\lambda / 2$  to guarantee independent noise and to minimize mutual coupling [34].

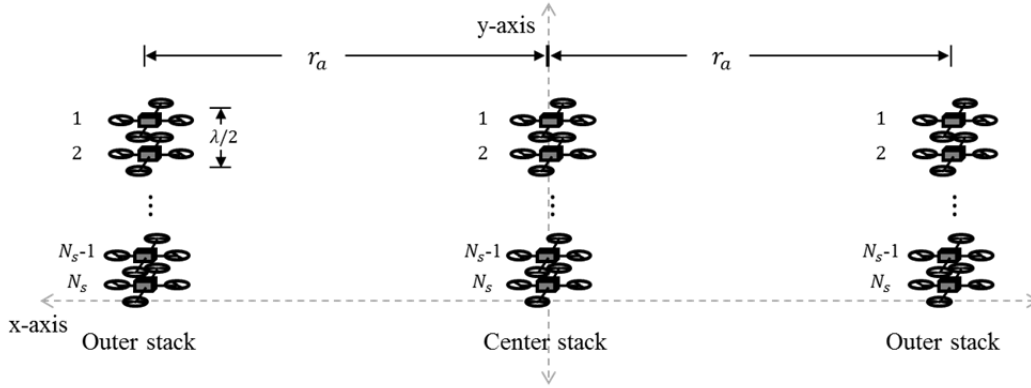


Figure 6. Illustration of the ASLA formation.

The linear formation is special in the sense that it delivers the best performance in bearing and range estimates. The caveat is that this optimality is dependent on the target emitter's bearing [34]. A Monte Carlo simulation illustrating the dependence on the target bearing is shown in Figure 7. Here, the hyperbolic localization accuracy of an eight node ASLA formation is compared with an equal numbered circular formation at varying target bearing. From the simulation, we see that the bearing of the target has little to no effect on the circular estimate, whereas the linear formation performs better when the target bearing is approximately  $\pm 30$  degrees from the array's normal direction.

Even though conditionally optimal, its high accuracy is the key reason the linear formation was chosen for the proposed scheme.

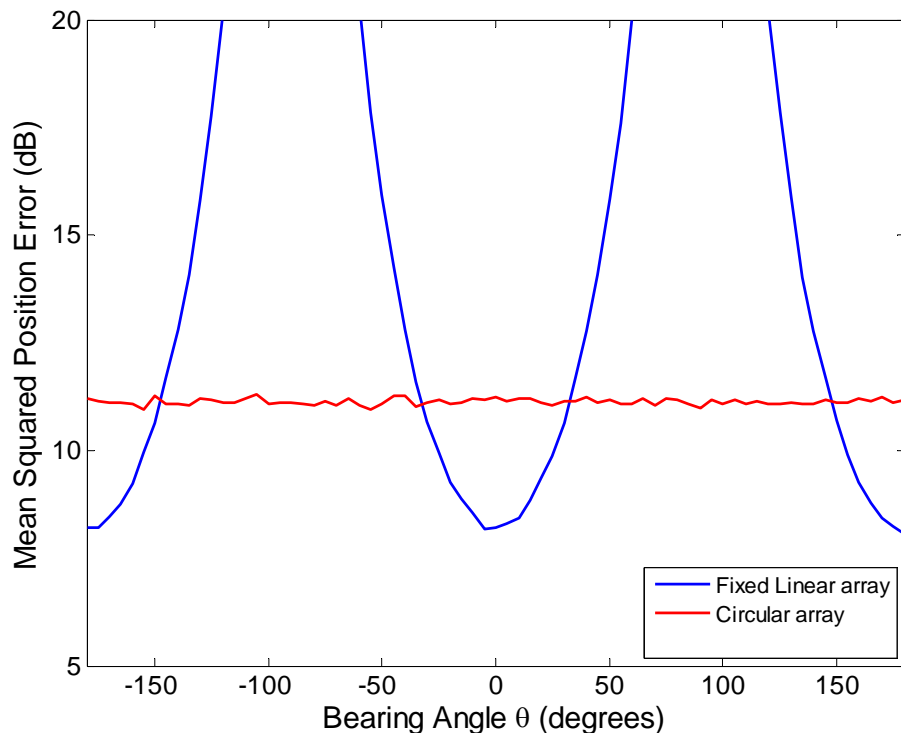


Figure 7. Accuracy of position estimate for fixed linear formation (blue) and fixed circular formation (red).

## 5. TDOA Outlier Measurement Diagnostics

With the proposed localization technique implemented on an elevated, mobile sensor network, there will be increased measurement noise due to sensor position and other sensor network related errors. This increase in measurement noise creates a need for methods to mitigate the effects of statistical outliers or errors on parameter estimation. In this section, we cover some statistical tools used in our proposed localization scheme for robustness to such errors.

To assess the influence of the  $i^{\text{th}}$  measurement/observation in a least-squares solution, we can calculate the solution with and without it. Calculating the amount of divergence with and without the measurement is termed “single case diagnostics” [18].

To perform this diagnostic, it is important to consider which measure of divergence is appropriate for the solution. A standard approach is to use the squared-Mahalanobis distance given by [18], [19],

$$D_{M,i} = (\mathbf{v}_i - E\{\mathbf{v}_\omega\}) \mathbf{C}_\omega^{-1} (\mathbf{v}_i - E\{\mathbf{v}_\omega\})^T, \quad (27)$$

where the  $\mathbf{v}_\omega$  is the  $M \times 2$  matrix containing  $M$  location estimates,  $\mathbf{v}_i$  is the  $1 \times 2$  vector containing the  $i^{\text{th}}$  location estimate, and  $\mathbf{C}_\omega$  is the covariance matrix of  $\mathbf{v}_\omega$ . The purpose of the Mahalanobis distance is to discern how much influence the  $i^{\text{th}}$  measurement has on the solution given the covariance of each of the measurements.

To illustrate this concept, we consider a set of 200 weighted least-squares location estimates shown in Figure 8. In this set, there is one outlier shown in green, which we wish to reject. Using the Euclidean distance from the mean as a measure of divergence, we see that the outlier has the same divergence as the standard estimate shown in red. In contrast, using the Mahalanobis distance as the measure of divergence, we find that the outlier has a divergence of 34.5 where as the standard estimate has a divergence of 0.9; hence, the outlier can be easily identified and discarded.

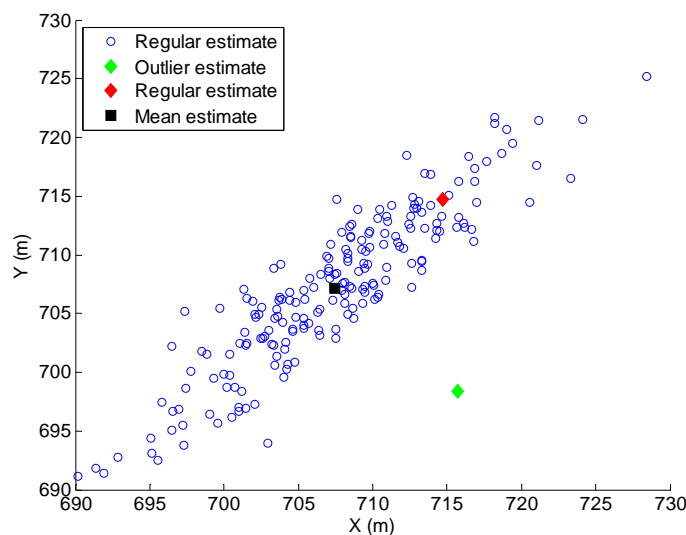


Figure 8. Scatter plot of 200 hyperbolic location estimates.

### C. BEAMFORMING

Beamforming is an efficient signal processing technique that enables space-division multiple access [6]. The benefits and various applications of traditional beamforming have been well documented [60], [61]. The extension of beamforming to wireless sensor networks has given rise to the concept of collaborative beamforming [2], [62] in which a network of synchronized and distributed sensors is used to form a distributed beamforming array.

Beamforming begins with a plane wave signal impinging on the array from a direction-of-arrival  $\theta_i$ . With the signal arriving at each node with a corresponding phase delay, beamforming uses phase shifters to nullify this delay and constructively sums each node's signal. The concept of a plane wave falling across a uniform linear array of  $M$  nodes where the phase delay is a function of the distance between each node  $d$  is illustrated in Figure 9.

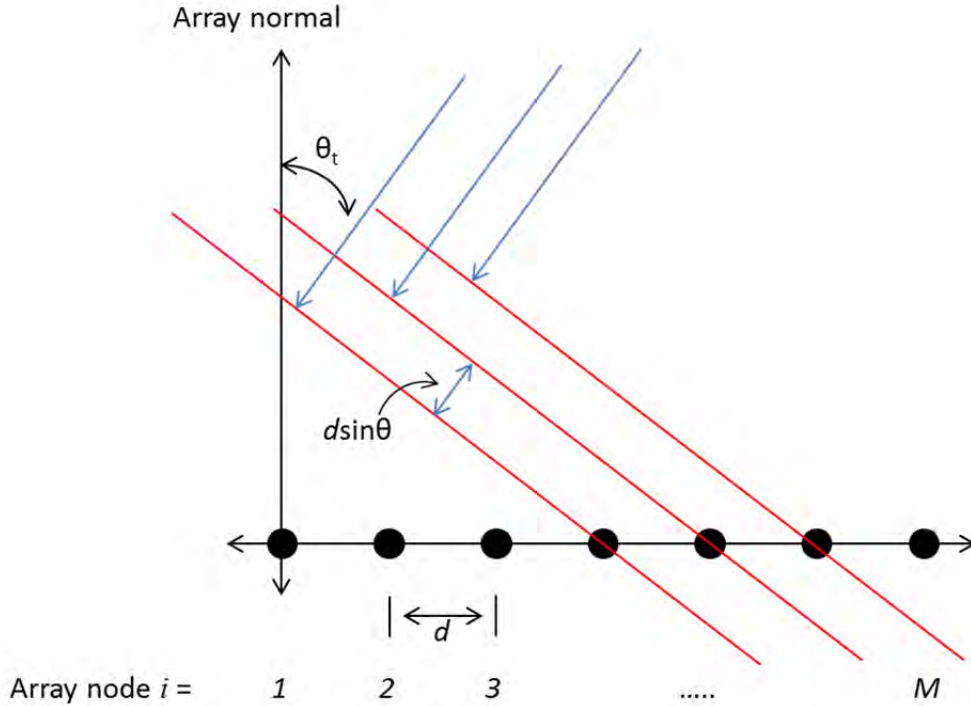


Figure 9. Plane wave impinging on a uniform linear array.

## 1. Phase Shift Beamforming

With the phase of the incoming signal at node  $i=1$  set to zero, the combined signal of a uniform linear array with  $M$  nodes, commonly termed the array factor can be expressed as [63]

$$A_{FL}(\theta_t, \theta_{sa}) = \sum_{i=1}^M w_i e^{j(i-1)\beta d \sin \theta_t}, \quad (28)$$

where

$$w_i = A_i e^{-j\beta d \sin \theta_{sa}} \quad (29)$$

is the complex weight with magnitude  $A_i$  and phase  $-\beta d \sin \theta_t$ ,  $\lambda$  is the signal wavelength and  $\beta = (2\pi)/\lambda$ . From (28), it is apparent that the array yields a maximum response in the direction of the beam steering angle  $\theta_{sa}$ . By controlling the response of the array as a function of  $\theta_{sa}$ , the spatial diversity required for space-division multiple access is achieved. Along with this diversity, beamforming also provides a signal gain equal to the number of receiving elements/nodes.

There are many parameters that dictate the resulting array factor of a beamforming array. Of key importance to this research is the number elements/nodes and their placement relative to each other. The effect of increasing the number of elements/nodes in a uniform linear array's array factor is illustrated in Figure 10. The first effect is the narrowing of the main beam's beamwidth. The main beam is defined as the lobe that contains the direction of the array factor's maximum response. The beamwidth, also called the half-power beam width, is typically defined as the angle range at which the main beam falls above 3 dB of the maximum response. The relationship between the beamwidth and the number of nodes in a linear array is given by [63]

$$B_w \approx \frac{0.88\lambda}{d M}. \quad (30)$$

The second effect is the location and the number of sidelobes present in the array factor. Sidelobes are defined as any lobe other than the main beam lobe. For uniform linear arrays, the magnitude of the nearest sidelobe to the main lobe is on average 13 dB lower [63].

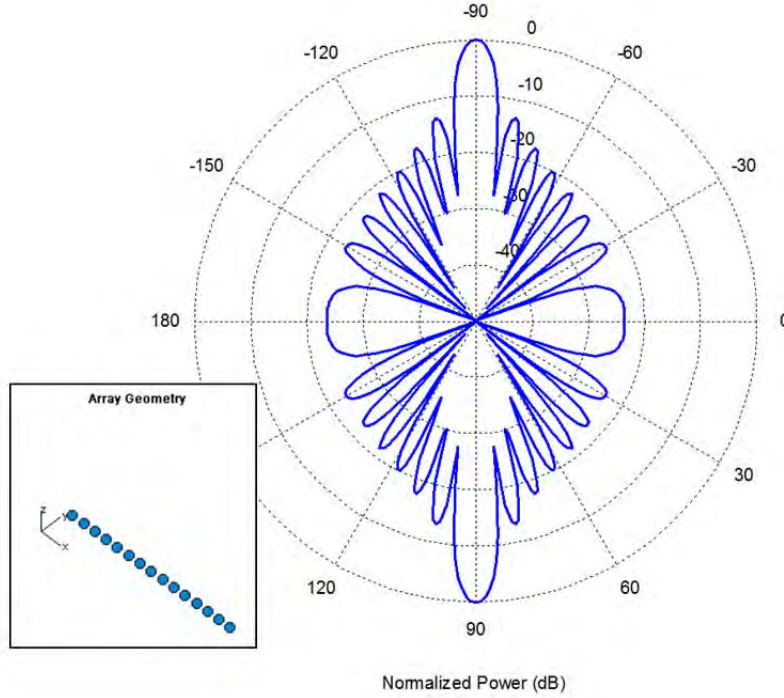


Figure 10. Array factor of a 15 isotropic node linear array with  $d = \lambda / 2$ .

## 2. Adaptive Beamforming

Adaptive beamforming is the process of adapting an antenna's array factor in a manner that both increase the gain of a target signal while decreasing the gain of all interfering signals. This is accomplished by placing a complex weight on each antenna signal. These weights modify the phase and allow for the coherent amplification (reduction) of a target signal (undesired signals). In this section, we will illustrate the

basic phase shift beamformer [64], [65] and the adaptive minimum variance distortionless response (MVDR) beamformer [66], [67].

The MVDR beamformer combats the effects of interfering signals by placing nulls in their direction. This is achieved by selecting the array weights that minimize the output noise variance [63]. The array output is expressed as

$$y(t) = \mathbf{w}^H \mathbf{s} + \mathbf{w}^H \mathbf{u}, \quad (31)$$

where  $\mathbf{w}$  is an  $M \times 1$  vector of the complex weights to be determined,  $\mathbf{u}$  is an  $M \times 1$  vector of the sum of all interfering signal vectors  $\boldsymbol{\eta}_i = [1, e^{i\beta d \sin \theta_i}, \dots, e^{i\beta(M-1)d \sin \theta_i}]^T$  represented as

$$\mathbf{u} = \sum_{i=1}^{N_u} u_i(t) \boldsymbol{\eta}_i, \quad (32)$$

and  $\mathbf{s}$  is an  $M \times 1$  the signal vector represented by

$$\mathbf{s} = s(t) \mathbf{v}, \quad (33)$$

with  $s(t)$  being the desired signal and the steering vector  $\mathbf{v} = [1, e^{i\beta d \sin \theta}, \dots, e^{i\beta(M-1)d \sin \theta}]^T$ . By minimizing the noise contributions of the interfering signals in the output, we can determine the optimal weights  $\mathbf{w}_o$ . The output variance can be shown as [63]

$$\sigma_y^2 = \mathbf{w}^H \mathbf{R}_s \mathbf{w} + \mathbf{w}^H \mathbf{R}_u \mathbf{w}. \quad (34)$$

Assuming that  $\mathbf{R}_s = E\{\mathbf{s}\mathbf{s}^H\}$  and  $\mathbf{R}_u = E\{\mathbf{u}\mathbf{u}^H\}$  are known, we see that the minimization of the output variance is reduced to the minimization of  $\mathbf{w}^H \mathbf{R}_u \mathbf{w}$ , which results in an expression for the optimal weights [63]

$$\mathbf{w}_o = \frac{1}{\mathbf{v}^H \mathbf{R}_u^{-1} \mathbf{v}} \mathbf{R}_u^{-1} \mathbf{v} . \quad (35)$$

To illustrate both the phase shift and MVDR beamforming concepts, we consider a scenario where a target signal with two interfering signals is received by the 15 node uniform linear array shown in Figure 10. The target signal-of-interest is shown in Figure 11, with a direction-of-arrival (DOA) of 45 deg and a signal amplitude of one. The two interfering signals are arriving at a DOA of 30 and 50 deg, each with an amplitude of 10.

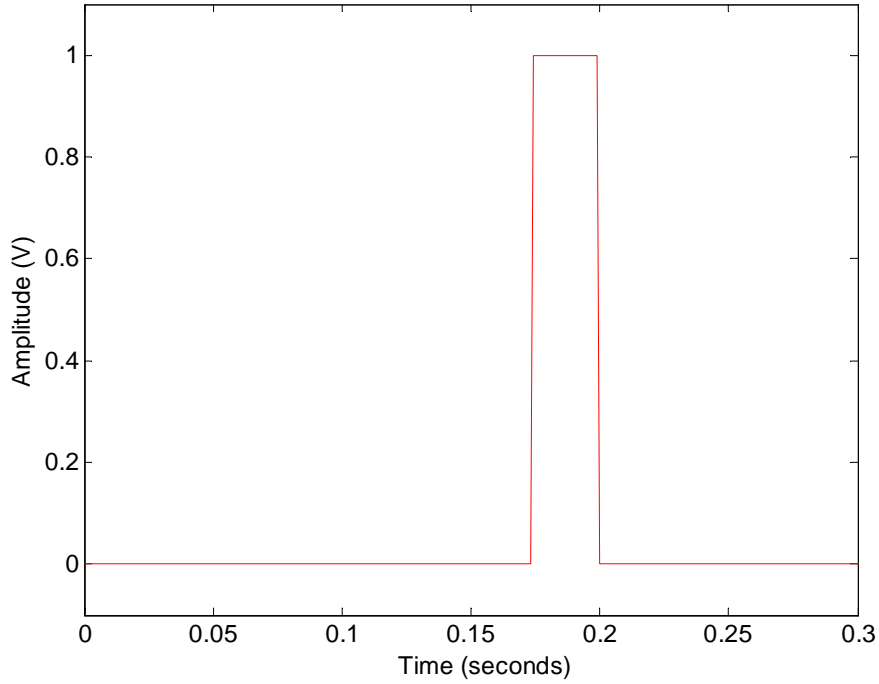


Figure 11. Transmitted signal-of-interest.

The phase shift beamformer's response to the interfering signals and target signal is shown in Figure 12. We can see the two interfering signals have fully corrupted the target signal. In contrast to the phase shift beamformer, the adaptive MVDR beamformer response is shown in Figure 13. From this, we can clearly see that the MVDR beamformer is able to nullify interference and successfully recover the target signal.

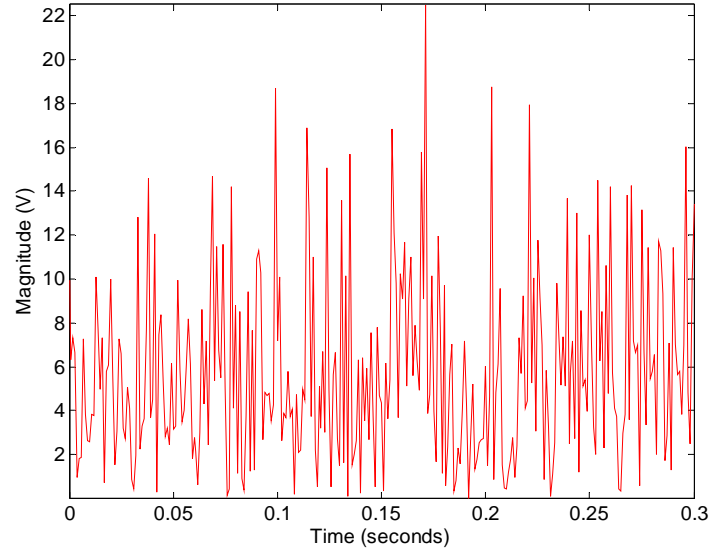


Figure 12. Response of 15 node phase shift beamformer with two 10 dB interfering signals at DOA of 30 and 50 degrees.

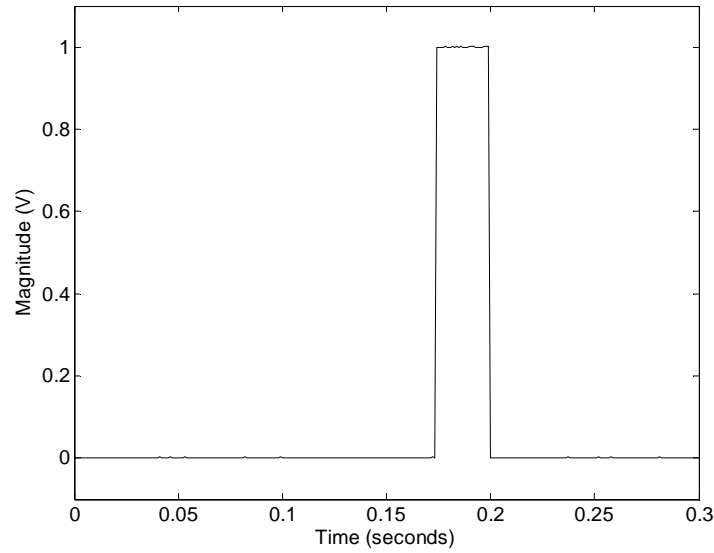


Figure 13. Output signal of the MVDR beamformer in the presence of a target signal at  $\theta_t = 45^\circ$  and two interfering signals at  $\theta_i = 30$  and  $50^\circ$ .

A comparison between the array factor of the MVDR and that of the phase shift beamformer is provided in Figure 14. From the illustration, we can see the MVDR's array factor contains two strong nulls in the directions of the interference, whereas the

phase shift beamformer has a response of approximately  $-13$  dB and  $-3$  dB in the same directions.

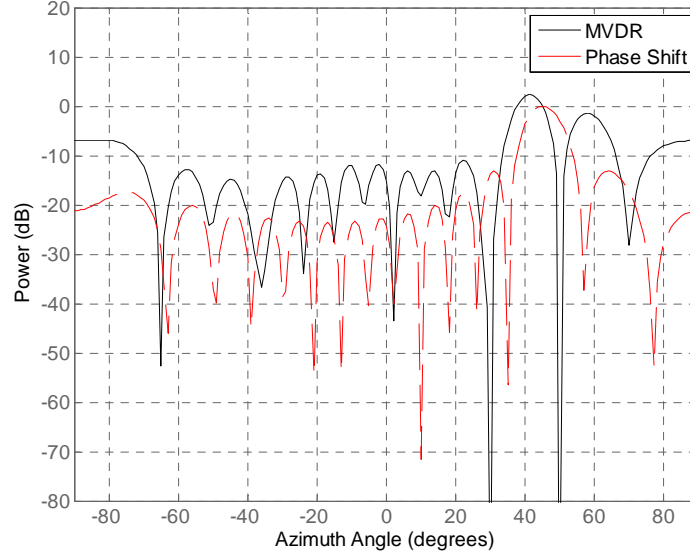


Figure 14. Comparison between the MVDR and phase shift beamformers in the presence of a target signal at  $\theta_t = 45$  deg and two interfering signals at  $\theta_i = 30$  and  $50$  deg .

### 3. Error Effects in Beamforming

Two key errors to account for in beamforming are pointing errors and unintended sidelobe response. Pointing errors are defined as the difference between the array's actual steering direction and that of the maximum response. The standard deviation of the pointing error is given by [4]

$$\sigma_{PE} \approx \frac{\sigma_{\phi}(B_w)}{\sqrt{M}}, \quad (36)$$

where  $\sigma_{\phi}$  is the standard deviation of the phase errors. With the beamwidth for a uniform linear array as defined in (30), the pointing errors can be expressed as

$$\sigma_{PE,ULA} \approx \frac{0.88\lambda\sigma_\phi}{d M \sqrt{M}}. \quad (37)$$

The expression for the expected side lobe level is given by [63]

$$\Delta_{sl} = \frac{a(1 - A^2) + \sigma_{\Delta a}^2}{Ma^2 A^2}, \quad (38)$$

where  $a$  is the error free main beam gain,  $\sigma_{\Delta a}^2$  is the variance of amplitude error and  $A^2 = \left| E \left\{ e^{i\Delta\phi} \right\} \right|^2$ . If the phase errors are zero mean and Gaussian, then  $A^2 = e^{-\sigma_{\Delta\phi}^2}$ .

#### 4. Sidelobe Control via Array Tapering

For a uniform linear array, the sidelobe response can be controlled by adjusting the gain of each node's response [68]. This process is termed tapering and is akin to windowing in digital filtering [69], [70]. Tapering an array provides a tradeoff between the beamwidth and the sidelobe levels. With this in mind, we will briefly examine the characteristics of four tapering methods: Uniform [71], Dolph-Chebyshev [72], Taylor-Kaiser [73], and Binomial [74].

##### a. Tapering Methods for Uniform Linear Arrays

The uniform tapered array is actually a non-tapered array as all nodes are uniformly weighted by one, which results in the standard phase shift beamformer with an array factor of

$$A_{FL}(\theta) = \sum_{m=1}^M e^{j(m-1)\beta d \sin\theta}. \quad (39)$$

This tapering method makes no consideration to sidelobe response and has the highest sidelobe level when compared to other methods.

The binomial tapered array is unique because it has zero sidelobes, but this is at the cost of a wider beamwidth. The weights of an  $M$ -node binomial uniform linear array are calculated from the binomial coefficients as follows [70]

$$w_{BN}(m) = \frac{(M-1)!}{m!(M-1-m)!}, \quad m = 0, 1, \dots, M-1. \quad (40)$$

The corresponding array factor is given by [70]

$$A_{FB}(\theta) = \left( 2 \cos \left( \frac{\theta}{2} \right) \right)^{M-1}. \quad (41)$$

From this expression, we can see that the array factor decreases to zero as  $\theta$  approaches  $\pm \pi$ .

The Dolph-Chebyshev [72] taper method is best applied when the sidelobe response at all angles must be kept below a specific value  $R_{DC}$ . The taper weights for the Dolph-Chebyshev uniform linear array are calculated using the Dolph-Chebyshev window transform [70], [75]

$$W_{Cheb}(\omega_k) = \frac{\cos \left( M \cos^{-1} \left[ R_0 \cos \left( \frac{\pi i}{M} \right) \right] \right)}{\cosh \left( M \cosh^{-1} (R_0) \right)}, \quad i = 0, 1, \dots, M-1, \quad (42)$$

where the scaling factor  $R_0$  is defined as [75]

$$R_0 = \cosh \left( \frac{\cosh^{-1} (10^{R_{DC}/20})}{M} \right). \quad (43)$$

The array weights  $w_{DC}(m)$  are then computed as the inverse discrete Fourier transform of  $W_{Cheb}(\omega_k)$ . The corresponding array factor for an array with an even number of nodes is expressed as [70]

$$A_{FD}(\theta) = \cos \left( 2M \cos^{-1} \left( R_0 \cos \left( \frac{\theta}{2} \right) \right) \right). \quad (44)$$

The Taylor-Kaiser tapering method is similar to the Dolph-Chebyshev method but has an exponentially decreasing sidelobe response. The array weights can be computed as [75]

$$w_{TK}(m) = I_0 \left( \pi \alpha_{TK} \sqrt{1 - m^2 / M^2} \right), \quad m = 1, \dots, M \quad (45)$$

where  $I_0$  is the zero<sup>th</sup>-order modified Bessel function of the first kind and  $\alpha_{TK}$  is the parameter used to control the sidelobe level response. The Taylor-Kaiser array factor can be expressed as [70]

$$A_{FT}(\theta) = \frac{M}{I_0(\pi \alpha_{TK})} \frac{\sinh \left( \sqrt{\alpha_{TK}^2 \pi^2 - (M\theta/2)^2} \right)}{\sqrt{\alpha_{TK}^2 \pi^2 - (M\theta/2)^2}}. \quad (46)$$

### ***b. Comparison of the Taper Methods***

A comparison of the four taper methods is illustrated in Figure 15. From the results, we see that the beamwidth is inversely proportional to the sidelobe response. We can see that the uniform tapering achieves the narrowest beamwidth with the highest sidelobe response, whereas the binomial tapering has the widest beamwidth with zero sidelobe response. The Dolph-Chebyshev has the unique ability to maintain a given maximum sidelobe response, while the Taylor-Kaiser taper show a better sidelobe response at the cost of a slightly wider beamwidth.

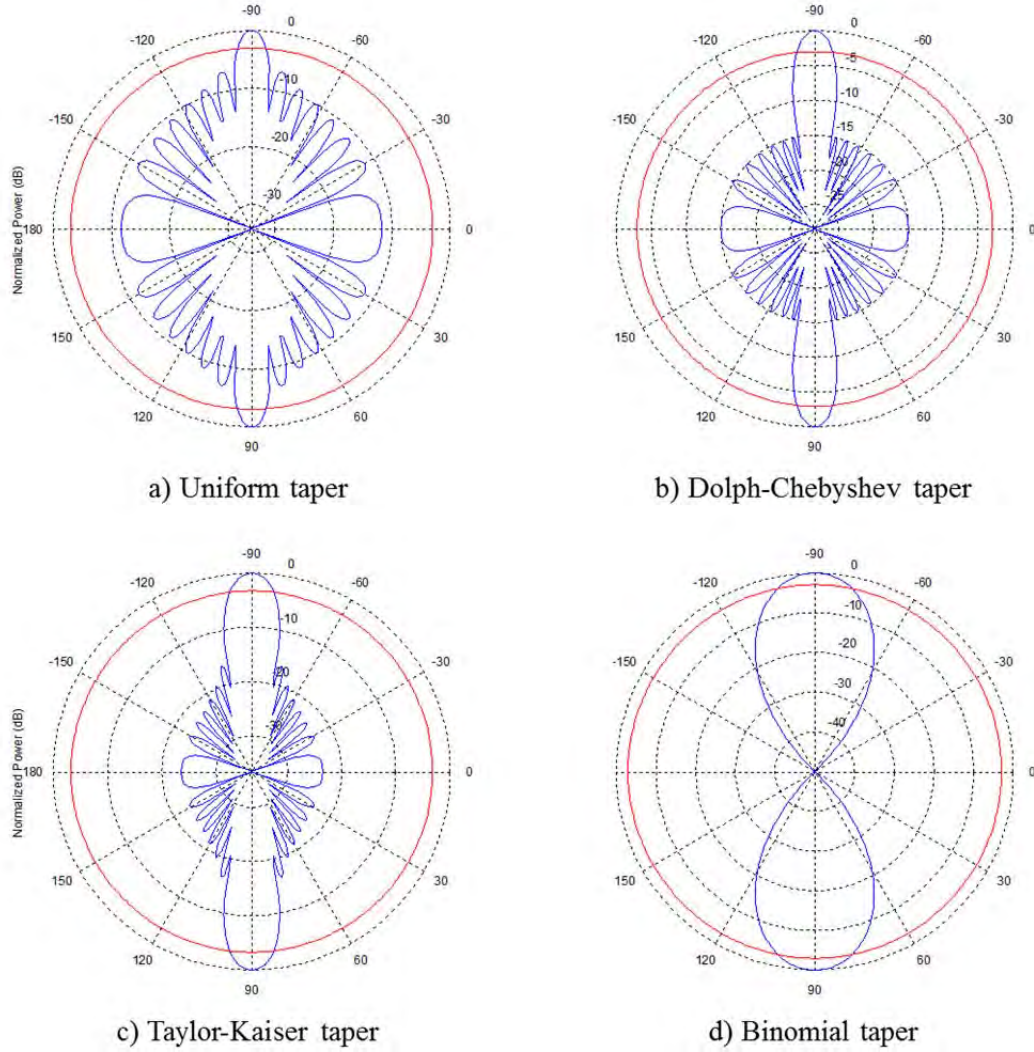


Figure 15. Beam width and sidelobe level tradeoff for four different tapering methods using a 15 node ULA. The beamwidth  $-3$  dB line is shown in red, from [70].

## 5. Grating Lobe Control via Virtual Filling

In collaborative beamforming where the nodes are separated by a distance greater than  $\lambda/2$ , grating lobes in the array factor will be a significant issue [71]. Grating lobes are lobes that have the same magnitude as the main lobe. To minimize the effects of grating lobes, the array can be virtually filled [76]. The virtual filling technique minimizes the grating lobes by filling in any internode distance  $d_v$  greater than  $\lambda/2$

with virtual nodes. These virtual nodes consist of interpolated complex signal data derived from the real nodes. This filling is done in a manner that turns the array into a virtually filled uniform linear array, which is inherently free of grating lobes [76].

A single snapshot of the complex signal received at the  $n^{\text{th}}$  node in a collaborative beamforming network can be expressed as

$$\mathbf{A}_n = \sum_{i=1}^{N_R} V_{t,i} \exp(j\phi_{t,i}) \exp(-j\beta x_n \sin \theta_{t,i}), \quad n = 1, \dots, M, \quad (47)$$

where  $N_R$  is the number of signals impinging on the array,  $x_n$  is the  $n^{\text{th}}$  node's location on the x-axis,  $V_{t,i}$ ,  $\phi_{t,i}$ , and  $\theta_{t,i}$  are the  $i^{\text{th}}$  signal's magnitude, phase, and bearing, respectively. This expression can be written in matrix form as [76]

$$\mathbf{E}_n \mathbf{V}_V = \mathbf{A}_n, \quad (48)$$

where  $\mathbf{A}_n$  is an  $M \times 1$  vector containing the complex signal snapshot from each node,  $\mathbf{E}_n$  is an  $M \times N_R$  matrix given by

$$\mathbf{E}_n = \begin{bmatrix} \exp(-j\beta x_1 \sin \theta_{t,1}) & \cdots & \exp(-j\beta x_1 \sin \theta_{t,N_R}) \\ \vdots & \ddots & \vdots \\ \exp(-j\beta x_M \sin \theta_{t,1}) & \cdots & \exp(-j\beta x_M \sin \theta_{t,N_R}) \end{bmatrix}, \quad (49)$$

and the  $N_R \times 1$  vector

$$\mathbf{V}_V = \begin{bmatrix} V_{t,1} \exp(j\phi_{t,1}) \\ \vdots \\ V_{t,N_R} \exp(j\phi_{t,N_R}) \end{bmatrix}. \quad (50)$$

Assuming that each signal's bearing is known, an estimate of their magnitude and phase can be obtained using the least-squares approach expressed as [77]

$$\hat{V}_V = \left(E_n^T E_n\right)^{-1} E_n^T A_n. \quad (51)$$

These signal estimates are then used to represent each virtual nodes signal output. The output of each virtual node is expressed as

$$A_v = \sum_{i=1}^{N_R} \hat{V}_{t,i} \exp(j\hat{\phi}_{t,i}) \exp(-j\beta x_v \sin \theta_{t,i}), \quad v = 1, \dots, M_v, \quad (52)$$

where  $x_v$  is the position of the  $v^{\text{th}}$  virtual node along the  $x$ -axis and  $M_v$  is the number of virtual nodes equal to  $d_v / (\lambda / 2)$ .

In this chapter, we covered hyperbolic localization and beamforming within the context of wireless sensor networks. With regard to localization, we presented two localization techniques and their application to an optimal ASLA sensor formation. We also covered the use of outlier detection techniques to mitigate measurement noise. The discussion regarding beamforming focused on techniques to increase array robustness against various steering errors and sidelobe interference. Together, these topics provide the necessary details to present our proposed signal collection scheme in the next chapter.

### III. SOLUTION APPROACH

This chapter begins with an explanation of the operating scenario and assumptions used in this dissertation. We provide an overview of the proposed scheme for radio frequency source localization and signal collection. We then define the figures of merit used to evaluate the scheme's performance.

#### A. PROPOSED SCHEME

The intended operational scenario for the proposed scheme is shown in Figure 16. With a distant, stationary, sporadic or repeating source emitter located at  $(x_t, y_t)$ , there is a network of sensors deployed with the goal of locating the emitter and collecting its signals. In this scenario and in this dissertation research in general, we assume the following. Sensor node deployment is restricted to a circular area, each node has an isotropic antenna with matched polarization, and all nodes are synchronized to a common clock.

The network of  $M$  sensor nodes is initially deployed into an ASLA formation (introduced in Chapter II) where they form an ad hoc wireless sensor network. Each node consists of a multirotor UAV, used to realize the concept of an elevated, mobile sensor network. The ASLA formation shown in Figure 6 places the  $M$  sensor nodes into three node stacks, each containing an equal number of nodes. These three stacks are deployed along the x-axis, one at the origin and the other two flanking the center on both sides at a distance of  $r_a$ . For source localization, this formation is used to minimize the estimate error variance [17], [34]. For signal collection, the node stacks allow for robust signal estimation.

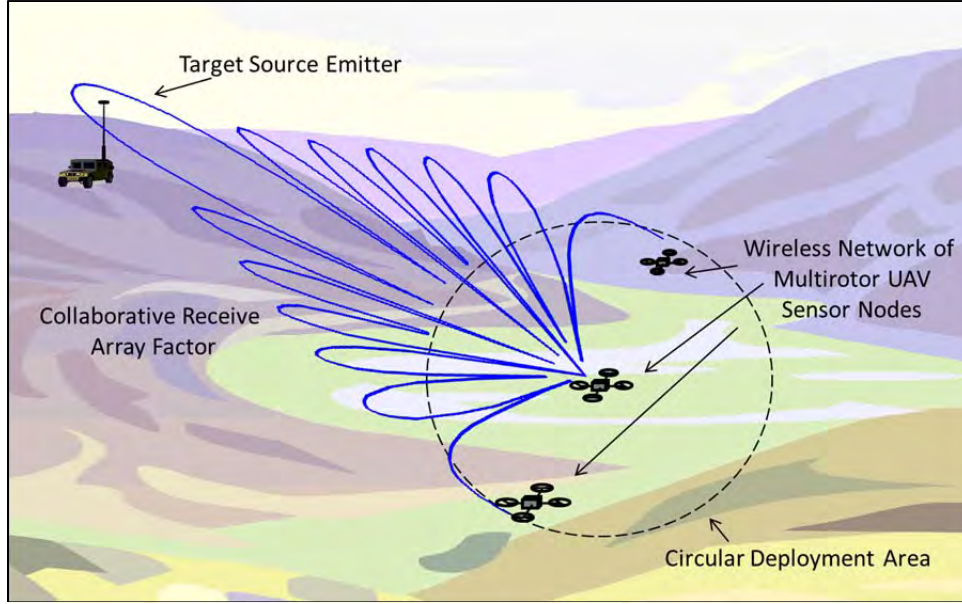


Figure 16. Operational concept of an elevated, mobile sensor network deployed in an ASLA formation.

A schematic diagram of the proposed source localization and signal collection scheme is shown in Figure 17. The scheme begins in the localization phase once a signal has been detected. This generates a set of TDOA measurements that is fed to the location estimator. Using this initial location estimate, we reorient the sensor network to be perpendicular to the target emitter. The objective of this network orientation is to maximize the accuracy of the location estimate, which we call the refined estimate. With the refined estimate obtaining an improved location estimate, this information is used in the signal collection phase. In this phase, each node in the network samples the signal and transmits these samples to the network's sink node. Located in the center of the network, the sink node uses a combination of beamform processing and signal estimation to combine and amplify the signal samples coherently. This makes the signal collection phase essentially a collaborative beamforming effort.

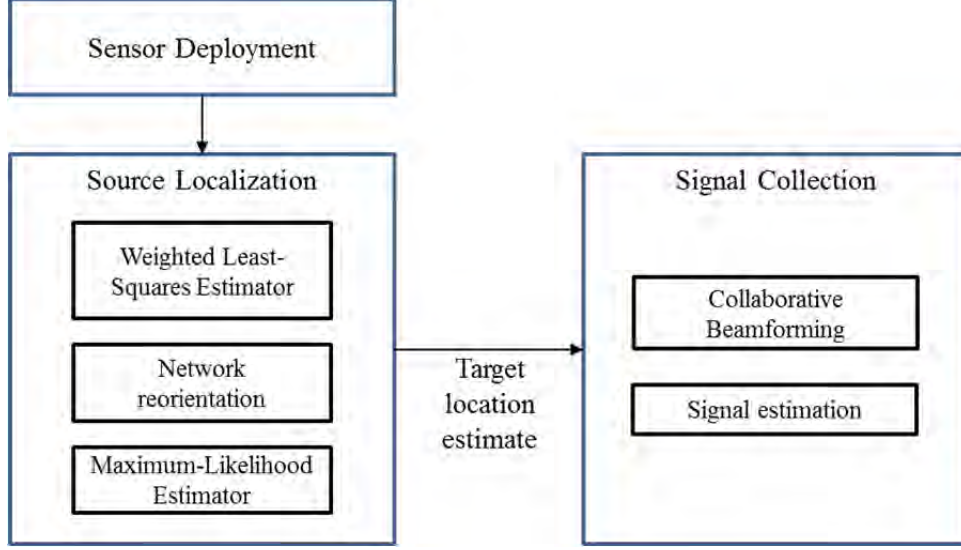


Figure 17. Process flow for propose signal collection scheme.

### 1. Source Localization

The objective of this phase is to obtain a precise location estimate of the target signal emitter. To accomplish this, we employ the use of an unbiased and efficient maximum-likelihood location estimator [52]. Although an effective location estimator, it requires an initial position estimate, in order to avoid local minima solutions [59]. To satisfy this requirement, we precede the maximum-likelihood estimator with another estimator that does not require initialization. For this task, we propose a weighted least-squares estimator.

Furthermore, after obtaining the initial estimate we take advantage of the network's mobility and re-orient the network nodes to create an optimal sensor to target geometry [17]. This new orientation minimizes the geometric dilution of precision [52], thus minimizing the maximum-likelihood estimator's error variance. Because of this further refinement of the location estimate, we term the maximum-likelihood estimator the refining estimator. This two-stage localization technique is illustrated in Figure 18. Starting in the initial configuration shown in Figure 18 (a), we obtain a location estimate  $(\hat{x}_t, \hat{y}_t)$  which is used to calculate the emitter bearing estimate  $\hat{\theta}_t$ . Using  $\hat{\theta}_t$ , we reorient the network nodes perpendicular to the target signal emitter, resulting in the reoriented network configuration as seen in Figure 18 (b).

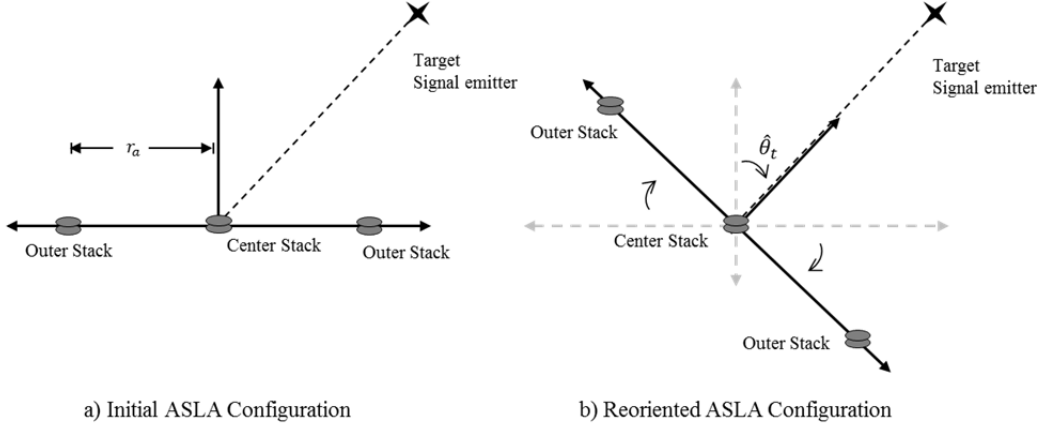


Figure 18. Network reorientation operation for the two-stage localization technique.

In conjunction with both estimators, we propose to implement a robust measurement outlier rejection process to detect and reject erroneous TDOA measurements. This process is used to increase the localization phase's robustness to measurement error and sensor position errors.

## 2. Sensor Node Position Error

In this research, the position information of each node is assumed known. Fluctuations in each node's position due to their station keeping operations are also assumed [47], [48], [78]. The effects of these position errors are the main concern in this dissertation. With each node in the network envisioned as a multirotor UAV, the actual position errors are mainly governed by wind, GPS accuracy, and flight controller scheme [46]–[48]. In the absence of such knowledge we resort to two basic position error distributions, uniform and Gaussian. More specifically, we model these small fluctuations in the  $x$  and  $y$  positions as two independent and identically distributed uniform or Gaussian random variables  $\delta_x$  and  $\delta_y$ , respectively.

For the uniformly distributed position error case, the probability density functions are given by

$$\begin{aligned}
f_{\Delta_x}(\delta_x) &= \frac{1}{2\delta_p}, & -\delta_p \leq \delta_x \leq \delta_p \\
f_{\Delta_y}(\delta_y) &= \frac{1}{2\delta_p}, & -\delta_p \leq \delta_y \leq \delta_p
\end{aligned} \tag{53}$$

where  $\delta_p$  can be interpreted as the maximum position error in the  $x$  or  $y$  direction [48].

For the case of Gaussian position error, both random variables are zero mean with a variance of  $\sigma_p^2$ . The probability density functions are expressed as

$$\begin{aligned}
f_{\Delta_x}(\delta_x) &= \frac{1}{\sqrt{2\pi\sigma_p^2}} \exp\left(-\frac{\delta_x^2}{2\sigma_p^2}\right), & -\infty \leq \delta_x \leq \infty \\
f_{\Delta_y}(\delta_y) &= \frac{1}{\sqrt{2\pi\sigma_p^2}} \exp\left(-\frac{\delta_y^2}{2\sigma_p^2}\right), & -\infty \leq \delta_y \leq \infty
\end{aligned} \tag{54}$$

where  $\sigma_p^2$  is the position error variance in the  $x$  or  $y$  direction [48].

### 3. Collaborative Signal Collection

After the source localization, the objective of the signal collection is to collect and amplify the target signal. The main concern is that, while the mobility of each node is allowed for optimal formations in the localization phase, it will cause array phase errors. To achieve the objective, despite the presence of such errors, we propose a combination of collaborative beamforming and signal estimation.

In this approach, we exploit the sensor grouping of the ASLA formation. The ASLA formation contains three groups of sensors placed symmetrically along the  $x$ -axis (see Figure 6). With each node in a group providing a noisy sample of the same signal, a sample mean can be calculated. Using each group's sample mean in a collaborative phase shift beamformer, we reconstruct and amplify the signal.

Furthermore, since the ASLA formation's array factor contains grating lobes due to its large inter-stack distance  $r_a$ , it is extra sensitive to interfering signals. To increase the robustness of signal collection against such signals, we employ the use of virtual

filling [76]. This array processing technique is used to manage the array's inherent side lobes and grating lobes in order to minimize the effects of interfering signals.

It is important to note that while our scheme is not a traditional adaptive beamformer, it accomplishes the same task. Adaptive beamforming is the process of manipulating an array's weights in order to amplify a target signal while suppressing undesirable signals. Although our approach uses fixed uniform weights, it amplifies a target signal using array rotation and suppresses undesirable signal through the use of virtual filling and tapering techniques.

## B. PERFORMANCE METRICS

With this dissertation heavily focused on parameter estimation, it is critical to define performance metrics as a means to support and analyze the proposed theory and scheme. The performance metrics used throughout this dissertation is defined as follows.

For localization schemes, a widely used performance metric is the Cramer–Rao lower bound (CRLB) [58]. The CRLB is the theoretical minimum solution variance an estimator can achieve. Any unbiased estimator that can achieve the CRLB is said to be efficient [59]. For our proposed network, the CRLB for location (minimum location uncertainty) and bearing (see Chapter II) are expressed as

$$\omega_{CRLB} = \left[ \frac{Mr_a^4}{8\sigma_R^2 c^2 r_t^4} \sin^4 \theta_t \right]^{-1} \quad (55)$$

and

$$\theta_{CRLB} = \left[ \frac{2Mr_a^2}{\sigma_R^2 c^2} \sin^2 \theta_t \right]^{-1}, \quad (56)$$

where  $M$  is the number of sensor,  $r_a$  is the distance between the outer and center node stacks,  $\sigma_R^2$  is the ranging measurement error variance, and  $\theta_t$  is the target source bearing.

For estimation processes, the root mean-square error is a standard performance metric. For source localization, we focus on two root mean-square error values, the first being root mean-square error of location estimates defined as

$$\xi_{loc} = \sqrt{\frac{\sum_{i=1}^{n_t} \|\hat{\omega}_t - \omega_t\|^2}{n_t}}, \quad (57)$$

where  $\omega_t$  is a  $2 \times 1$  vector containing the true source's location,  $\hat{\omega}_t$  is the estimate  $\omega_t$ , and  $n_t$  is the number of trials. The second value is the root mean-square error of bearing estimates defined as

$$\xi_{\theta} = \sqrt{\frac{\sum_{i=1}^{n_t} (\hat{\theta}_t - \theta_t)^2}{n_t}}, \quad (58)$$

where  $\theta_t$  is the true source bearing and  $\hat{\theta}_t$  is its estimate.

For signal estimation, we focus on the root mean-square error of magnitude and phase. The root mean-square error of magnitude estimates is defined as

$$\xi_V = \sqrt{\frac{\sum_{i=1}^{n_t} (\hat{V}_t - V_t)^2}{n_t}}, \quad (59)$$

where  $V_t$  is the true signal magnitude and  $\hat{V}_t$  is its estimate. The root mean-square error of phase estimates is defined as

$$\xi_{\phi} = \sqrt{\frac{\sum_{i=1}^{n_t} (\hat{\phi}_t - \phi_t)^2}{n_t}}, \quad (60)$$

where  $\phi_t$  is the true signal magnitude and  $\hat{\phi}_t$  is its estimate.

To quantify the error in a normalized array factor with and without position errors, we define the normalized array factor error as

$$\psi_{\varepsilon} = \int_0^{2\pi} (A_F(\theta_t) - A_{\varepsilon}(\theta_t))^2 d\theta_t, \quad (61)$$

where  $\theta_t$  is the signal bearing,  $A_F$  is the normalized error free array factor, and  $A_\varepsilon$  is the normalized array factor with position errors.

In this chapter, we provided an overview of the proposed scheme for source localization and signal collection. We described the use of two sequential location estimates that support a follow on signal collection. We then described a set of performance metrics used to analyze the scheme's performance. In the next chapter, we present a two-stage localization technique capable of approaching the CRLB and propose a measurement outlier rejection process to increase localization robustness.

## IV. ROBUST TWO-STAGE SOURCE LOCALIZATION FROM AN AIRBORNE SYMMETRIC LINE ARRAY NETWORK

In this chapter, we introduce a two-stage source localization technique. We examine its performance in the presence of measurement and sensor position errors. To combat these effects, we propose a measurement outlier rejection technique. This technique is used to identify and reject specious TDOA measurements in an effort to increase the localization robustness. We then use simulations to support the theoretical development and analyze the performance.

### A. TWO-STAGE HYPERBOLIC LOCALIZATION

The objective is to estimate the location of a single source emitter located at  $(x_t, y_t)$ . The sensor network is deployed in the initial ASLA configuration, as seen in Figure 18 (a). In this configuration, the network detects an incoming emission and generates a set of TDOA measurements. Using these measurements in the weighted least-squares estimator introduced in Chapter II, we obtain a location estimate. This initial localization is a closed-form estimator that does not require any initialization [5], [79].

#### 1. Hyperbolic Localization via Weighted Least-Squares

The estimator described in this section is derived from the linear array estimators found in [5] and [79], and a generic linear array formation is adapted for use with an ASLA formation.

Since weighted least-squares estimation is primarily for linear models, its applicability to hyperbolic estimation is not immediately obvious. To apply the weighted least-squares approach to localization, we must rewrite (6) to obtain a set of linear equations. To do this, we define the noisy range difference-of-arrival measurement of a sensor pair as [5], [79]

$$d_{i,k} = d_{i,k}^0 + \varepsilon_{i,k}, \quad i, k = 1, \dots, M, \quad (62)$$

where  $d_{i,k}^0$  is the true range difference between sensors  $i$  and  $k$  and  $\varepsilon_{i,k}$  is the zero mean Gaussian range difference measurement error. Then the range from the  $i^{\text{th}}$  sensor to the source emitter is determined as [5]

$$r_i = \sqrt{(x_i - x_t)^2 + (y_i - y_t)^2}. \quad (63)$$

By squaring both sides of (63), we obtain

$$r_i^2 = K_i - 2x_i x_t - 2y_i y_t + x_t^2 + y_t^2, \quad i = 1, \dots, M, \quad (64)$$

where  $K_i = x_i^2 + y_i^2$  and  $r_{i,1} = r_i - r_1$ . In this form, we can formulate a linear weighted least-squares problem in which the sensors are placed in a line. By substituting  $r_i^2 = (r_{i,1} + r_1)^2$  in (64), we get

$$r_{i,1}^2 + 2r_{i,1}r_1 + r_1^2 = K_i - 2x_i x_t - 2y_i y_t + K_t. \quad (65)$$

By co-locating the origin with the first sensor and making it the reference sensor, we get  $r_t = r_1$ , and  $K_t = K_1$ , then (65) can be expressed as

$$r_{i,1}^2 + 2r_{i,1}r_1 = -2x_{i,1}x_t - 2y_{i,1}y_t + K_i - K_1. \quad (66)$$

Finally, with all the sensors in a line, we replace  $-2x_{i,1}x_t - 2y_{i,1}y_t$  by  $-2x_{i,1}(x_t + \alpha_t y_t)$  where  $\alpha_t$  is some constant. With this substitution, (66) becomes

$$r_{i,1}^2 - K_i + K_1 = -2x_{i,1}(x_t + \alpha_t y_t) - 2r_{i,1}r_1. \quad (67)$$

With (67) now linear in  $r_1$  and  $(x_t + \alpha_t y_t)$ , a weighted least-squares solution can be obtained as [5], [79]

$$\hat{\boldsymbol{\omega}}_{WLS} = \begin{bmatrix} (\hat{x}_t + \alpha_t \hat{y}_t) \\ \hat{r}_t \end{bmatrix} = (\mathbf{G}_l^T \mathbf{C}_\varepsilon^{-1} \mathbf{G}_l)^{-1} \mathbf{G}_l^T \mathbf{C}_\varepsilon^{-1} \mathbf{h}, \quad (68)$$

where

$$\mathbf{G}_l = \begin{bmatrix} x_{2,1} & r_{2,1} \\ x_{3,1} & r_{3,1} \\ \vdots & \vdots \\ x_{M,1} & r_{M,1} \end{bmatrix}, \quad \mathbf{h} = \begin{bmatrix} r_{2,1}^2 - x_2^2 \\ r_{3,1}^2 - x_3^2 \\ \vdots \\ r_{M,1}^2 - x_M^2 \end{bmatrix},$$

and  $\mathbf{C}_\varepsilon^{-1}$  is the inverse covariance matrix of the TDOA measurement vector from (62).

When all the sensors are located on the x-axis,  $y_{i,1} = 0$  for  $i = 2, \dots, M$ , resulting in  $\alpha_t = 0$ . The solution is then expressed as

$$\hat{\boldsymbol{\omega}}_{WLS} = \begin{bmatrix} \hat{x}_t \\ \hat{r}_t \end{bmatrix} = (\mathbf{G}_l^T \mathbf{C}_\varepsilon^{-1} \mathbf{G}_l)^{-1} \mathbf{G}_l^T \mathbf{C}_\varepsilon^{-1} \mathbf{h}. \quad (69)$$

Using (69), we calculate the y-coordinate estimate using the expression

$$\hat{y}_t = \sqrt{\hat{r}_t^2 - x_t^2}. \quad (70)$$

Using the initial estimate  $\hat{\boldsymbol{\omega}}_{WLS}$ , we see that the network reorients itself into a desired ASLA formation, as seen in Figure 18 (b). In this configuration, the effect of GDOP is minimized, thus minimizing the estimate's CRLB [34]. To take full advantage of the new formation and its minimized CRLB, we propose the use of a maximum-likelihood estimator introduced in Chapter II. This estimator is unbiased and asymptotically efficient, i.e., it achieves the CRLB [59].

## 2. Hyperbolic Localization via Maximum-Likelihood Estimation

The estimator described in this section is derived from the generic TDOA estimator found in [52] but here is adapted for use with an ASLA formation in polar coordinates.

Introduced in Chapter II, the maximum-likelihood estimator has been shown to be unbiased and asymptotically efficient [59]. Its extension to hyperbolic localization is done in a similar fashion to that of the weighted least-squares estimator. We rewrite (13) to account for time-of-arrival measurements as

$$\mathbf{t} = t_0 \mathbf{I}_M + \mathbf{D} / c + \boldsymbol{\varepsilon} \quad (71)$$

where  $\mathbf{D}$  is an  $M \times 1$  vector containing the range from the emitter to each node,  $t_0$  is the time of signal emission,  $\mathbf{I}_M$  is an  $M \times 1$  vector of ones, and  $\boldsymbol{\varepsilon}$  is an  $M \times 1$  vector containing the TOA measurement errors. To convert the TOAs to TDOAs, we subtract the  $i^{\text{th}}$  TOA measurement from the first TOA measurement to eliminate  $t_0$ . This results in

$$t_1 - t_i = t_0 - t_0 + (D_1 - D_i) / c + \varepsilon_1 - \varepsilon_i. \quad (72)$$

To put it in matrix form, we multiply (71) by the  $(M-1) \times M$  matrix [52]

$$\mathbf{G}_M = \begin{bmatrix} 1 & -1 & 0 & \cdots & 0 \\ 1 & 0 & -1 & \ddots & \vdots \\ \vdots & \vdots & \ddots & \ddots & 0 \\ 1 & 0 & \cdots & 0 & -1 \end{bmatrix} \quad (73)$$

to get

$$\mathbf{y}_{TD} = \mathbf{G}_M \mathbf{D} / c + \mathbf{G}_M \boldsymbol{\varepsilon}. \quad (74)$$

where  $\mathbf{y}_{TD} = \mathbf{G}_M \mathbf{t}$  is an  $(M-1) \times 1$  vector containing all the resulting time-difference-of-arrival measurements.

From (18), we set  $\boldsymbol{\omega}_r = \hat{\boldsymbol{\omega}}_{WLS}$ , and the maximum-likelihood estimator's solution in polar coordinates can be expressed as [52]

$$\hat{\boldsymbol{\omega}}_{ML} = \begin{bmatrix} \hat{r}_t \\ \hat{\theta}_t \end{bmatrix} = \hat{\boldsymbol{\omega}}_{WLS} + c \left( \mathbf{H}^T \mathbf{G}_M^T \mathbf{C}_\varepsilon^{-1} \mathbf{G}_M \mathbf{H} \right)^{-1} \mathbf{H}^T \mathbf{G}_M^T \mathbf{C}_\varepsilon^{-1} \left( \mathbf{y}_{TD} - (\mathbf{G}_M \mathbf{D}_0) / c \right), \quad (75)$$

where  $\hat{\boldsymbol{\omega}}_{WLS}$  is the weighted least-squares estimate in polar coordinates,  $\mathbf{D}_0$  is the  $(M-1) \times 1$  vector containing the distances between the reference point and the sensor nodes and  $\mathbf{H}$  is the  $(M-1) \times 2$  matrix expressed as

$$\mathbf{H} = \begin{bmatrix} \frac{r_m - r_r \cos(\theta_m - \theta_r)}{D_{0,m}} & \frac{r_m r_r \sin(\theta_m - \theta_r)}{D_{0,m}} \\ \vdots & \vdots \\ \frac{r_M - r_r \cos(\theta_M - \theta_r)}{D_{0,M}} & \frac{r_M r_r \sin(\theta_M - \theta_r)}{D_{0,M}} \end{bmatrix}, \quad m = 2, \dots, M, \quad (76)$$

with  $r_m$  and  $\theta_m$  the  $m^{\text{th}}$  node's range and bearing, respectively,  $r_r$  and  $\theta_r$  are the reference point's range and bearing, respectively,  $D_{0,m}$  the  $m^{\text{th}}$  element of  $\mathbf{D}_0$ , and the product  $\mathbf{G}_M \mathbf{H}$  the hyperbolic version of (17).

## B. LOCALIZATION PERFORMANCE

A series of Monte Carlo simulations to support proposed localization technique is presented in this section. The results of the simulation are based on 10,000 trials each. For each simulation, the ASLA configuration is arranged in accordance with Figure 18, with  $r_a = 200$  m and  $N_s = 5$ . Note, since TDOA measurements are typically on the order of nanoseconds, for convenience, we use range difference-of-arrival (RDOA), i.e., the TDOA measurement weighted by the signal propagation speed  $c$ , which is typically on

the order of meters. This substitution is used only as a means to simplify the simulation results and does not affect the theory in any way.

In Figure 19, the root mean-square error of location estimate  $\xi_{loc}$  for both the initial and refined localization are compared against their corresponding CRLB as a function of RDOA noise variance  $\sigma_{RD}^2 = c^2 \sigma_R^2$ . In this simulation,  $N_s = 5$ , the emitter is located at  $\omega_t = [2500 \text{ m}, 45 \text{ deg}]^T$ ,  $r_a = 200 \text{ m}$ , and each data point is the result of 10,000 trials. From the results, we see that the  $\xi_{loc}$  of both the initial and refined estimates increase rapidly with noise. As expected, the  $\xi_{loc}$  of the refined estimate outperforms the initial estimate at all values of noise simulated. Also, we can see that the refined estimator using a maximum-likelihood estimate approaches the CRLB up to approximately 0 dB. It is important to note that the maximum-likelihood estimate is asymptotically efficient [15], but here, using the ASLA formation, it approaches the CRLB in one iteration.

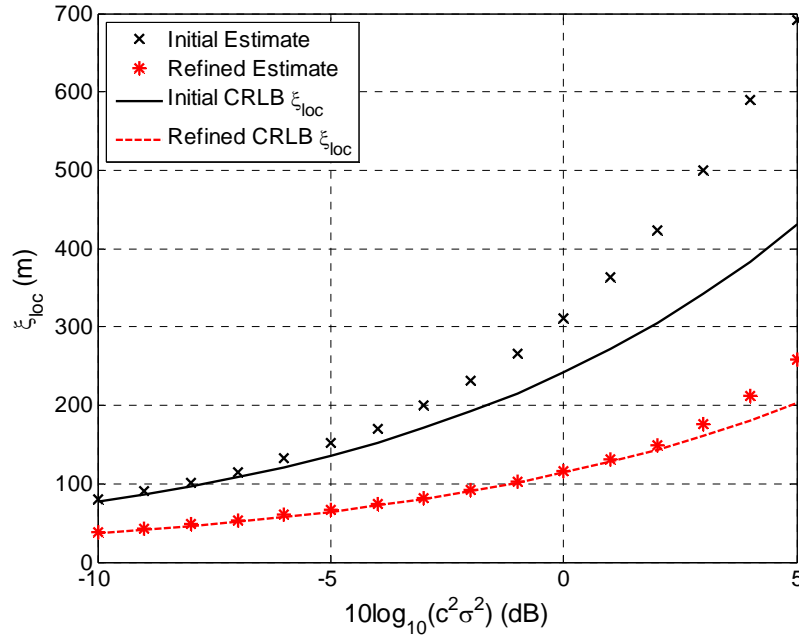


Figure 19. Root mean-square error  $\xi_{loc}$  of the initial (black) and refined (red) localizations versus RDOA noise. Result based on 10,000 trials,  $N_s = 5$ ,  $r_a = 200 \text{ m}$ , and  $\omega_t = [2500 \text{ m}, 45 \text{ deg}]^T$ .

A plot of the angular root mean-square error  $\xi_\theta$  for both the initial and refined localization as a function of  $\sigma_{RD}^2$  is provided in Figure 20. In this simulation,  $N_s = 5$ , the emitter is located at  $\boldsymbol{\omega}_t = [2500 \text{ m}, 45 \text{ deg}]^T$ ,  $r_a = 200 \text{ m}$ , and each data point is the result of 10,000 trials. The y-axis is  $\xi_\theta$  in radians, and the x-axis is RDOA noise in dB. From the results, we observe that the same trends as in Figure 19. From (56), we know that the ASLA formation yields an accurate bearing estimate. This is validated by the simulation results with the refined estimator's  $\xi_\theta = -0.25 \times 10^{-3} \text{ rad}$  at  $-10 \text{ dB}$  RDOA noise. The initial bearing estimate is just shy of CRLB, while the refined maximum-likelihood estimate approaches it at all simulated values. As with the  $\xi_{loc}$  estimate, the maximum-likelihood estimator also approaches the CRLB in one iteration.

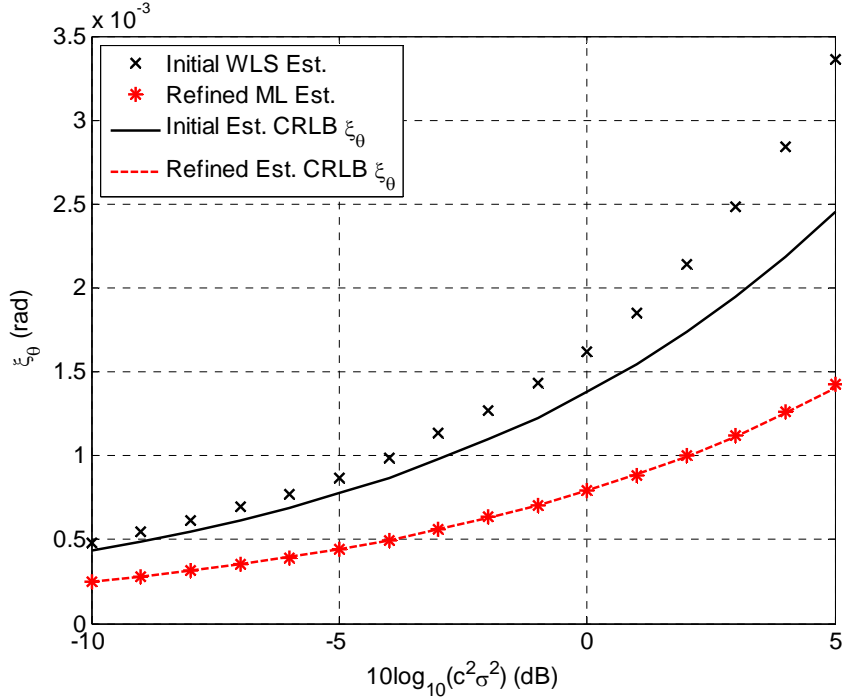


Figure 20. RMSE  $\xi_\theta$  of the initial (black) and refined (red) localizations versus RDOA noise. Result based on 10,000 trials,  $N_s = 5$ ,  $r_a = 200 \text{ m}$ , and  $\boldsymbol{\omega}_t = [2500 \text{ m}, 45 \text{ deg}]^T$ .

We plot both the initial and refined localization's  $\xi_{loc}$  values in Figure 21 as a function of sensors per stack  $N_s$ . Each estimator's CRLB is also included for comparison. In this simulation,  $\sigma_{RD}^2 = 0$  dB, the emitter is located at  $\omega_t = [2000 \text{ m}, 30 \text{ deg}]^T$ ,  $r_a = 200$  m, and each data point is the result of 10,000 trials. From the results, we see that the  $\xi_{loc}$  of the initial estimate approaches the CRLB at  $N_s = 2$  but quickly diverges from it. In contrast, the  $\xi_{loc}$  of the refined estimate does not approach the CRLB until  $N_s > 5$ . It is interesting to note that an increasing  $N_s$  improves the performance of the refined estimate at a higher rate than the initial estimate.

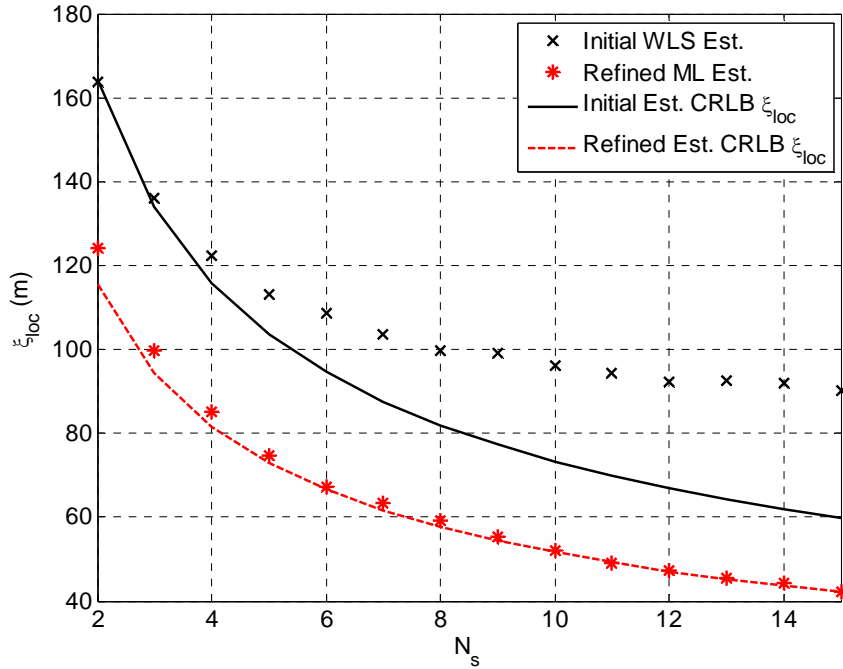


Figure 21. Root mean-square error  $\xi_{loc}$  of the initial (black) and refined (red) localizations versus  $N_s$ . Results based on 10,000 trials with  $\sigma_{RD}^2 = 0$  dB,  $N_s = 5$ ,  $r_a = 200$  m, and  $\omega_t = [2000 \text{ m}, 30 \text{ deg}]^T$ .

A comparison of both the initial and refined localization's  $\xi_\theta$  values is shown in Figure 22 as a function of sensors per stack  $N_s$ . In this simulation,  $\sigma_{RD}^2 = 0$  dB, the

emitter is located at  $\omega_t = [2000 \text{ m}, 30 \text{ deg}]^T$ ,  $r_a = 200 \text{ m}$ , and each data point is the result of 10,000 trials. From the results, we see that the  $\xi_\theta$  of the initial estimate is always just shy of the CRLB for all values of  $N_s$  simulated. Conversely, the  $\xi_\theta$  of the refined estimate approaches the CRLB for all values of  $N_s$  simulated. These results suggest that the refined maximum-likelihood estimator is a good candidate for bearing estimates regardless of the number of sensors employed.

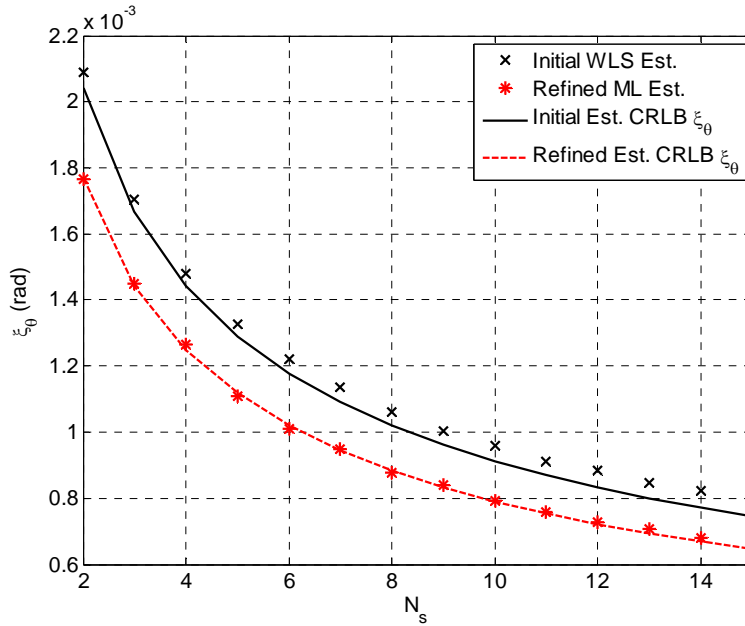


Figure 22. Root mean-square error  $\xi_\theta$  of the initial (black) and refined (red) localizations versus  $N_s$ . Results based on 10,000 trials with  $\sigma_{RD}^2 = 0 \text{ dB}$ ,  $N_s = 5$ ,  $r_a = 200 \text{ m}$ , and  $\omega_t = [2000 \text{ m}, 30 \text{ deg}]^T$ .

In Figure 23, both the initial and refined localization's  $\xi_{loc}$  are plotted as a function of the emitter's bearing. In this simulation,  $\sigma_{RD}^2 = 0 \text{ dB}$ , the emitter is located at  $\omega_t = [2000 \text{ m}, \theta_t]^T$ ,  $r_a = 200 \text{ m}$ , and each data point is the result of 10,000 trials. From the results, it is clear that the initial and refined estimator's performance is dependent on the target's bearing (relative to the initial array configuration). The initial estimate

follows the CRLB as seen in (55), while the refined estimate improves the  $\xi_{loc}$  within the range of  $-40 \leq \theta_t \leq 40$  deg. From (55), we see that  $\xi_{loc}$  approaches infinity as  $\theta_t$  approaches  $\pm 90$  deg. This suggests that the initial estimate requires some knowledge of the target bearing *a priori* to insure a sufficiently accurate initialization for the refined estimate. In other words, if the emitter bearing is greater than  $\pm 40$  deg, the initial estimate is insufficient in setting up the follow-on refined estimate. If this is not possible, the initial estimate can be obtained using estimators that are independent of  $\theta_t$  such as the ones in [5] and [80]. Note that these estimators require a random positioning of the sensor nodes and are not applicable to an ASLA configuration.

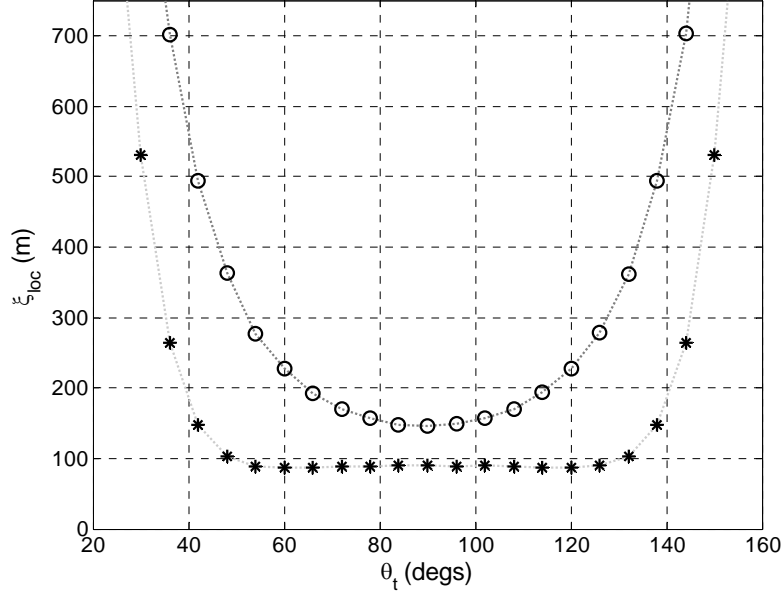


Figure 23. Root mean-square error  $\xi_{loc}$  of the initial (o) and refined (\*) localizations versus  $\theta_t$ . Results based on 10,000 trials with  $\sigma_{RD}^2 = 0$  dB,  $N_s = 5$ ,  $r_a = 200$  m, and  $r_t = 2000$  m.

### 1. Performance of the Localization Scheme in the Presence of Uniform Position Errors

This research envisions the use of multirotor UAVs to realize an elevated, mobile WSN. As such, it is necessary to address the position errors induced by the UAV's

unsteady station-keeping operations. This unsteadiness is mainly due to wind [46] and causes nodes to momentarily deviate from their given positions. In this section, we model these position errors as two uniformly distributed random variables  $\delta_x$  and  $\delta_y$ , each bounded by  $\delta_p$ . The true distribution of position errors for any given UAV is determined by many factors such as GPS accuracy, wind effect, and flight controller [38]. In the absence of such knowledge, we resort to a basic distribution in order to complete our analysis. The effects of these position errors are illustrated in Figure 24 through Figure 27.

A comparison of the initial localization's root mean squared location error  $\xi_{loc}$  and bearing error  $\xi_\theta$  with and without position errors is shown in Figure 24 and Figure 25 as a function of the maximum position error  $\delta_p$  (see (53)). In this simulation,  $\sigma_{RD}^2 = 0$  dB, the emitter is located at  $\omega_t = [2000 \text{ m}, 30 \text{ deg}]^T$ ,  $r_a = 200 \text{ m}$ , and each data point is the result of 10,000 trials. From the plots, we see that the root mean squared location error monotonically increases with  $\delta_p$ , both in location and bearing estimates.

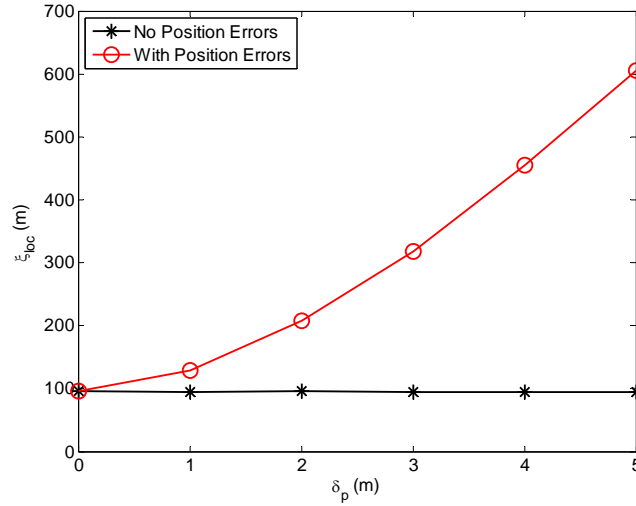


Figure 24. Initial localization's root mean-square error  $\xi_{loc}$  with no position errors (black) and with position errors (red) versus maximum uniform position error  $\delta_p$ . Results based on 10,000 trials with  $\sigma_{RD}^2 = 0$  dB,  $N_s = 5$ ,  $r_a = 200 \text{ m}$ , and  $\omega_t = [2000 \text{ m}, 30 \text{ deg}]^T$ .

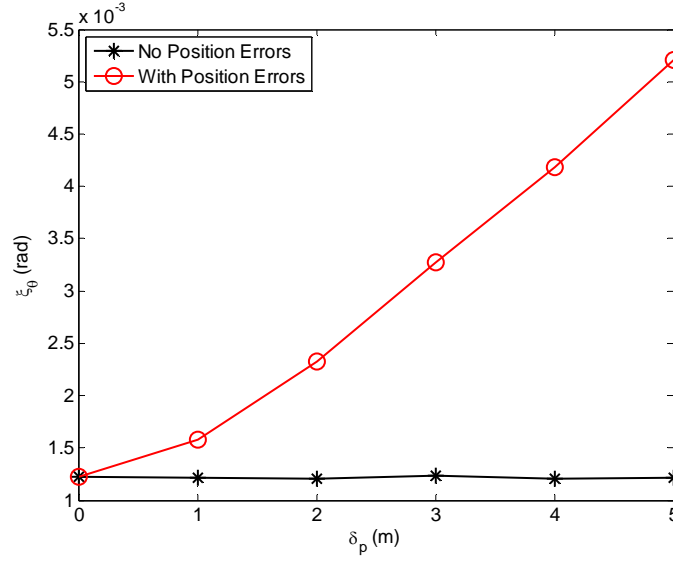


Figure 25. Initial localization's root mean-square error  $\xi_\theta$  with no position errors (black) and with position errors (red) versus maximum uniform position error  $\delta_p$ . Results based on 10,000 trials with  $\sigma_{RD}^2 = 0$  dB,  $N_s = 5$ ,  $r_a = 200$  m, and  $\omega_t = [2000 \text{ m}, 30 \text{ deg}]^T$ .

Similar to Figure 24 and Figure 25, the performance of the refined localization as a function of  $\delta_p$  is shown in Figure 26 and Figure 27. In this simulation,  $\sigma_{RD}^2 = 0$  dB, the emitter is located at  $\omega_t = [2000 \text{ m}, 30 \text{ deg}]^T$ ,  $r_a = 200$  m, and each data point is the result of 10,000 trials. From the results, we see that the refined maximum-likelihood estimate is more resilient against position error with an almost linear response to  $\delta_p$ . Specifically, we see in Figure 26 that for  $\delta_p = 1$  m,  $\xi_{loc}$  only increases by approximately 50 m. Overall, these results suggest that position errors play a significant role in the accuracy of localization using a mobile network. In the next section, we address these errors using a measurement outlier rejection process.

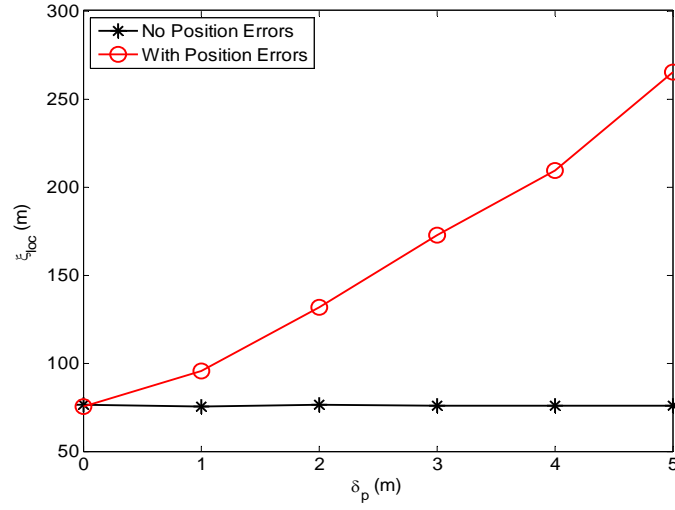


Figure 26. Refined localization's root mean-square error  $\xi_{loc}$  with no position errors (black) and with position errors (red) versus maximum uniform position error  $\delta_p$ . Results based on 10,000 trials with  $\sigma_{RD}^2 = 0$  dB,  $N_s = 5$ ,  $r_a = 200$  m, and  $\omega_t = [2000 \text{ m}, 30 \text{ deg}]^T$ .

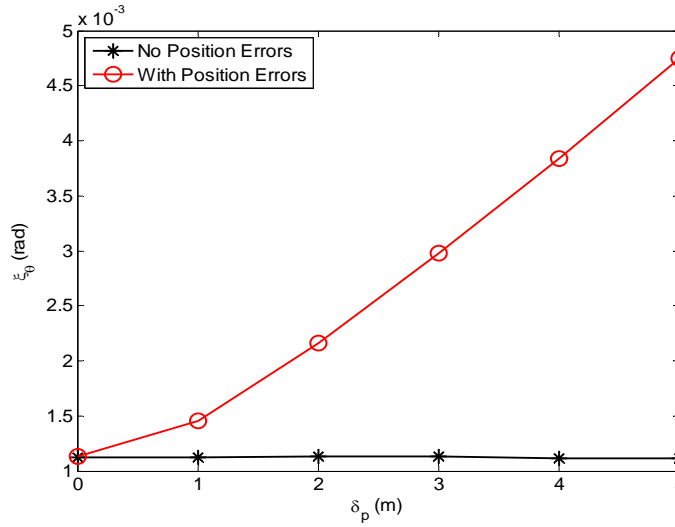


Figure 27. Refined localization's root mean-square error  $\xi_\theta$  with no position errors (black) and with position errors (red) versus maximum uniform position error  $\delta_p$ . Results based on 10,000 trials with  $\sigma_{RD}^2 = 0$  dB,  $N_s = 5$ ,  $r_a = 200$  m, and  $\omega_t = [2000 \text{ m}, 30 \text{ deg}]^T$ .

### C. ROBUST SIGNAL LOCALIZATION VIA MEASUREMENT OUTLIER REJECTION

With the goal of improving the robustness of the source localization technique, we propose a measurement outlier rejection process to improve localization noise performance. This includes resilience to increased signal noise, sensor position errors, and measurement outliers. These improvements leverage the existing outlier detection techniques to identify and remove specious measurement data, i.e., measurements that seem benign but in actuality degrade the estimate's accuracy. The basic premise is to determine the effect each measurement has on the end solution as a means to identify and remove measurement outliers. In this research, we define a measurement outlier as a measurement taken with a variance greater than a specified multiple of the expected variance.

#### 1. Robust Hyperbolic Localization via Measurement Outlier Rejection

When trying to detect the presence of outliers in a data set containing location estimates, the simplest methodology is to calculate each sample's Euclidean distance from the sample mean. The problem with this approach is that outliers heavily influence the sample mean, making it a poor discriminator of outliers [18]. Another approach is to use a statistical hypothesis test to determine the likelihood that the data set is derived from a single distribution [55]; however, this approach is more suited to problems with larger data sets ( $> 30$  samples per stack) [55], which is not appropriate for our scheme.

##### *a. Measurement Outlier Rejection via the Mahalanobis Distance*

Since the localization technique is focused on a small sample size, the use of hypothesis testing to identify outliers is limited. An alternative approach is the Mahalanobis distance. This approach performs well with small sample sizes and is less affected by the presence of outliers [18]. In contrast to the Euclidean distance, the Mahalanobis distance calculates the distance from the mean but does so in a manner that accounts for the samples distribution, i.e., its covariance matrix. Given  $N_{sc}$  location estimates, the corresponding Mahalanobis distance is defined as [18]

$$d_{M,i} = (\mathbf{v}_i - E\{\mathbf{v}_\omega\}) \mathbf{C}_\omega^{-1} (\mathbf{v}_i - E\{\mathbf{v}_\omega\})^T, \quad (77)$$

where the  $\mathbf{v}_\omega$  is the  $N_{sc} \times 2$  matrix containing all the location estimates,  $\mathbf{v}_i$  is the  $1 \times 2$  vector containing the  $i^{\text{th}}$  location estimate, and  $\mathbf{C}_\omega$  is the  $2 \times 2$  covariance matrix of  $\mathbf{v}_\omega$ . In the proposed rejection process, we use the Mahalanobis distance of the weighted least-squares solution to determine the best and worst candidate measurements for use in the final location estimate. In this approach, we use single case diagnostics [18] to derive multiple weighted least-squares estimates from one set of TDOA measurements. For ASLA configured network, the number of single cases for a given signal measurement is  $N_{sc} = M - 1$ .

A classic tool for the detection of statistical outliers in least-square estimation problems, single case diagnostics provide a methodology to single out measurements that lead to strong deviations in the end solution [18]. In this approach, a single measurement from a set is removed, and the corresponding weighted least-squares solution is calculated. This process is repeated until each measurement is treated in the same fashion. The Mahalanobis distance of each solution is then calculated using the mean and covariance of the entire  $N_{sc}$  set of solutions. The solutions with high Mahalanobis distance values suggest that an influential measurement was removed. Such measurements are termed leverage points [18]. Conversely, if the Mahalanobis distance value was low, then the measurement in question is considered valid.

#### ***b. Distribution of the Mahalanobis Distance***

With a measure of solution divergence now obtained, the next step is to be able to discern which values of this divergence represent outliers and which represent valid measurements. This process amounts to setting a Mahalanobis distance value outlier threshold. To calculate a suitable threshold value, we consider the distribution of the Mahalanobis distance values with and without outliers. Given a set of location estimates that are Gaussian with a known mean and covariance matrix, the distribution of the Mahalanobis distance values follow a Chi-squared distribution [81]. The Chi-squared

distribution is the resulting distribution for the sum of multiple squared Gaussian random variables. The Chi-squared distribution can be expressed by its degrees of freedom  $p$ , which is the number of squared Gaussian random variables present in the sum. The Chi-squared distribution of the Mahalanobis distance is expressed as [55]

$$f_{D_M}(d_M) = \frac{1}{2^{p/2} \Gamma(p/2)} \exp(-d_M/2) (d_M)^{p/2-1} \quad \text{for } 0 \leq d_M < \infty, \quad (78)$$

where  $\Gamma$  is the gamma function defined as

$$\Gamma(\tau) = \int_0^{\infty} x^{\tau-1} e^{-x} dx \quad \text{for } \tau > 0. \quad (79)$$

The cumulative distribution function is defined as

$$F_{D_M}(d_M | p) = \int_0^{d_M} \frac{x^{(p-2)/2} e^{-x/2}}{2^{p/2} \Gamma(p/2)} dx \quad (80)$$

and the corresponding means and variance are expressed as [55]

$$\begin{aligned} E\{d_M\} &= p, \\ \sigma_{d_M}^2 &= 2p. \end{aligned} \quad (81)$$

Given that our scenario considers a small number of outliers, we hypothesize that the distribution of the Mahalanobis distance with and without outliers is significantly similar.

To validate this hypothesis, a comparison of Mahalanobis distance values and their estimated distribution are shown in Figure 28. In this simulation, using (69), the histogram of 100 Mahalanobis distance values with and without outliers is shown. The Chi-squared probability density functions were plotted using the sample mean. In the outlier case, there are 15 outliers present with a variance five times larger than the expected variance. In both cases, the estimated degrees of freedom was  $p = 1.98$ . These

results help support the claim that the estimated probability density function of the Mahalanobis distance approximates the Chi-squared with or without a small amount of outliers present.

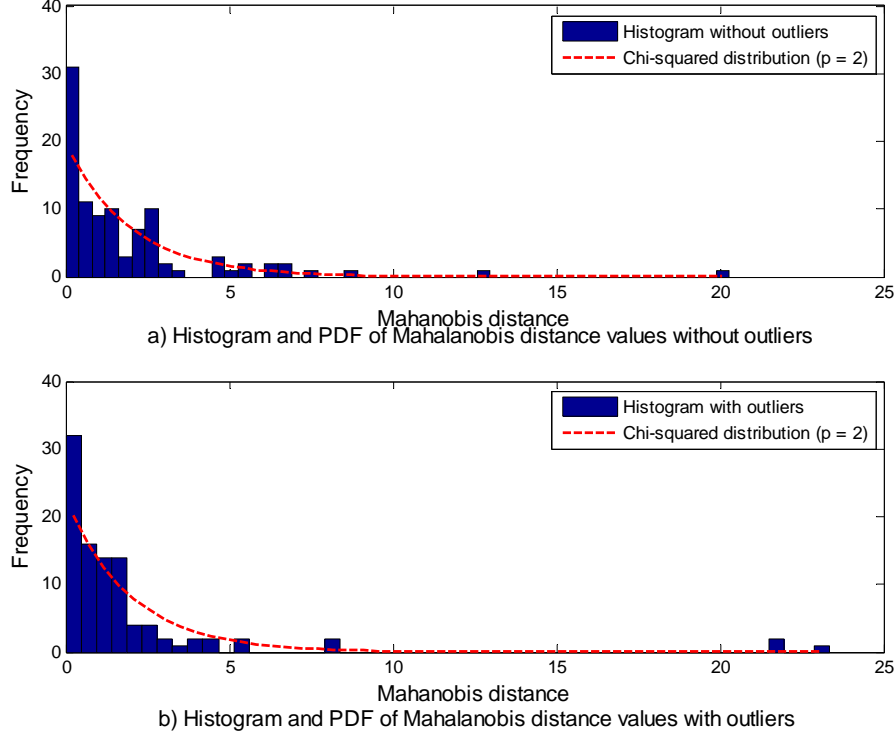


Figure 28. Comparison of histogram and Chi-squared probability density function of Mahalanobis distances.

### c. *Outlier Rejection Threshold*

Using the previous results to support our hypothesis, we next determine the outlier rejection threshold. A standard criterion for outlier rejection thresholds is the Tukey criteria for anomalies [82]. This criterion states that in a given range of data points, values at the extreme ends of the data set are considered outliers. To quantify the threshold, Tukey [82] proposed the following criterion. Taking the difference between the 25<sup>th</sup> and 75<sup>th</sup> percentile of a data set as the interquartile range [82]

$$Q_{IR} = Q_{75\%} - Q_{25\%} \quad (82)$$

we consider any data point greater than  $Q_{75\%} + (3/2) Q_{IR}$  as an outlier [82]. It is important to note that this criterion makes no consideration on the data's distribution. To incorporate knowledge of the data set distribution, we propose the use of Horn's algorithm [83].

Horn's algorithm begins with the estimation of a data set's distribution. Next, the Tukey criterion threshold is determined using the estimated cumulative distribution function. Then, all data points greater than the calculated threshold are removed from the data set [83]. Overall, assuming the distribution of the Mahalanobis distance values is Chi-squared, the interquartile range is determined by [83]

$$Q_{IR} = F^{-1}(0.75|p) - F^{-1}(0.25|p), \quad (83)$$

where the  $F^{-1}$  is the inverse Chi-squared cumulative distribution function. The outlier threshold using Horn's algorithm can then be expressed as [82] [83]

$$T_{O_{MD}} = F^{-1}(0.75|p) + (3/2)Q_{IR}. \quad (84)$$

Using the outlier rejection process in conjunction with our proposed localization, we wish to minimize the effects of TDOA measurement noise, position errors, and measurement outliers. We term an estimator using this process a robust estimator.

## 2. Performance of the Robust Localization in the Presence of Measurement Outliers

To support the proposed outlier rejection process, we examine the results of four Monte Carlo simulations. Each simulation evaluates the robust localization estimator's performance in the presence of random measurement outliers. Each simulation uses a 15 node ASLA configured network in which the emitter is located at  $\omega_t = [2000 \text{ m}, 30 \text{ deg}]^T$ .

A comparison of the robust and regular weighted least-squares estimator's root mean-square error  $\xi_{loc}$  as a function of  $\sigma_{RD}^2 = c^2 \sigma_R^2$  is shown in Figure 29. In this simulation, there are no measurement outliers present,  $N_s = 5$ , the emitter is located at  $\omega_i = [2000 \text{ m}, 30 \text{ deg}]^T$ ,  $r_a = 200 \text{ m}$ , and each data point is the result of 10,000 trials. The results show that the robust estimator's  $\xi_{loc}$  is only slightly higher than the regular estimator at low noise levels. In contrast, the robust estimator outperforms the regular estimator at high noise levels. Overall, this result validates the effectiveness of the rejection process against high measurement noise.

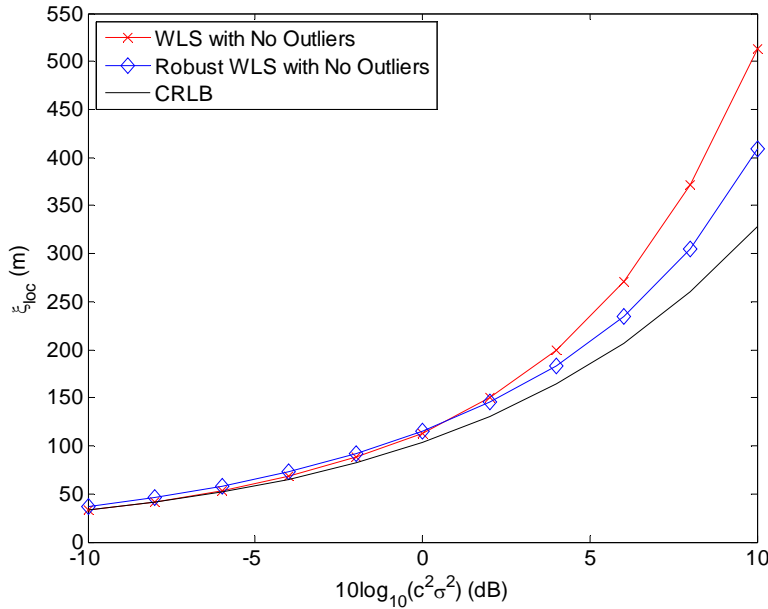


Figure 29. Root mean-square error  $\xi_{loc}$  of the weighted least-squares (red) and robust weighted least-squares (blue) versus RDOA noise variance. No outliers. Results based on 10,000 trials with  $N_s = 5$ ,  $r_a = 200 \text{ m}$ , and  $\omega_i = [2000 \text{ m}, 30 \text{ deg}]^T$ .

In Figure 30, the robust weighted least-squares estimator's  $\xi_{loc}$  is compared against its corresponding CRLB at increasing RDOA noise values. In this simulation, there are two random measurement outliers with a RDOA noise variance that is five times greater than the remaining set of measurements. Also,  $N_s = 5$ , the emitter is

located at  $\omega_t = [2000 \text{ m}, 30 \text{ deg}]^T$ ,  $r_a = 200 \text{ m}$ , and each data point is the result of 10,000 trials. The y-axis is  $\xi_{loc}$  in meters, and the x-axis is RDOA noise variance in dB. The results show that the effects of the outliers are almost negligible at the lower levels of RDOA noise ( $< -5 \text{ dB}$ ). The robust weighted least-squares estimator outperforms the weighted least-squares estimate at all simulated noise levels, with significant improvements occurring at RDOA noise level above  $-2 \text{ dB}$ . Of interest is the robust estimator's performance above  $6 \text{ dB}$ , where it again outperforms the no outlier case. This result validates the effectiveness of the proposed outlier rejection process for a wide range of measurement noise, with or without outliers present.

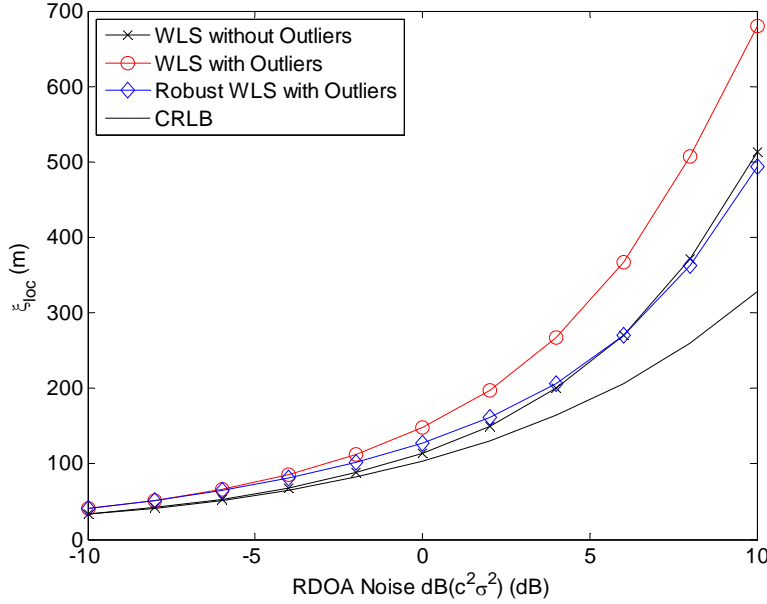


Figure 30. Root mean-square error  $\xi_{loc}$  of the weighted least-squares estimator with outliers (red), weighted least-squares estimator without outliers (black), and robust weighted least-squares estimator with outliers (blue) versus RDOA noise variance. Results based on 10,000 trials with  $N_s = 5$ ,  $r_a = 200 \text{ m}$ , and  $\omega_t = [2000 \text{ m}, 30 \text{ deg}]^T$ . In the outlier cases there were two random outliers present at a RDOA noise variance five times  $\sigma_{RD}^2$ .

The results of two Monte Carlo simulations illustrating the robust weighted least-squares estimator's performance as a function of the number of random outliers present and their variance are shown in Figure 31 and Figure 32.

A plot of the robust and regular weighted least-squares estimator  $\xi_{loc}$  is shown in Figure 31 as a function of the number of random outliers present. In this simulation,  $N_s = 5$ , the emitter is located at  $\omega_t = [2000 \text{ m}, 30 \text{ deg}]^T$ ,  $r_a = 200 \text{ m}$ ,  $\sigma_{RD}^2 = 0 \text{ dB}$ , the outlier variance is five times larger than the expected variance, and each data point is the result of 10,000 trials. From the results, we see that the increase in  $\xi_{loc}$  of both the regular and robust estimate is almost linear, with the robust estimator having a slower rate of increase. This result suggests that the performance increase of the robust estimator is a function of the number of outliers present. As the number of outliers increases, the more of them are rejected.

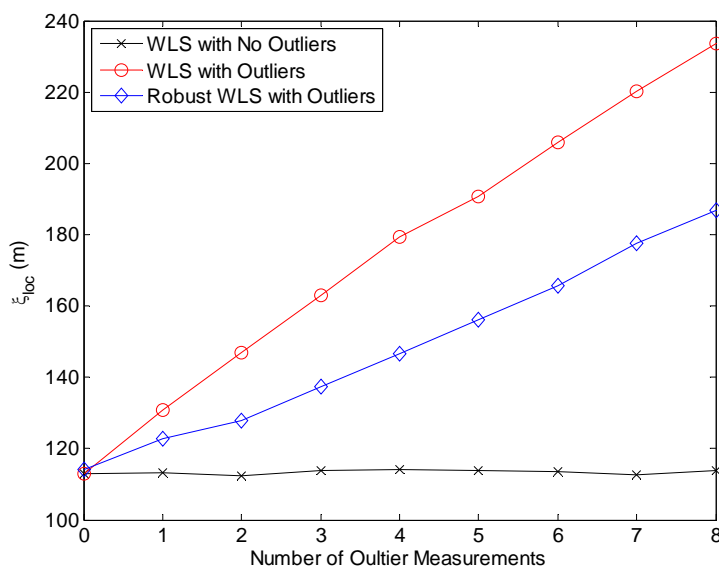


Figure 31. Root mean-square error  $\xi_{loc}$  of the weighted least-squares estimator with outliers (red), weighted least-squares estimator without outliers (black), and robust weighted least-squares estimator with outliers (blue) versus number of outliers. Results based on 10,000 trials with  $N_s = 5$ ,  $r_a = 200 \text{ m}$ , and  $\omega_t = [2000 \text{ m}, 30 \text{ deg}]^T$ . In the outlier cases their RDOA noise variance is five times  $\sigma_{RD}^2$ .

A comparison of the robust and regular weighted least-squares estimator's  $\xi_{loc}$  values as a function of outlier variance gain is shown in Figure 32. In this simulation, the parameters are similar to the ones used to create Figure 31. From the results, we see that the increase in  $\xi_{loc}$  approaches a maximum at variance multiplier greater than ten. Since each outlier is derived with a larger variance, they are easier to identify and be removed, thus we see a plateauing effect on the  $\xi_{loc}$ . This also suggests that above a certain variance, value the  $\xi_{loc}$  of the robust estimator has a stronger dependence on the number of outliers rather than on their variance.

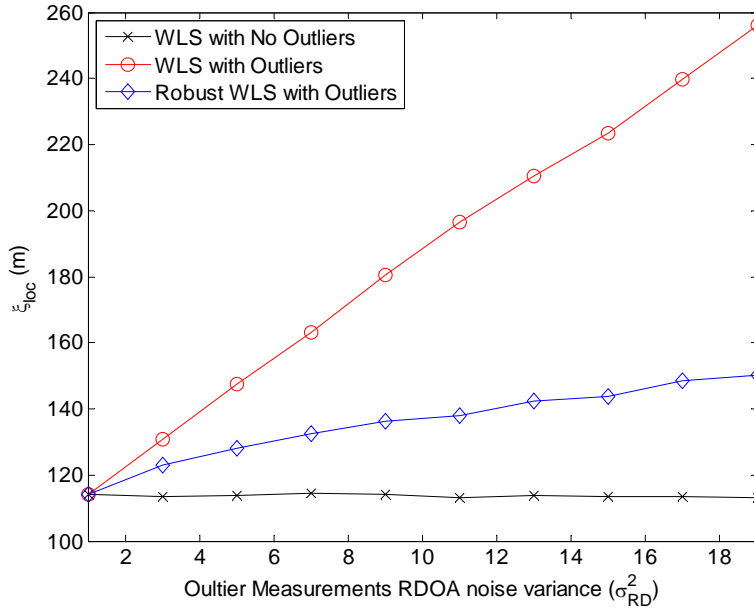


Figure 32. Root mean-square error  $\xi_{loc}$  of the weighted least-squares estimator with outliers (red), weighted least-squares estimator without outliers (black), and robust weighted least-squares estimator with outliers (blue) versus RDOA noise gain. Results based on 10,000 trials with  $N_s = 5$ ,  $r_a = 200$  m, and  $\omega_t = [2000 \text{ m}, 30 \text{ deg}]^T$ . In the outlier cases there were 2 random outliers present.

The performance of the robust weighted least-squares estimator compared to the regular weighted least-squares estimator as a function of the emitter's bearing is shown in Figure 33. In this simulation, there are two outlier measurements present with a variance

equal to five times  $\sigma_{RD}^2$ , the emitter is located at  $\omega_t = [2000 \text{ m}, \theta_t]^T$  where  $\theta_t$  ranges from  $-60 \leq \theta_t \leq 60$ ,  $r_a = 200 \text{ m}$ , and each data point is the result of 10,000 trials. From the results, we see the robust weighted least-squares estimator performs better than the regular estimator and at a wider range of  $\theta_t$ . This suggests that the robust estimator has a smaller dependence on the emitter's bearing compared to the regular weighted least-squares estimate. This also validates the effectiveness of the rejection processes in increasing the initial estimate's accuracy in the presence of measurement outliers. From Figure 23, we see that the refined estimator's performance is dependent on the initial estimator's performance; therefore, any improvement to the initial estimate's accuracy benefits the overall localization performance.

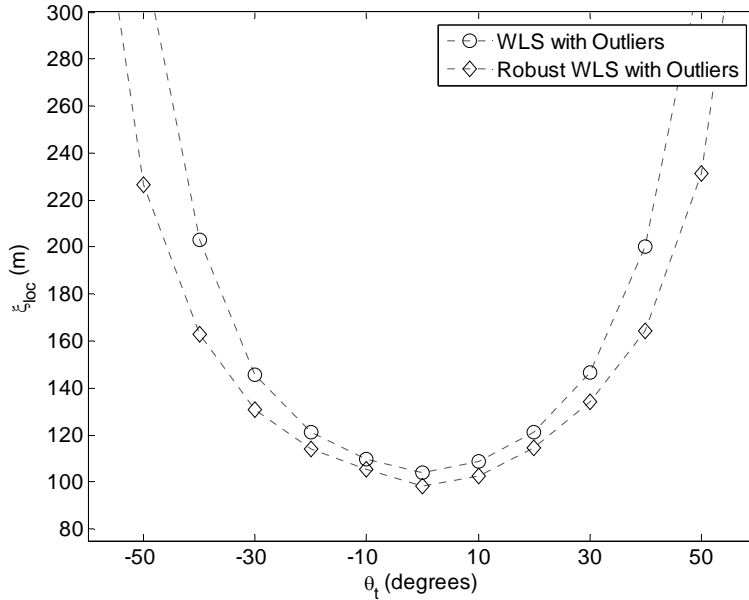


Figure 33. Root mean-square error  $\xi_{loc}$  of the weighted least-squares estimator (circle) and robust weighted least-squares estimator (diamond) versus  $\theta_t$ .

Results based on 3,000 trials with  $\sigma_{RD}^2 = 0 \text{ dB}$ ,  $N_s = 5$ ,  $r_a = 200 \text{ m}$ , and  $r_t = 2000 \text{ m}$ . In both cases there were 2 random outliers present at a RDOA noise variance five times  $\sigma_{RD}^2$ .

#### D. PERFORMANCE OF THE ROBUST LOCALIZATION IN THE PRESENCES OF MEASUREMENT OUTLIERS AND UNIFORM POSITION ERRORS

In this section, we examine at the performance of the proposed robust weighted least-squares localization in the presence of measurement outliers and uniform position errors. To assess the performance of the localization with position errors we evaluated two Monte Carlo simulations, with and without measurement outliers present. Each simulation uses a 15 node ASLA configured network in which the emitter is located at  $\omega_t = [2000 \text{ m}, 30 \text{ deg}]^T$ ,  $r_a = 200 \text{ m}$ ,  $\sigma_{RD}^2 = 0 \text{ dB}$ , and all data points are the result of 10,000 trials.

A comparison of the robust and regular weighted least-squares estimator's  $\xi_{loc}$  as a function of maximum uniform position error  $\delta_p$  is shown in Figure 34. In this case, there are no measurement outliers present. From the results, we see that the robust estimator does not improve performance over the regular estimator until a  $\delta_p$  value of 0.4 meters. Overall, this would suggest that the outlier rejection process is not beneficial in the small position error case given that there are no outliers present.

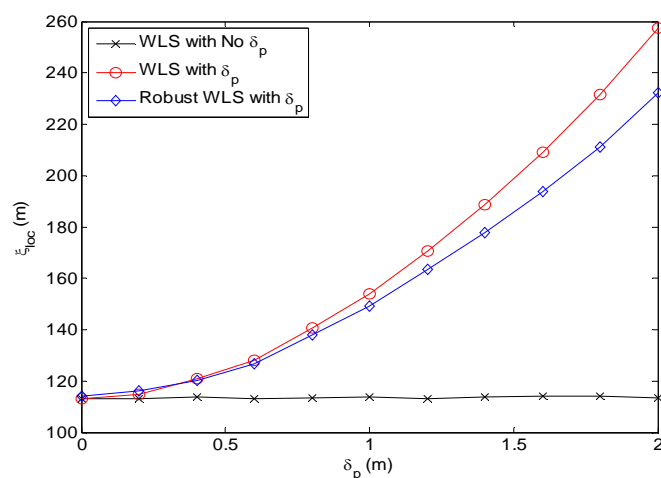


Figure 34. Root mean-square error  $\xi_{loc}$  of the weighted least-squares estimate (red) and robust weighted least-squares estimate (blue) versus  $\delta_p$ . For comparison the no error case is shown in black. Results based on 10,000 trials with  $\sigma_{RD}^2 = 0 \text{ dB}$ ,  $N_s = 5$ ,  $r_a = 200 \text{ m}$ , and  $\omega_t = [2000 \text{ m}, 30 \text{ deg}]^T$ .

Now, with measurement outliers present, a comparison of the robust and regular weighted least-squares estimator's  $\xi_{loc}$  is shown in Figure 35. In contrast to Figure 34, the robust estimator shows a semi-fixed amount improvement over the regular estimator at all values of position errors simulated. This result suggests that the robust estimator is effective against measurement outliers but only marginally effective in the presence of position errors.

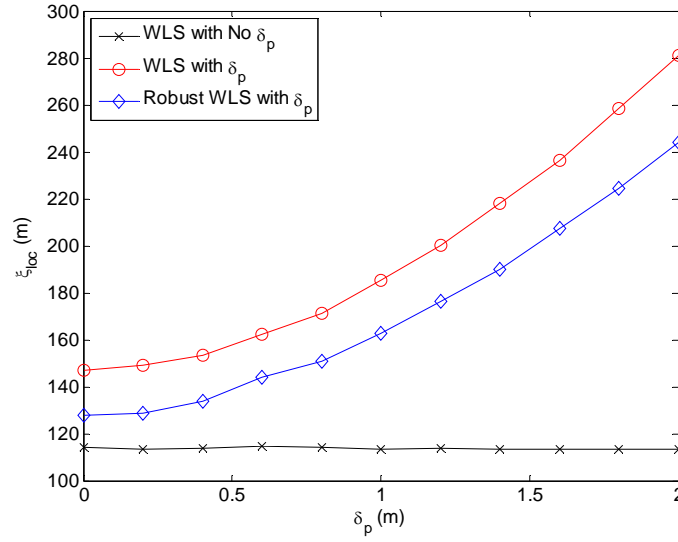


Figure 35. Root mean-square error  $\xi_{loc}$  of the weighted least-squares estimate (red) and robust weighted least-squares estimate (blue) versus  $\delta_p$ . For comparison the no error case is shown in black. Results based on 10,000 trials with  $\sigma_{RD}^2 = 0$  dB,  $N_s = 5$ ,  $r_a = 200$  m, and  $\omega_t = [2000 \text{ m}, 30 \text{ deg}]^T$ .

In this chapter, we developed a localization technique that is capable of approaching the CRLB. This technique consists of two sequential location estimators, a weighted least-squares estimator followed by a maximum-likelihood estimator to refine the initial estimate. We demonstrated that this technique is moderately susceptible to sensor position errors. Next, we developed a measurement outlier rejection process to compensate for these position errors as well as measurement outliers. The simulation results showed that the outlier rejection technique is effective against measurement

outliers and large position errors. In the next chapter, we provide a detailed description of the proposed collaborative signal collection technique.

## V. ROBUST SIGNAL COLLECTION FROM AN AIRBORNE SEMI-STATIONARY NETWORK

In this chapter, we develop the proposed collaborative signal collection scheme. This begins with an analysis of uniform and Gaussian sensor position errors and their effects on the ASLA formation's array factor and main beam gain. Through this analysis, we are able to derive a novel signal estimator that uses sampled data and knowledge of the position error statistics to compensate for the sensor position errors. We further improve the collection's robustness to interfering signals by adapting virtual filling and array tapering techniques to the proposed scheme. Simulations are used to support the developed theory and analyze its performance.

### A. EFFECTS OF UNIFORM POSITION ERROR ON THE ARRAY FACTOR

In Chapter IV, we showed that uniform position errors negatively affect the localization performance. In this section, we discuss the effects of these errors on collaborative beamforming.

From [63], we rewrite (28) to represent the array factor of a planar array as

$$A_{FP}(\theta_{sa}, \theta_t) = \sum_{i=1}^M w_i e^{j\alpha_i}, \quad (85)$$

where  $\theta_t$  is the signal bearing,  $\theta_{sa}$  is the array steering angle, i.e., the direction of the main beam gain,  $\alpha_i$  is the  $i^{\text{th}}$  node's signal phase expressed as

$$\alpha_i = \beta(x_i \sin \theta_t + y_i \cos \theta_t), \quad (86)$$

$w_i$  is the  $i^{\text{th}}$  node's complex weight expressed as

$$w_i = \exp(-j\beta(x_i \sin \theta_{sa} + y_i \cos \theta_{sa})), \quad (87)$$

$M$  is the number of sensor nodes, and  $\beta = 2\pi / \lambda$ . Incorporating uniform position errors  $\delta_x$  and  $\delta_y$  (see (53)) into (86) yields

$$\tilde{\alpha}_i = \beta \left( (x_i + \delta_{x,i}) \sin \theta_t + (y_i + \delta_{y,i}) \cos \theta_t \right). \quad (88)$$

Separating the sensor position from its position errors, we get

$$A_\varepsilon(\theta_{sa}, \theta_t, \delta_x, \delta_y) = \sum_{i=1}^M w_i \exp(j\alpha_i) \exp(j\alpha_{p,i}), \quad (89)$$

where

$$\alpha_{p,i} = \beta (\delta_{x,i} \sin \theta_t + \delta_{y,i} \cos \theta_t) \quad (90)$$

is the  $i^{\text{th}}$  node's phase perturbation due to position errors. To steer the array to the intended signal's direction  $\theta_t$ , we set  $\theta_{sa}$  equal to  $\theta_t$ . As a result,  $w_i \exp(j\alpha_i) = 1$ , and the array factor becomes the expression for the main beam gain

$$G_{MB}(\theta_t, \delta_x, \delta_y) = A_\varepsilon(\theta_{sa}, \theta_t, \delta_x, \delta_y) \Big|_{\theta_{sa} = \theta_t = \text{constant}} = \sum_{i=1}^M e^{j\beta(\delta_{x,i} \sin \theta_t + \delta_{y,i} \cos \theta_t)}, \quad (91)$$

where we assume that  $\theta_t$  is known and treat it as a constant. By letting

$\eta_{\varepsilon,i} = e^{j\beta(\delta_{x,i} \sin \theta_t + \delta_{y,i} \cos \theta_t)}$ , we can express the mean of the phase error per node as

$$\mu_{\eta_{\varepsilon,i}} = E\{\eta_{\varepsilon,i}\} = \int_{-\delta_p}^{\delta_p} \int_{-\delta_p}^{\delta_p} e^{j\beta(\delta_{x,i} \sin \theta_t + \delta_{y,i} \cos \theta_t)} f_{\Delta_x}(\delta_x) f_{\Delta_y}(\delta_y) d\delta_{x,i} d\delta_{y,i}. \quad (92)$$

By substituting  $f_{\Delta_x}(\delta_x) = f_{\Delta_y}(\delta_y) = 1/(2\delta_p)$  into (92), we obtain

$$\text{magnitude } \left\{ \mu_{\eta_{\varepsilon,i}} \right\} = \frac{\sin(\delta_p \beta \sin \theta_t) \sin(\delta_p \beta \cos \theta_t)}{(\delta_p \beta)^2 \sin \theta_t \cos \theta_t} \quad (93)$$

and

$$\text{angle } \left\{ \mu_{\eta_{\varepsilon,i}} \right\} = 0. \quad (94)$$

The variance of  $\eta_{\varepsilon,i}$  is then obtained from

$$\sigma_{\eta_{\varepsilon,i}}^2 = E\left\{ \eta_{\varepsilon,i}^2 \right\} - \mu_{\eta_{\varepsilon,i}}^2, \quad (95)$$

where the second moment  $E\left\{ \eta_{\varepsilon,i}^2 \right\}$  is expressed as

$$\begin{aligned} E\left\{ \eta_{\varepsilon,i}^2 \right\} &= \int_{-\delta_p}^{\delta_p} \int_{-\delta_p}^{\delta_p} \left| e^{j\beta(\delta_{x,i} \sin \theta_t + \delta_{y,i} \cos \theta_t)} \right|^2 f_{\Delta_x}(\delta_x) f_{\Delta_y}(\delta_y) d\delta_{x,i} d\delta_{y,i}, \\ &= \left( \frac{1}{2\delta_p} \right)^2 \int_{-\delta_p}^{\delta_p} \int_{-\delta_p}^{\delta_p} e^{j\beta(\delta_{x,i} \sin \theta_t + \delta_{y,i} \cos \theta_t)} e^{-j\beta(\delta_{x,i} \sin \theta_t + \delta_{y,i} \cos \theta_t)} d\delta_{x,i} d\delta_{y,i}, \\ &= \left( \frac{1}{2\delta_p} \right)^2 \int_{-\delta_p}^{\delta_p} \int_{-\delta_p}^{\delta_p} 1 d\delta_{x,i} d\delta_{y,i}, \\ &= 1. \end{aligned} \quad (96)$$

Using (96), we rewrite (95) as

$$\sigma_{\eta_{\varepsilon,i}}^2 = 1 - \mu_{\eta_{\varepsilon,i}}^2. \quad (97)$$

Assuming that  $\delta_{x,i}$  and  $\delta_{y,i}$  are independent and identically distributed random variables, we have that  $\eta_{\varepsilon,i}$  for  $i = 1, \dots, M$  are also independent and identically distributed. Given

that  $G_{MB}(\theta_t, \delta_x, \delta_y)$  is the sum of these  $M$  random variables, we express its mean and variance as

$$\mu_{G_{MB}} = \sum_{i=1}^M \mu_{\eta_{\epsilon,i}} = M \mu_{\eta_{\epsilon}} \quad (98)$$

and

$$\sigma_{G_{MB}}^2 = \sum_{i=1}^M \sigma_{\eta_{\epsilon,i}}^2 = M (1 - \mu_{\eta_{\epsilon}}^2). \quad (99)$$

### 1. Effects of Uniform Position Error in the Special Case when the ASLA Formation Is Normal to the Target Source

In the special case where the ASLA array has been reoriented (see Figure 18 (b)), the target emitter is normal to the array making  $\theta_t = \theta_{sa} = 0$  deg. In this scenario, the expressions for the mean of the main beam gain is simplified such that (91) is now only a function of  $\delta_y$  and is written as

$$\tilde{G}_{MB}(\delta_y) = \sum_{i=1}^M e^{j\beta\delta_{y,i}}. \quad (100)$$

By letting  $\tilde{\eta}_{\epsilon,i} = e^{j\beta\delta_{y,i}}$ , we can express the mean of the phase error per node as

$$\tilde{\mu}_{\eta_{\epsilon,i}} = E\{\tilde{\eta}_{\epsilon,i}\} = \int_{-\delta_p}^{\delta_p} e^{j\beta\delta_{y,i}} f_{\Delta_y}(\delta_y) d\delta_{y,i}. \quad (101)$$

By substituting  $f_{\Delta_y}(\delta_y) = 1/(2\delta_p)$  into (101), we obtain

$$\text{magnitude } \{\tilde{\mu}_{\eta_{\epsilon,i}}\} = \frac{\sin(\delta_p \beta)}{\delta_p \beta}. \quad (102)$$

$$\text{angle } \{\tilde{\mu}_{\eta_{\epsilon,i}}\} = 0. \quad (103)$$

Along the lines of (98) and (99), we express mean and variance of the main beam gain as

$$\tilde{\mu}_{G_{MB}} = \sum_{i=1}^M \tilde{\mu}_{\eta_{\varepsilon,i}} = M \tilde{\mu}_{\eta_{\varepsilon}} \quad (104)$$

and

$$\tilde{\sigma}_{G_{MB}}^2 = \sum_{i=1}^M \tilde{\sigma}_{\eta_{\varepsilon,i}}^2 = M (1 - \tilde{\mu}_{\eta_{\varepsilon}}^2). \quad (105)$$

## 2. Simulation Results on the Effects of Uniform Position Errors on the Array Factor

To support these findings, three simulations were conducted using an  $N_s = 5$  ASLA configured network with a total of  $M = 15$  nodes each with uniform position errors. For these simulations,  $\lambda = 1$ , the source emitter is located at a bearing of  $\theta_t = 45 \text{ deg}$ ,  $r_a = 200 \text{ m}$ , and all data points are the result of 1,000 trials.

A comparison between the simulated and theoretical values of  $\mu_{MB}$  and  $\sigma_{MB}^2$  as a function of  $\delta_p$  are shown in Figure 36 and Figure 37. From the results, we see that the simulated values closely adhere to the theoretical values, thus validating the derived expressions.

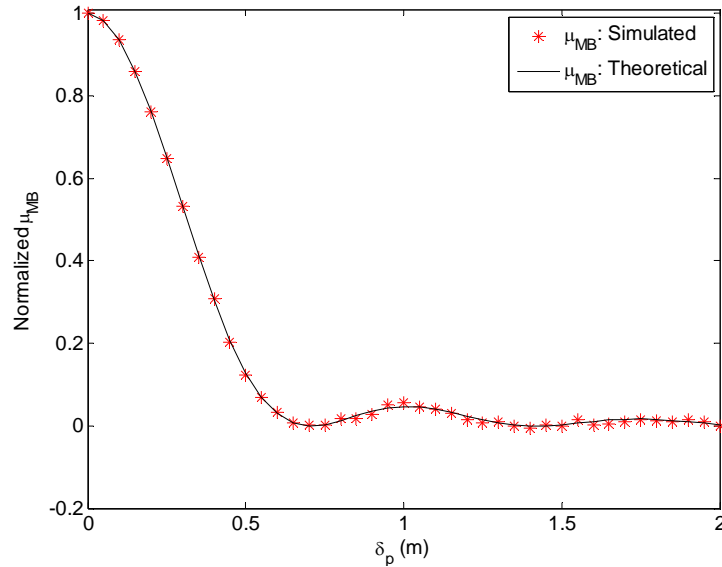


Figure 36. Mean normalized main beam gain of an  $N_s = 5$  ASLA versus  $\delta_p$ .  
Results based on 1,000 trials with  $r_a = 200 \text{ m}$ , and  $\theta_t = 45 \text{ deg}$ .

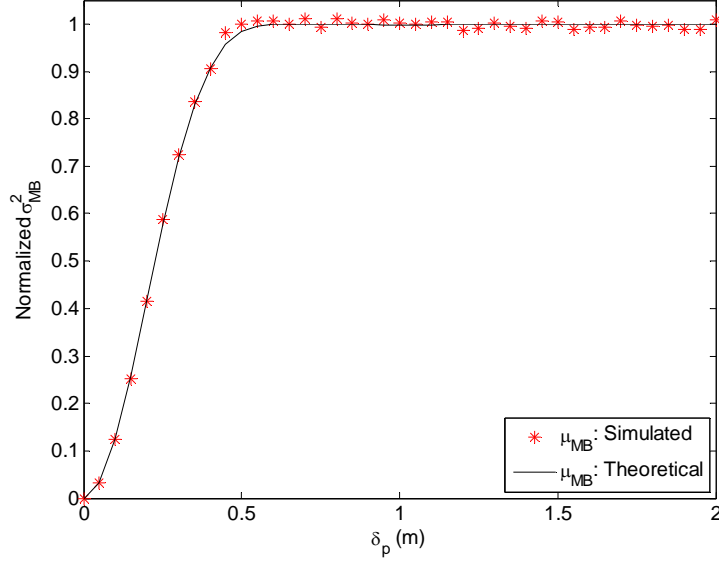


Figure 37. Variance of the normalized main beam gain for  $N_s = 5$  ASLA versus  $\delta_p$ . Results based on 1,000 trials with  $r_a = 200$  m, and  $\theta_t = 45$  deg.

We now evaluate the effects of uniform position errors on the array factor. The average normalized array factor error  $\psi_\varepsilon$  (refer to (61)) as a function of maximum uniform position error  $\delta_p$  is shown in Figure 38. In this simulation,  $N_s = 5$ , each data point is the result of 1,000 trials,  $\lambda = 1$ ,  $r_a = 200$  m, and  $\theta_t = 45$  deg. From the results, we can see that the average  $\psi_\varepsilon$  rapidly increases with  $\delta_p$ , which means that even minor position ( $\delta_p < 1$  m) errors can have a significant effect on the array factor. This suggests that position errors of this nature if not compensated for will negate any benefits that collaborative beamforming can provide. This result is a key motivator for this research, as it is the objective of this dissertation to deliver an effective signal collection scheme (see Chapter V section C) in the presence of such errors.

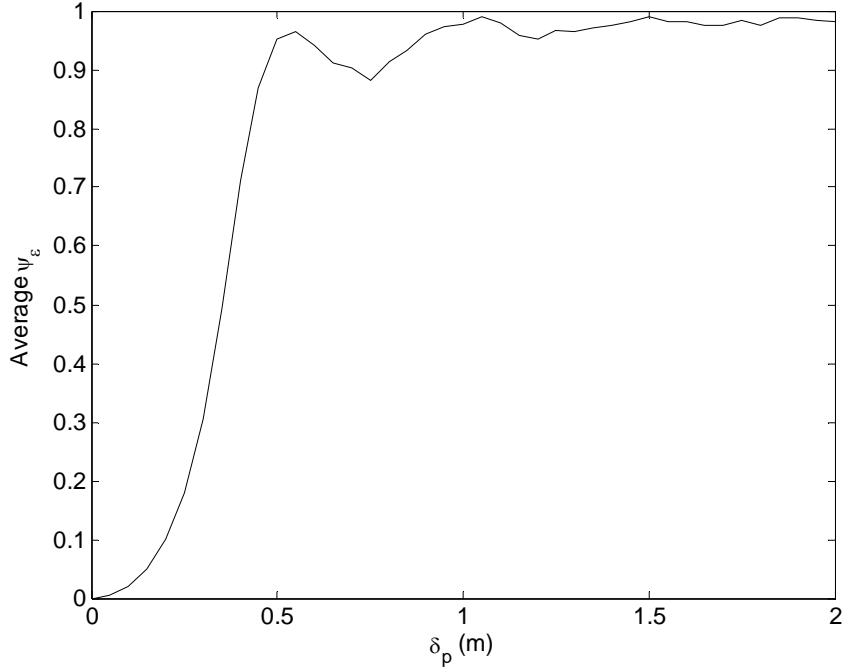


Figure 38. Average  $\psi_\varepsilon$  for an  $N_s = 5$  ASLA versus  $\delta_p$ . Results based on 1,000 trials with  $\lambda = 1$ ,  $r_a = 200$  m, and  $\theta_t = 45$  deg.

## B. EFFECTS OF GAUSSIAN POSITION ERROR ON THE ARRAY FACTOR

In the previous section, we evaluated the effects of uniform position error on the array factor and the main beam gain of an ASLA configuration. In this section, we perform a similar analysis with Gaussian position errors.

Similar to the uniform position error case, we wish to obtain an expression for the mean and variance of the main beam gain; however, using the same methodology becomes intractable for the Gaussian random variables. As an alternative, we instead evaluate the main beam gain after the ASLA formation has been reoriented as shown in Figure 18 (b). In this configuration, we assume that  $\theta_t = \theta_{sa} = 0$  deg. This assumption allows us to study the effects of Gaussian position errors independent of errors in the bearing estimate  $\hat{\theta}_t$ . As a result of this assumption, the main beam gain from (91) can be expressed as

$$G_{MB}(\delta_y) = \sum_{i=1}^M e^{j\beta\delta_y}, \quad (106)$$

where  $e^{j\beta\delta_y}$  is known as the wrapped Gaussian random variable [84]. By letting  $w_{g,i} = e^{j\beta\delta_{y,i}}$ , we can interpret the main beam gain as the sum of  $M$  wrapped Gaussian random variables  $w_g$ , each with a mean of zero and variance  $\sigma_g^2 = (\beta\sigma_p)^2$  [84]. The probability density function of the wrapped Gaussian random variable is given by [84]

$$f_{w_g}(w_g, \sigma_g^2) = \frac{1}{\sqrt{2\pi\sigma_g^2}} \sum_{k=-\infty}^{\infty} \exp\left(-\frac{(w_g + 2\pi k)^2}{2\sigma_g^2}\right). \quad (107)$$

The mean values of the magnitude and phase, respectively, are given by [84]

$$\text{magnitude}\{\mu_w\} = e^{-(\beta\sigma_p)^2/2} \quad (108)$$

$$\text{angle}\{\mu_w\} = 0. \quad (109)$$

The variance is given as

$$\sigma_w^2 = 1 - e^{-(\beta\sigma_p)^2/2}. \quad (110)$$

Since the main beam gain is the sum of  $M$  terms, similar to (98) and (99) we express the mean value of its magnitude and phase as

$$\text{magnitude}\{\mu_{MB}\} = M e^{-(\beta\sigma_p)^2/2}, \quad (111)$$

$$\text{angle}\{\mu_{MB}\} = 0 \quad (112)$$

with a corresponding variance of

$$\sigma_{MB}^2 = M \left(1 - e^{-(\beta\sigma_p)^2/2}\right). \quad (113)$$

## 1. Simulation Results of the Effects of Gaussian Position Errors on the Array Factor

To support the theory presented in the previous section, three simulations were conducted using an  $N_s = 30$  ASLA configured network, with Gaussian position errors. In these simulations, the source emitter is located at a bearing of  $\theta_t = 0^\circ$ ,  $\lambda = 1$ ,  $r_a = 200$  m, and all data points are the result of 1,000 trials.

A plot of the simulation and theoretical normalized values of magnitude  $\{\mu_{MB}\}$  as a function of  $\sigma_g^2 = (\beta\sigma_p)^2$  is shown in Figure 39. From the plot, we see that the simulation results closely follow the theoretical. The results indicate that the main beam gain monotonically decreases as  $\sigma_g^2$  increases. Similar to the uniform position error case, we see that the errors significantly reduce the effectiveness of collaborative beamforming.

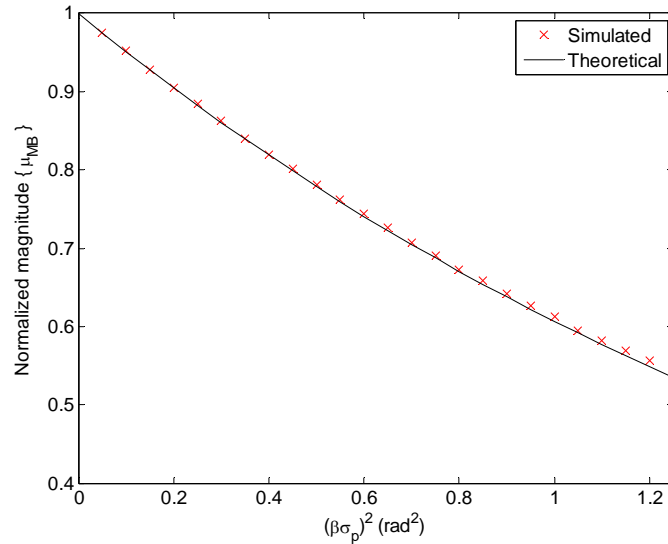


Figure 39. Normalized values of magnitude  $\{\mu_{MB}\}$  versus position error variance

$\sigma_g^2 = (\beta\sigma_p)^2$ . In this simulation  $N_s = 30$ ,  $\theta_t = 0^\circ$ ,  $\lambda = 1$ ,  $r_a = 200$  m, and all data points are the result of 1,000 trials.

Similar to the previous simulation, a comparison between the simulation and theoretical values of  $\text{angle}\{\mu_{MB}\}$  as a function of  $\sigma_g^2 = (\beta\sigma_p)^2$  is shown in Figure 40. From the results, we see that the simulation results closely follow the theoretical value, with the  $\text{angle}\{\mu_{MB}\}$  values approximately equal to zero at all values of  $\sigma_g^2$  simulated. This suggests that the effects of Gaussian position errors have no effect on the mean value of the main beam phase angle. Since position errors do not affect the  $\text{angle}\{\mu_{MB}\}$ , it will have a prominent role in the signal estimation described in the following section.

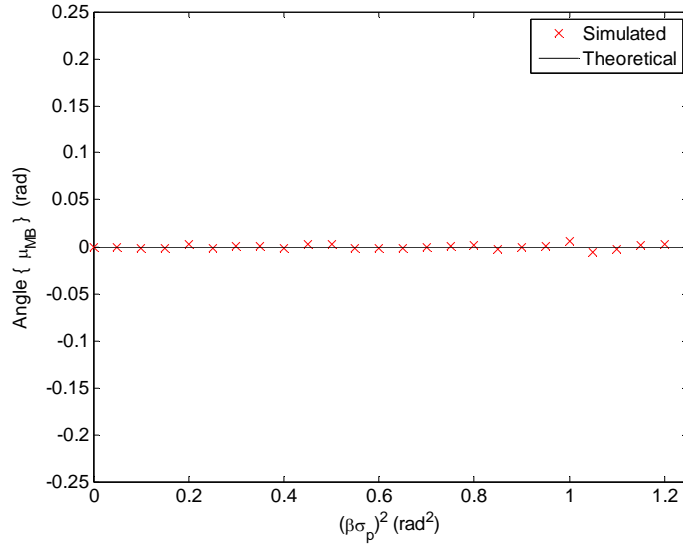


Figure 40. Values of  $\text{angle}\{\mu_{MB}\}$  versus position error variance  $\sigma_g^2 = (\beta\sigma_p)^2$ . In this simulation  $N_s = 30$ ,  $\theta_t = 0^\circ$ ,  $\lambda = 1$ ,  $r_a = 200$  m, and all data points are the result of 1,000 trials.

### C. SIGNAL COLLECTION FROM AIRBORNE SYMMETRIC LINE ARRAY NETWORK IN THE PRESENCE OF UNIFORM POSITION ERRORS

In the previous section, we showed that each node's phase perturbations due to position errors have a mean value of zero. Given that the ASLA configuration contains three stacks of  $N_s$  sensor nodes each, we consider a snapshot of the complex signal received by each node in a particular stack, which we model as the true signal received at

that stack with phase perturbations due to position errors. By using the mean value of the in-phase and quadrature components of all the measurements from a particular stack, we can estimate the true signal magnitude and phase at that stack. Since position errors do not affect the mean value of the phase estimate, this method will recover the signal magnitude and phase despite the presence of position errors. Given this, we derive an expression for the mean of the in-phase and quadrature components at each stack. This expression is used to estimate the phase and magnitude based on the sample mean of the received complex snapshots.

Considering an ASLA configured network with uniform position errors, we represent a snapshot of the complex signal received at the  $i^{\text{th}}$  node of the center stack as

$$\gamma_{c,i} = V_t e^{j\phi_t} e^{j\beta(\delta_{x,i}\sin\theta_t + \delta_{y,i}\cos\theta_t)}, \quad (114)$$

where  $i = 1, \dots, N_s$ , and  $V_t$  and  $\phi_t$  are the signal's magnitude and phase, respectively.

Using the same assumptions used to derive (106), we express (114) as

$$\gamma_{c,i} = V_t e^{j(\phi_t + \rho_{\varepsilon,i})} \quad (115)$$

where  $\rho_{\varepsilon,i} = \beta\delta_{y,i}$  is a uniform random variable representing the  $i^{\text{th}}$  node's phase perturbation due to position errors in the y-direction. The resulting complex signal is then represented as two random variables [85]

$$\gamma_{c,i} = \gamma_{c_I,i} + j\gamma_{c_Q,i}, \quad (116)$$

where  $\gamma_{c_I,i}$  is the  $i^{\text{th}}$  node's in-phase component expressed as

$$\gamma_{c_I,i} = V_t \cos(\phi_t + \rho_{\varepsilon,i}) \quad (117)$$

and  $\gamma_{c_Q,i}$  is the  $i^{\text{th}}$  node's quadrature component expressed as

$$\gamma_{c_Q,i} = V_t \sin(\phi_t + \rho_{\varepsilon,i}). \quad (118)$$

We consider  $\gamma_{c_I}$  and  $\gamma_{c_Q}$  as two random variables representing a given stack's received in-phase and quadrature components, respectively. The random variables  $\gamma_{c_I,i}$  and  $\gamma_{c_Q,i}$  can be interpreted as the  $i^{\text{th}}$  instance of the true  $\gamma_{c_I}$  and  $\gamma_{c_Q}$  that are perturbed by node position errors. Also, the mean values of all the instances would then be the sample means of  $\gamma_{c_I}$  and  $\gamma_{c_Q}$ . Since we have shown that position errors do not affect the mean value of the signal phase, we can use the sample mean of  $\gamma_{c_I}$  and  $\gamma_{c_Q}$  to derive an estimate of the true signal phase. Overall, by deriving an expression for the mean of  $\gamma_{c_I}$  and  $\gamma_{c_Q}$ , we can also determine a way to estimate the true signal phase.

With a goal of derive an expression for the mean of  $\gamma_{c_Q}$  and  $\gamma_{c_I}$  for a given stack, we begin by deriving the probability density function of  $\gamma_{c_Q}$ . By substituting  $\rho_s = \phi_t + \rho_\varepsilon$  in (116), we get

$$\gamma_{c_Q} = V_t \sin(\rho_s). \quad (119)$$

The probability density function of  $\rho_s$  can be expressed as

$$f_{\Theta_s}(\rho_s) = \frac{1}{2\beta\delta_p}, \quad \phi_t - \beta\delta_p \leq \rho_s \leq \phi_t + \beta\delta_p. \quad (120)$$

We next substitute  $\kappa_s = \sin(\rho_s)$  in (119) to get

$$\gamma_{c_Q} = V_t \kappa_s. \quad (121)$$

The probability density function of the random variable  $\kappa_s$  is expressed as

$$f_{\kappa_s}(\kappa_s) = \frac{1}{|d\kappa_s/d\rho_s|} f_{\Theta_s}(\rho_s) \Big|_{\rho_s=g^{-1}(\kappa_s)} = \frac{1/(2\beta\delta_p)}{\sqrt{1-(\kappa_s)^2}}, \quad (122)$$

where

$$g^{-1}(\kappa_s) = \sin^{-1} \kappa_s, \quad (123)$$

and

$$|d\kappa_s/d\rho_s|_{\rho_s=g^{-1}(\kappa_s)} = \cos(\sin^{-1} \kappa_s) = \sqrt{1-(\kappa_s)^2}, \quad (124)$$

for  $\sin(\phi_t - \beta\delta_p) \leq \kappa_s \leq \sin(\phi_t + \beta\delta_p)$ . Finally, the probability density function of the random variable  $\gamma_{C_{Q_i}} = V_t \kappa_s$  is expressed as

$$\begin{aligned} f_{\Gamma_Q}(\gamma_{C_Q}) &= \frac{1}{V_t} f_{\kappa_s}\left(\frac{\gamma_{C_Q}}{V_t}\right) \\ &= \frac{1}{2\beta\delta_p} \frac{1}{\sqrt{V_t^2 - \gamma_{C_Q}^2}}, \quad V_t \sin(\phi_t - \beta\delta_p) \leq \gamma_{C_Q} \leq V_t \sin(\phi_t + \beta\delta_p). \end{aligned} \quad (125)$$

We then account for measurement noise using the expression

$$I_s = \gamma_{C_I} + I_{AWGN}, \quad (126)$$

and

$$Q_s = \gamma_{C_Q} + Q_{AWGN}, \quad (127)$$

where  $I_{AWGN}$  and  $Q_{AWGN}$  are independent Gaussian random variables, representing the complex additive white Gaussian noise. Using these expressions, we derive an estimate of  $V_t$  and  $\phi_t$  from the mean of all the center stack's complex in-phase and quadrature

measurements. The mean of each stack's in-phase and quadrature components can be expressed as

$$\mu_{C_I} = E\{I_s\} = E\{\gamma_{C_I}\} + E\{I_{AWGN}\}, \quad (128)$$

$$\mu_{C_Q} = E\{Q_s\} = E\{\gamma_{C_Q}\} + E\{Q_{AWGN}\}. \quad (129)$$

With regard to the quadrature component, since  $Q_{AWGN}$  is zero mean,  $\mu_{C_Q}$  can be re-written as

$$\mu_{C_Q} = E\{\gamma_{C_Q}\} = \begin{cases} \int_{A_Q}^{B_Q} \frac{1}{2\alpha_p} \frac{\gamma_{C_Q}}{\sqrt{V_t^2 - \gamma_{C_Q}^2}} d\gamma_{C_Q}, & |\phi_t| \leq \frac{\pi}{2} - \alpha_p \\ \int_{A_Q}^{B_Q} \frac{1}{2\alpha_p} \frac{\gamma_{C_Q}}{\sqrt{V_t^2 - \gamma_{C_Q}^2}} d\gamma_{C_Q} + \int_{A_Q}^{V_s} \frac{1}{2\alpha_p} \frac{\gamma_{C_Q}}{\sqrt{V_t^2 - \gamma_{C_Q}^2}} d\gamma_{C_Q}, & \frac{\pi}{2} - \alpha_p < |\phi_t| \leq \frac{\pi}{2} + \alpha_p \\ \int_{A_Q}^{B_Q} \frac{1}{2\alpha_p} \frac{\gamma_{C_Q}}{\sqrt{V_t^2 - \gamma_{C_Q}^2}} d\gamma_{C_Q}, & |\phi_t| > \frac{\pi}{2} + \alpha_p \end{cases}, \quad (130)$$

where  $\alpha_p = \beta\delta_p$ ,  $A_Q = V_t \sin(\phi_t - \alpha_p)$ , and  $B_Q = V_t \sin(\phi_t + \alpha_p)$ . We define the mean of the in-phase component similarly as

$$\begin{aligned}
\mu_{C_I} &= E\{\gamma_{C_I}\} \\
&= \begin{cases} \int_{A_I}^{B_I} \frac{1}{2\alpha_p} \frac{\gamma_{C_I}}{\sqrt{V_t^2 - \gamma_{C_I}^2}} d\gamma_{C_I}, & |\phi_t| \leq \frac{\pi}{2} - \alpha_p \\ \int_{A_I}^{B_I} \frac{1}{2\alpha_p} \frac{\gamma_{C_I}}{\sqrt{V_t^2 - \gamma_{C_I}^2}} d\gamma_{C_I} + \int_{A_I}^{V_t} \frac{1}{2\alpha_p} \frac{\gamma_{C_I}}{\sqrt{V_t^2 - \gamma_{C_I}^2}} d\gamma_{C_I}, & \frac{\pi}{2} - \alpha_p < |\phi_t| \leq \frac{\pi}{2} + \alpha_p \\ \int_{A_I}^{B_I} \frac{1}{2\alpha_p} \frac{\gamma_{C_I}}{\sqrt{V_t^2 - \gamma_{C_I}^2}} d\gamma_{C_I}, & |\phi_t| > \frac{\pi}{2} + \alpha_p \end{cases} \quad (131)
\end{aligned}$$

where  $A_I = V_t \cos(\phi_t - \alpha_p)$  and  $B_I = V_t \cos(\phi_t + \alpha_p)$ . By solving (130) for  $\phi_t$ , we obtain an expression for the true signal phase that is a function of  $\mu_{C_Q}$ ,  $V_t$  and  $\alpha_p$ . Then using the sample mean  $\hat{\mu}_{C_Q}$  in place of the true mean  $\mu_{C_Q}$ , we obtain the phase estimate  $\hat{\phi}_t$ . The derivation of the phase estimate  $\hat{\phi}_t$  for the case of  $|\phi_t| \leq \pi/2 - \alpha_p$  is shown as

$$\begin{aligned}
\hat{\mu}_{C_Q} &= \int_{A_Q}^{B_Q} \frac{1}{2\alpha_p} \frac{\gamma_{C_Q}}{\sqrt{V_t^2 - (\gamma_{C_Q})^2}} d\gamma_{C_Q}, \\
&= \frac{1}{2\alpha_p} \left[ \sqrt{V_t^2 - (\gamma_{C_Q})^2} \right]_{A_Q}^{B_Q}, \\
&= \frac{1}{2\alpha_p} \left[ \sqrt{V_t^2 - (A_Q)^2} - \sqrt{V_t^2 - (B_Q)^2} \right]. \quad (132)
\end{aligned}$$

By squaring both sides and expanding  $A_Q$  and  $B_Q$  terms, we get

$$\left(2\alpha_p \hat{\mu}_{C_Q}\right)^2 = \left( \sqrt{V_t^2 - \left(V_t \sin(\phi_t - \alpha_p)\right)^2} - \sqrt{V_t^2 - \left(V_t \sin(\phi_t + \alpha_p)\right)^2} \right)^2. \quad (133)$$

Expanding the right hand side and applying the trigonometric identity  $\cos^2 \theta - \sin^2 \theta = \cos 2\theta$ , we get

$$\begin{aligned} \left(2\alpha_p \hat{\mu}_{C_Q}\right)^2 = & V_t^2 \left(1 + \cos(2\phi_t) \cos(2\alpha_p)\right) \\ & - 2\sqrt{V_t^4 \cos^2(\phi_t - \alpha_p) \cos^2(\phi_t + \alpha_p)}. \end{aligned} \quad (134)$$

By taking  $V_t^4$  out of the square root and bringing  $V_t^2$  to the left hand side, we get

$$\begin{aligned} \left(2\alpha_p \hat{\mu}_{C_Q}\right)^2 = & V_t^2 \left(1 + \cos(2\phi_t) \cos(2\alpha_p)\right) \\ & - 2V_t^2 \left| \cos(\phi_t - \alpha_p) \cos(\phi_t + \alpha_p) \right| \end{aligned} \quad (135)$$

By applying trigonometric identity  $\cos x \cos y = (1/2)[\cos(x+y) + \cos(x-y)]$  to the absolute value terms, we get

$$\left( \frac{2\alpha_p \hat{\mu}_{C_Q}}{V_t} \right)^2 = 1 + \cos(2\phi_t) \cos(2\alpha_p) - \left| \cos(2\alpha_p) + \cos(2\phi_t) \right|. \quad (136)$$

We perform the same derivation for the mean of the in-phase component to obtain

$$\left( \frac{2\alpha_p \hat{\mu}_{C_I}}{V_t} \right)^2 = 1 - \cos(2\phi_t) \cos(2\alpha_p) - \left| \cos(2\alpha_p) - \cos(2\phi_t) \right|. \quad (137)$$

Taking the ratio of (136) and (137) yields

$$\left( \frac{\hat{\mu}_{C_Q}}{\hat{\mu}_{C_I}} \right)^2 = \frac{1 + \cos(2\phi_t) \cos(2\alpha_p) - \left| \cos(2\alpha_p) + \cos(2\phi_t) \right|}{1 - \cos(2\phi_t) \cos(2\alpha_p) - \left| \cos(2\alpha_p) - \cos(2\phi_t) \right|}. \quad (138)$$

To solve for  $\phi_t$ , we substitute,  $\mu_s = (\hat{\mu}_{C_q} / \hat{\mu}_{C_l})^2$ ,  $a = \cos(2\alpha_p)$  and  $b = \cos(2\phi_t)$  in (138) to get

$$\mu_s = \frac{1 + ab - |a + b|}{1 - ab - |a - b|} \quad (139)$$

By taking only the positive solutions for the absolute value terms and solving for  $b$ , we get

$$b = \frac{1 - \mu_s}{1 + \mu_s}. \quad (140)$$

Since  $b = \cos(2\phi_t)$ , we can solve (140) for the phase estimate

$$\hat{\phi}_t = (1/2) \cos^{-1} \left( \frac{1 - \mu_s}{1 + \mu_s} \right). \quad (141)$$

For the other two cases of (130), repeating the above steps yields the same expression for the phase estimate  $\hat{\phi}_t$ . By substituting  $\hat{\phi}_t$  into (137) and solving for  $V_t$ , we get the signal magnitude estimate

$$\hat{V}_t = \begin{cases} \frac{2\alpha_p \hat{\mu}_{C_l}}{\sqrt{1 - \cos(2\hat{\phi}_t) \cos(2\alpha_p) - |\cos(2\hat{\phi}_t) - \cos(2\alpha_p)|}}, & |\hat{\phi}_t| \leq \frac{\pi}{2} - \alpha_p \\ \frac{2\alpha_p \hat{\mu}_{C_l}}{|\cos(\hat{\phi}_t - \alpha_p)| + |\cos(\hat{\phi}_t + \alpha_p)|}, & \frac{\pi}{2} - \alpha_p < |\hat{\phi}_t| \leq \frac{\pi}{2} + \alpha_p \\ \frac{2\alpha_p \hat{\mu}_{C_l}}{\sqrt{1 - \cos(2\hat{\phi}_t) \cos(2\alpha_p) - |\cos(2\hat{\phi}_t) - \cos(2\alpha_p)|}}, & |\hat{\phi}_t| > \frac{\pi}{2} + \alpha_p. \end{cases} \quad (142)$$

With each stack in the array using the same estimation technique, we express their complex signal estimates as

$$\hat{\Omega}_n = \hat{V}_{t,n} \exp(j\hat{\phi}_{t,n}), \quad n = 1, 2, 3, \quad (143)$$

where  $\hat{V}_{t,n}$  and  $\hat{\phi}_{t,n}$  are the left, right and center stack's magnitude and phase estimates, respectively. Each stack's  $\hat{\Omega}_n$  is then treated as the complex output of a single node in a phase shift beamforming array. The final main beam response is then expressed as

$$\hat{\Omega}_t = \sum_{n=1}^3 \hat{\Omega}_n. \quad (144)$$

### 1. Signal Collection in the Presence of Thermal Noise and Uniform Sensor Position Error

To demonstrate the performance of our signal collection and estimation scheme, we present the results of five Monte Carlo simulations in Figure 41 through Figure 45. The results of these simulations focus on the root mean-square error for signal magnitude ( $\xi_v$ ) and phase ( $\xi_\phi$ ) estimate. For all five simulations,  $\lambda = 1$  m, the source emitter is located at  $\omega_t = [2000 \text{ m}, 45 \text{ deg}]^T$ ,  $r_a = 200$  meters, and all data points are the result of 10,000 trials. Note a key parameter in the following simulations is signal to noise ratio (SNR) in units of dB. This quantity is a measure of the ratio between signal power  $P_r$  and noise power  $P_n$  and is expressed as  $\text{SNR} = 10 \log_{10}(P_r / P_n)$ .

A comparison of the scheme's  $\xi_v$  and  $\xi_\phi$  as a function of per node SNR at different RDOA noise variance  $\sigma_{RD}^2$  levels are shown in Figure 41 and Figure 42, respectively. The target bearing estimate  $\hat{\theta}_t$  is derived using (75). From the results, we see that the effect of the per-node SNR on  $\xi_v$  and  $\xi_\phi$  is not as strong as that of the  $\hat{\theta}_t$  estimate. This suggests that the estimator is heavily dependent on the accuracy of the localization.

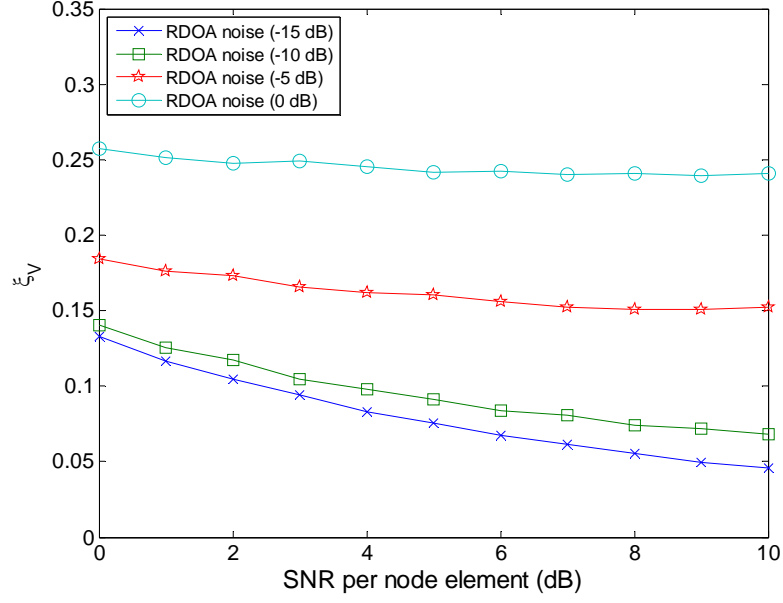


Figure 41. Root mean-square error  $\xi_v$  at different levels of RDOA noise versus SNR per node. Results based on 10,000 trials with  $N_s = 10$ ,  $r_a = 200$  m,  $\delta_p = .05$  m, and  $\omega_l = [2000 \text{ m}, 45 \text{ deg}]^T$ .

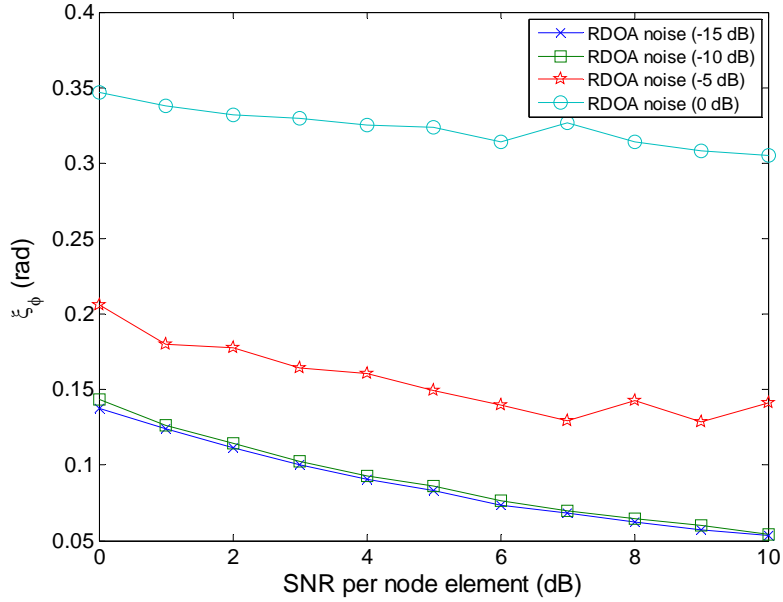


Figure 42. Root mean-square error  $\xi_\phi$  at different levels of RDOA noise versus SNR per node. Results based on 10,000 trials with  $N_s = 10$ ,  $r_a = 200$  m,  $\delta_p = .05$  m, and  $\omega_l = [2000 \text{ m}, 45 \text{ deg}]^T$ .

Two plots comparing the scheme's  $\xi_\phi$  as a function of maximum uniform position error  $\delta_p$  and the number of nodes per stack  $N_s$  as a function of  $\sigma_{RD}^2$  are shown in Figure 43 and Figure 44, respectively. In Figure 43, we see that uniform position error doesn't affect  $\xi_\phi$  until values of  $\delta_p > 0.1$  m in the low  $\sigma_{RD}^2$  case ( $\sigma_{RD}^2 = -10$  dB). Conversely, it causes a near linear increase in  $\xi_\phi$  for all values of  $\delta_p$  simulated. In Figure 44, the results show that the benefits of increasing  $N_s$  diminishes when  $N_s > 10$  nodes. Unlike the results from Figure 21, where increasing the number of nodes improved performance, here increasing the number of nodes per stack is less effective above a certain value.

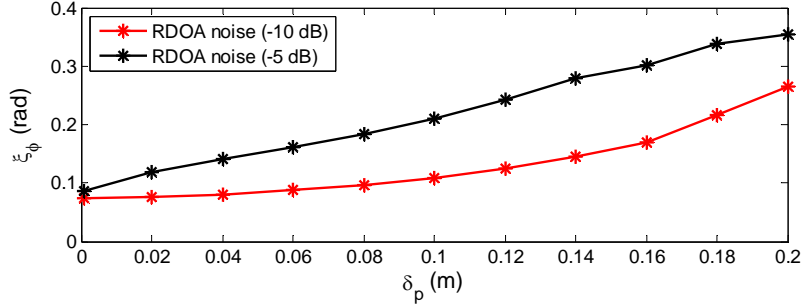


Figure 43. Root mean-square error  $\xi_\phi$  at different levels of RDOA noise under increase maxed uniform position error  $\delta_p$ . Results based on 10,000 trials with,  $N_s = 10$ ,  $r_a = 200$  m, SNR = 5 dB, and  $\omega_l = [2000 \text{ m}, 45 \text{ deg}]^T$ .

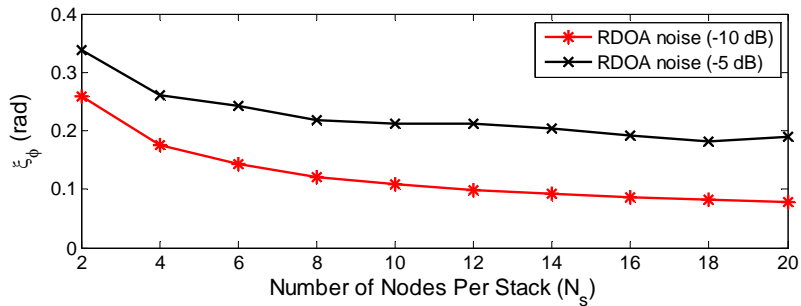


Figure 44. Root mean-square error  $\xi_\phi$  at different levels of RDOA noise under increase maxed uniform position error  $N_s$ . Results based on 10,000 trials with,  $\delta_p = 1/10$  m,  $r_a = 200$  m, SNR = 5 dB, and  $\omega_l = [2000 \text{ m}, 45 \text{ deg}]^T$ .

A plot of the proposed scheme's  $\xi_v$  as a function of per node SNR with and without signal estimation is shown in Figure 45. Each case was also evaluated at two different values of  $\sigma_{RD}^2$ . The “with estimation” case represents our proposed scheme, i.e., collaborative beamforming in conjunction with the proposed signal estimator. The “no-estimation” case represents collaborative beamforming without the use of signal estimation. In this simulation, the source emitter is located at  $\omega_t = [2000 \text{ m}, 45 \text{ deg}]^T$ ,  $N_s = 10$ ,  $\lambda = 1 \text{ m}$ ,  $\delta_p = 1/10 \text{ m}$ , and all data points are the result of 10,000 trials. In the  $\sigma_{RD}^2 = -15 \text{ dB}$  case, we see that the benefits of the signal estimation are evident at all values of SNR simulated. As evident in the  $\sigma_{RD}^2 = -5 \text{ dB}$  case where the scheme underperforms the no-estimation case, we again see that the scheme is highly dependent on the accuracy of the localization phase. This dependency is derived from the scheme's assumption that the target signal's bearing is perfectly normal to the array, i.e., the  $\theta_t = 0 \text{ deg}$ , when in actuality  $\theta_t$  is a small random quantity based on the accuracy of the localization.

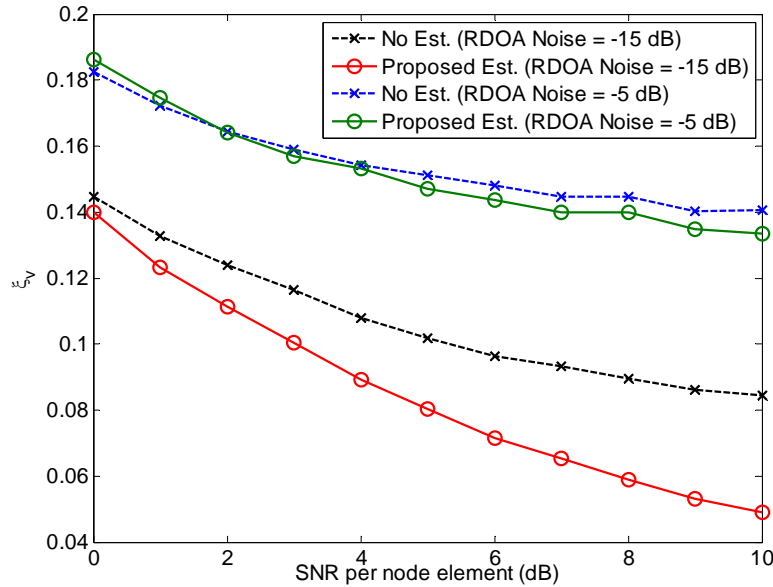


Figure 45. Signal  $\xi_v$  of proposed scheme compared with the no-estimation case versus SNR per node values. Results based on 10,000 trials with  $\delta_p = 1/10 \text{ m}$ ,  $r_a = 200 \text{ m}$ , and  $\omega_t = [2000 \text{ m}, 45 \text{ deg}]^T$ .

An illustration of the mean value of the normalized gain of the array as a function of signal frequency for different values of  $\delta_p$  is shown in Figure 46. For comparison, we also include the no-estimation case. In this simulation, the source emitter is located at  $\omega_t = [2000 \text{ m}, 45 \text{ deg}]^T$ ,  $N_s = 10$ ,  $\lambda = 1 \text{ m}$ ,  $\delta_p = 1/10 \text{ m}$ ,  $\sigma_{RD}^2 = 0 \text{ dB}$ , and all data points are the result of 10,000 trials. As frequency increases, so does  $\beta$ . From (115), we see that phase error due to  $\delta_p$  is proportional to  $\beta$ . As  $\beta = 2\pi f_c / c$ , an increase in frequency will magnify the negative effects of the position errors. From the results, we see that allowing these position errors into beamforming (no-estimation case) results in a response similar to that in Figure 36 where the main beam gain is significantly reduced as position errors increased. When we incorporate the proposed signal estimator, an improvement over the no-estimation case is apparent for all simulated frequency values. This suggests that the inclusion of signal estimation in collaborative beamforming can effectively mitigate array phase perturbations due to the uniformly distributed position errors.

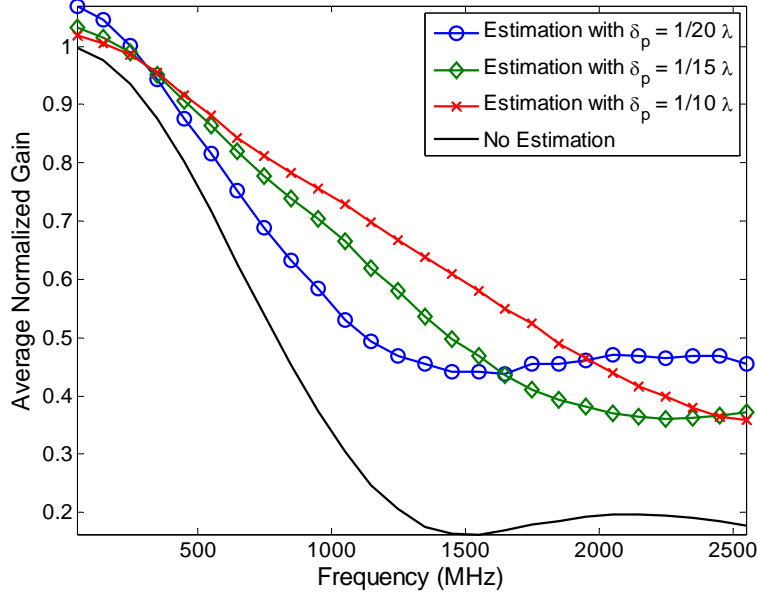


Figure 46. Average signal normalized gain at different levels of RDOA noise versus signal frequencies. Results based on 10,000 trials with  $\sigma_{RD}^2 = 0 \text{ dB}$ ,  $\delta_p = 1/10 \text{ m}$ ,  $r_a = 200 \text{ m}$ , and  $\omega_t = [2000 \text{ m}, 45 \text{ deg}]^T$ .

#### D. SIGNAL COLLECTION FROM AIRBORNE SYMMETRIC LINE ARRAY NETWORK IN THE PRESENCE OF GAUSSIAN POSITION ERROR

In the previous section, we developed a signal estimator to combat the effects of uniformly distributed position errors. In this section, we derive a similar estimator for the case of Gaussian distributed position errors.

In a fashion similar to (116), a snapshot of the complex signal received at the  $i^{\text{th}}$  node of the center stack is represented as

$$n_{C,i} = n_{C_I,i} + n_{C_Q,i}, \quad (145)$$

where

$$n_{C_I,i} = V_i \cos(\phi_i + \rho_n), \quad (146)$$

with  $\rho_n = \beta \delta_y$  with  $\delta_y$  being zero mean Gaussian position error with a variance of  $\sigma_p^2$  (see Chapter III) and

$$n_{C_Q,i} = jV_i \sin(\phi_i + \rho_n). \quad (147)$$

Similar to the uniform position error case, we will derive an expression for the mean value of the in-phase and quadrature components for each stack and then use these expressions to derive an estimate of the signal phase. Also similar to the uniform random variable case, each node's  $n_{C_I,i}$  and  $n_{C_Q,i}$  in a stack can be interpreted as the  $i^{\text{th}}$  instance of the in-phase random variable  $n_{C_I}$  and the quadrature random variable  $n_{C_Q}$ .

Focusing on the in-phase component first, the expression  $\phi_i + \rho_n$  can be expressed as a Gaussian random variable  $\delta_g$  with a mean of

$$\mu_g = \phi_i \quad (148)$$

and variance of

$$\sigma_g^2 = (\beta \sigma_p)^2. \quad (149)$$

By substituting  $\delta_g$  into  $n_{C_l}$ , we get

$$n_{C_l} = \cos(\delta_g). \quad (150)$$

To derive the resulting probability density function of  $n_{C_l}$ , we first define its cumulative distribution function as

$$F_{N_{C_l}}(n_{C_l}) = \Pr[g(\delta_g) \leq n_{C_l}] = \int_{g(\delta_g) \leq n_{C_l}} f_{H_g}(\delta_g) d\delta_g, \quad (151)$$

where  $g(\delta_g) = \cos(\delta_g)$ . Since a Gaussian random variable is define between  $-\infty$  and  $\infty$ ,

$\delta_g$  can be defined by the inverse transform of  $g(\delta_g)$  over the interval [84]

$$2\pi k + \cos^{-1}(n_{C_l}) \leq \delta_g < 2\pi(1+k) - \cos^{-1}(n_{C_l}). \quad (152)$$

The probability density function of  $n_{C_l}$  is then expressed as [81], [86]

$$f_{N_{C_l}}(n_{C_l}) = \sum_{k=-\infty}^{\infty} \left| \frac{d\delta_g}{dn_{C_l}} \right| \left( f_H(2\pi k + \cos^{-1}(n_{C_l})) + f_H(2\pi(1+k) - \cos^{-1}(n_{C_l})) \right), \quad (153)$$

where

$$\left| \frac{d\delta_g}{dn_{C_l}} \right| = \frac{1}{\sqrt{1-n_{C_l}^2}}. \quad (154)$$

By expanding (153), we get the final expression for the probability density function of  $n_{C_l}$  as

$$f_{N_{C_l}}(n_{C_l}) = \sum_{k=-\infty}^{\infty} \frac{1}{\sqrt{1-n_{C_l}^2}} \frac{1}{\sqrt{2\pi\sigma_g^2}} \left( \exp\left(-\frac{A_\gamma - \phi_t}{2\sigma_g^2}\right) + \exp\left(-\frac{B_\gamma - \phi_t}{2\sigma_g^2}\right) \right), \quad (155)$$

where  $A_\gamma = 2\pi k + \cos^{-1}(n_{C_l})$  and  $B_\gamma = 2\pi(1+k) - \cos^{-1}(n_{C_l})$ .

To support the validity of this expression, a comparison of the histogram of  $n_{C_l} = V_i \cos(\delta_g)$  with the response of (155) over the same interval is shown in Figure 47. For this simulation, 10,000 instances of  $\delta_g$  generated to form a histogram with 50 bins,  $\sigma_g^2 = (2\pi/5)^2$ , and  $f_{N_{C_l}}(n_{C_l})$  is calculated with  $k = 0, 1$ . As observed from the results, the simulated histogram closely follows the theoretical values of (155).

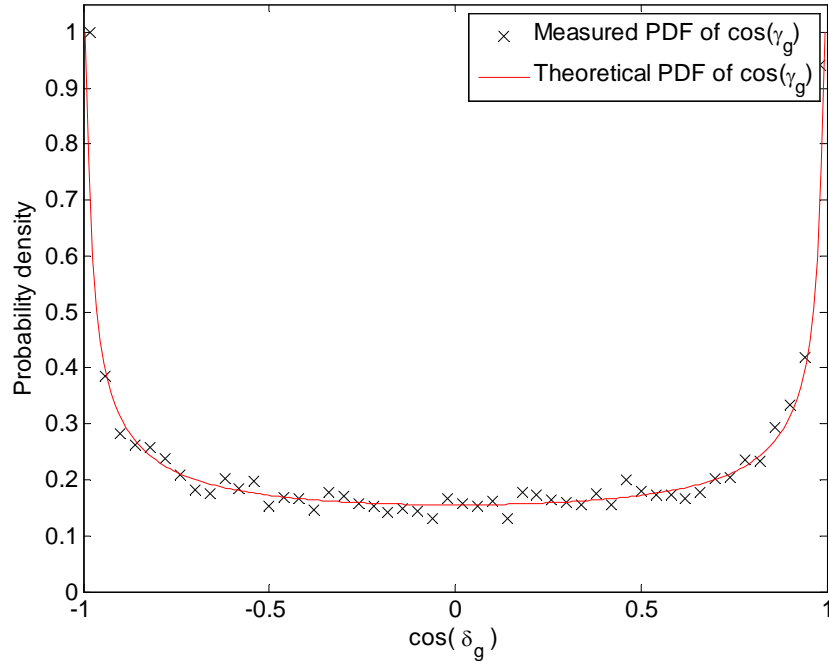


Figure 47. Comparison of measured and theoretical probability density function (pdf) of  $n_{C_l}$ . Signal phase  $\phi_t = 0$  and measured pdf based on histogram using 10,000 points and 50 bins.

## 1. Mean Value of the In-Phase and Quadrature Components with Gaussian Position Errors

With the probability density function of  $n_{C_i}$  defined as a function of  $\phi_i$  and  $\sigma_g^2$ , we can derive an estimate of  $\phi_i$  at a given stack based on the sample mean of  $n_{C_i}$  and knowledge of  $\sigma_g^2$ . Since it is difficult to derive an expression for the mean using the probability density function of  $n_{C_i}$ , we take an alternative approach using Euler's formula

$$e^{i\delta_g} = \cos\delta_g + j\sin\delta_g. \quad (156)$$

We will first consider the case where  $\delta_g$  is Gaussian with a mean value of zero and a variance of  $\sigma_g^2$ . Note that the mean value of  $\delta_g$  is indeed equal to  $\phi_i$  (see (148)), but we will first examine this simpler zero mean case in order to derive the non-zero mean case. The mean of the cosine term is then given as [87]

$$E\{\cos\delta_g\} = \exp(-\sigma_g^2 / 2), \quad (157)$$

and

$$E\{\sin\delta_g\} = 0. \quad (158)$$

Using the trigonometric identity

$$\cos^2 \delta_g = \frac{1}{2} \left( 1 + \cos(2\delta_g) \right), \quad (159)$$

the variance of  $\cos\delta_g$  can be expressed as

$$\text{var}\{\cos\delta_g\} = E\{\cos^2\delta_g\} - E\{\cos\delta_g\}^2. \quad (160)$$

By substituting (157) and (159) into (160), we get

$$\text{var}\{\cos\delta_g\} = \frac{1}{2}\left(1 + e^{-(2\sigma_g)^2/2}\right) - e^{-\sigma_g^2} = \frac{1}{2}\left(1 - e^{-\sigma_g^2}\right)^2. \quad (161)$$

Similarly, the variance of  $\sin\delta_g$  is given by

$$\text{var}\{\sin\delta_g\} = E\{\sin^2\delta_g\} - E\{\sin\delta_g\}^2 = \frac{1}{2}\left(1 - e^{-2\sigma_g^2}\right). \quad (162)$$

Finally to consider the case where  $\delta_g$  is not zero mean, where  $\delta_g$  is a Gaussian random variable with mean  $\mu_g = \phi_t$  and variance equal to  $\sigma_g^2$ . If this is true, then  $\delta_0 = \delta_g - \mu_g$  where  $\delta_0$  is the zero mean case of  $\delta_g$ . Thus, using the trigonometric identity  $\cos(x + y) = \cos x \cos y - \sin x \sin y$ , the mean of  $\cos(\delta_g)$  can be expressed as

$$E\{\cos\delta_g\} = E\{\cos(\delta_0 + \mu_{\delta_g})\} = E\{\cos\delta_0\cos\mu_g - \sin\delta_0\sin\mu_g\} = e^{-\sigma_g^2/2}\cos\mu_g. \quad (163)$$

Similarly,

$$E\{\sin\delta_g\} = E\{\sin(\delta_0 + \mu_g)\} = e^{-\sigma_g^2/2}\sin\mu_g. \quad (164)$$

Since  $n_{C_t} = \cos(\delta_g)$ , the mean of  $n_{C_t}$  is given as

$$E\{n_{C_t}\} = e^{-\sigma_g^2/2}\cos\mu_g. \quad (165)$$

Following the same derivation, the mean of  $n_{C_q}$  is expressed as

$$E\{n_{C_q}\} = e^{-\sigma_g^2/2}\sin\mu_g. \quad (166)$$

## 2. Phase Estimates Using Sampled Base Band Signals

Given that the signal phase is perturbed by sensor position errors, as shown in Chapter V section B, the mean value of the signal's phase remains largely unaffected. This makes the sample mean of a given stack's signal phase a suitable parameter from which to estimate the true signal phase.

One means of estimating the signal phase is by solving (163) or (165) for  $\phi_t$ , to obtain the phase estimate for the center stack

$$\hat{\phi}_{t,c} = \cos^{-1} \left( \hat{\mu}_{n_{cI}} / e^{-\sigma_s^2/2} \right) = \sin^{-1} \left( \hat{\mu}_{n_{cQ}} / e^{-\sigma_s^2/2} \right), \quad (167)$$

where  $\hat{\mu}_{n_{cI}}$  and  $\hat{\mu}_{n_{cQ}}$  are the signal's in-phase and quadrature component's sample mean for the center stack. This method, although valid, only uses the samples from either component. The preferred approach is to use both base band signal samples by taking the ratio of (166) and (165) as

$$\frac{E\{n_{cQ}\}}{E\{n_{cI}\}} = \frac{e^{-\sigma_s^2/2} \sin \mu_{\delta_s}}{e^{-\sigma_s^2/2} \cos \mu_{\delta_s}} = \frac{\sin \mu_{\delta_s}}{\cos \mu_{\delta_s}}. \quad (168)$$

Since  $\mu_{\delta_s} = \hat{\phi}_{t,c}$ , an estimate of  $\hat{\phi}_{t,c}$  is expressed as

$$\hat{\phi}_{t,c} = \tan^{-1} \left( \frac{\hat{\mu}_{n_{cQ}}}{\hat{\mu}_{n_{cI}}} \right). \quad (169)$$

This same phase estimation method is then used for the other two stacks in the array. The final signal phase estimate  $\hat{\phi}_t$  is then the average of these three estimates. Since the ASLA array is symmetrical about the y-axis, taking the average of the estimates will also

compensate for the minor errors in the arrays reorientation, i.e., errors in the estimate  $\hat{\theta}_t$ . The estimated complex signal for the  $n^{\text{th}}$  stack is then expressed as

$$\hat{\Omega}_n = \exp(j\hat{\phi}_t), \quad (170)$$

We then sum the estimates of all three stacks to obtain the final main beam response as

$$\hat{\Omega}_t = \sum_{n=1}^3 \hat{\Omega}_n \quad (171)$$

### 3. Performance of the Signal Collection Scheme in the Presence of Gaussian Sensor Position Errors

To evaluate the proposed scheme's performance in the presence of Gaussian sensor position errors, we conducted a series of Monte Carlo simulations. The results of these simulations focus on the root mean-square error for signal magnitude ( $\xi_v$ ) and phase ( $\xi_\phi$ ) estimate. For comparison, the no-estimation case, i.e., beamforming without signal estimation, is also shown. For each of these simulations,  $\lambda = 1$  m, the source emitter is located at  $\omega_t = [2000 \text{ m}, 15 \text{ deg}]^T$ ,  $r_a = 200$  meters, and  $N_s = 10$ . All data points are the result of 10,000 trials.

A comparison of the scheme's root mean-square error of normalized magnitude  $\xi_v$  with and without signal estimation as a function of the standard deviation of Gaussian position error  $\sigma_g$  is shown in Figure 48. In this simulation, to isolate the effect position error, the target signal's  $\theta_t$  is known *a priori*. From the results, we can see that the estimated case outperforms the no-estimation case at all values of  $\sigma_g$  simulated. This suggests that signal estimation provides an effective means of reducing the effects of Gaussian position errors.

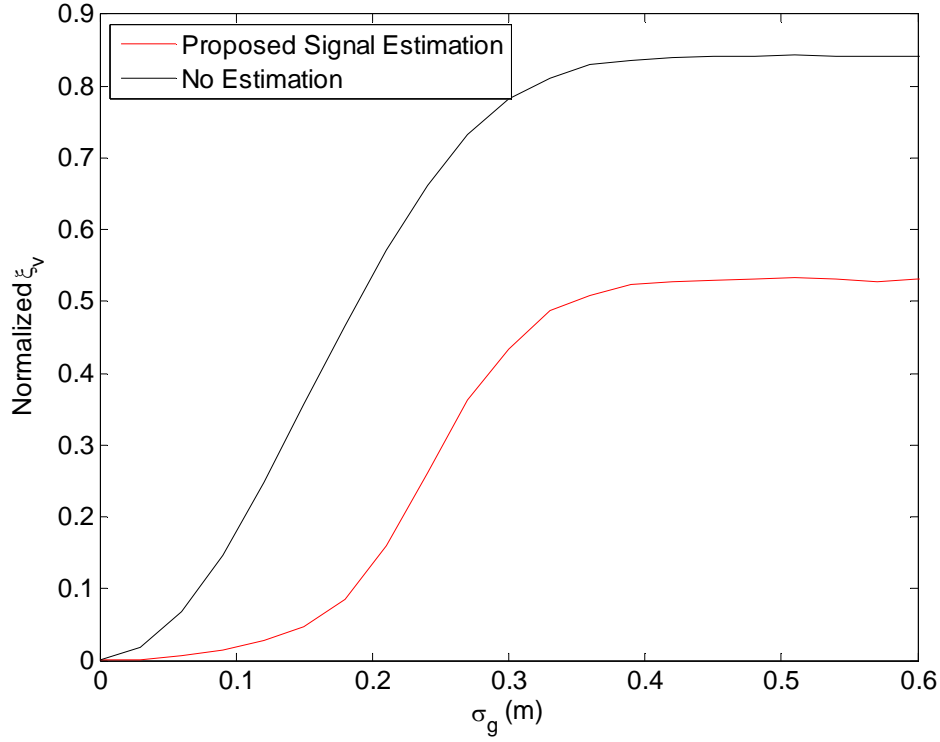


Figure 48. Root mean-square error of normalize magnitude versus the standard deviation of Gaussian position error  $\sigma_g$ . Results based on 10,000 trials with  $N_s = 10$ ,  $r_a = 200$  m, and  $\boldsymbol{\omega}_t = [2000 \text{ m}, 15 \text{ deg}]^T$ .

The scheme's  $\xi_\phi$  as a function of Gaussian position error  $\sigma_g$  is shown in Figure 49. Similar to the previous simulation, we assumed the target signal's  $\theta_t$  is known *a priori*. From the results, we observe no noticeable difference in the  $\xi_\phi$  between the proposed signal estimation case and the no-estimation case. Similar to the uniform position error case, this suggests that the proposed signal estimation technique does not improve the accuracy of the main beam signal phase, but as seen in Figure 48 does improve its magnitude gain.

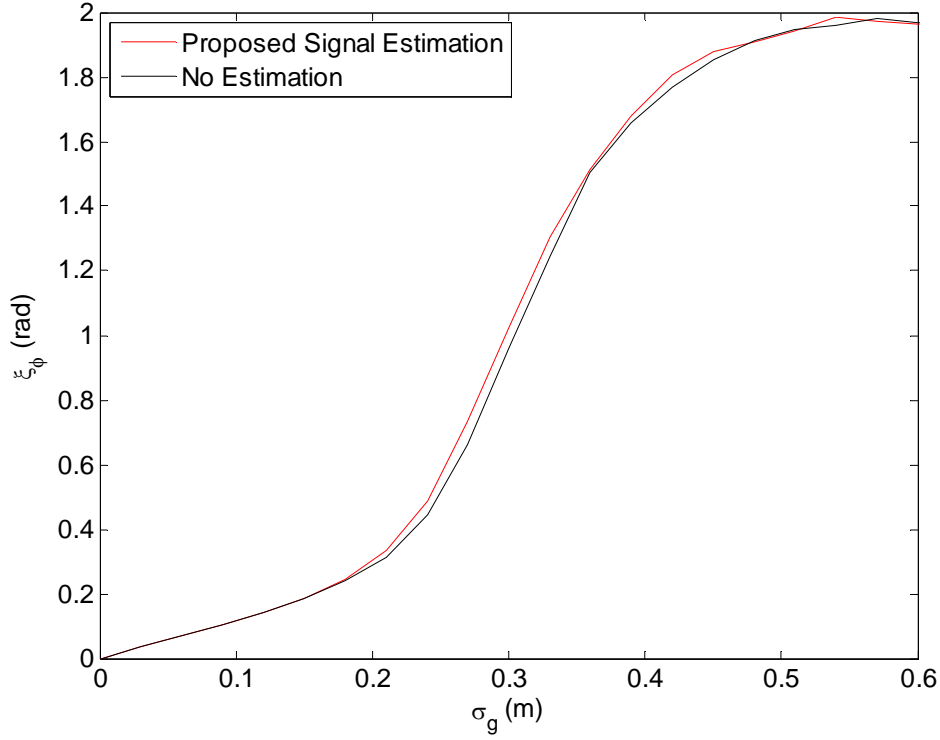


Figure 49. Root mean-square error phase  $\xi_\phi$  versus the standard deviation of Gaussian position error  $\sigma_g$ . Results based on 10,000 trials with  $N_s = 10$ ,  $r_a = 200$  m, and  $\omega_t = [2000 \text{ m}, 15 \text{ deg}]^T$ .

The scheme's  $\xi_v$  as a function of RDOA noise variance  $\sigma_{RD}^2 = c^2 \sigma_R^2$  is shown in Figure 50. In this simulation, the scheme is evaluated at two levels of position error with  $\sigma_g = 0$  and  $\sigma_g = 1/5$  m. From the results, we can see that the proposed scheme and no-estimation case have the same performance when no position errors are present. When position errors are introduced, we see that the proposed scheme outperform the no-estimation case. Of interest, we see that the scheme also outperforms the same case with no position error for values of RDOA noise greater than 2 dB. This would suggest that at a given  $\sigma_{RD}^2$  level, position errors become less of a factor than errors in  $\hat{\theta}_t$ .

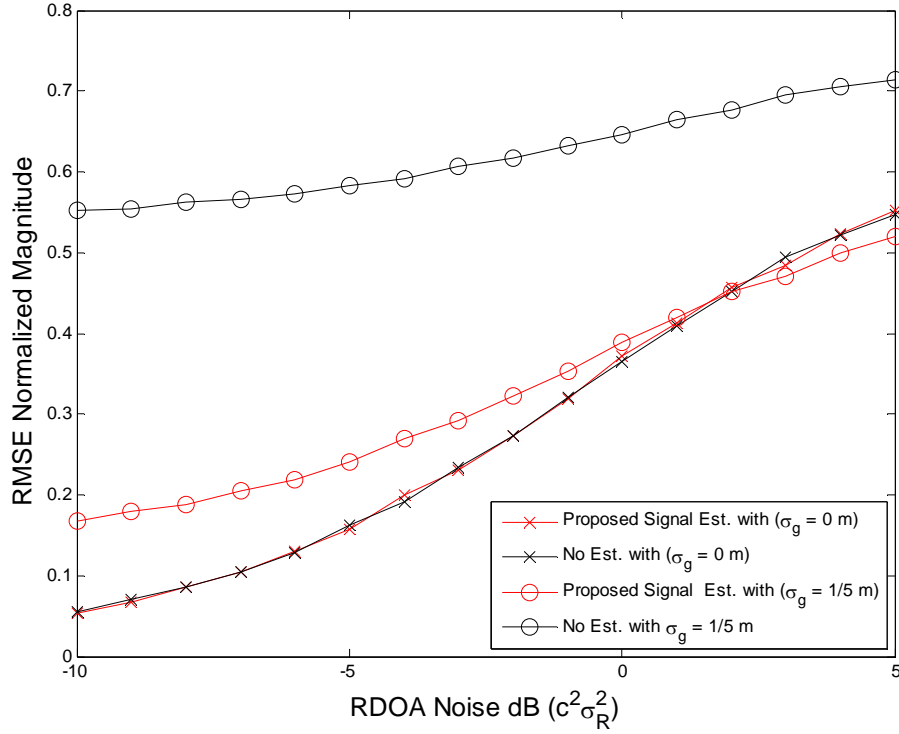


Figure 50. Root mean-square error of normalize magnitude versus RDOA noise.  
Results based on 10,000 trials with,  $N_s = 10$ ,  $r_a = 200$  m, and  
 $\omega_t = [2000 \text{ m}, 15 \text{ deg}]^T$ .

A comparison of the scheme's  $\xi_\phi$  as a function of  $\sigma_{RD}^2$  is shown in Figure 51. Similar to the previous simulation, the performance was evaluated at two levels of position error,  $\sigma_g = 0$  and  $\sigma_g = 1/5$  m. Similar to Figure 49, we can see that the proposed scheme and no-estimation case have the same performance with or without position errors. Also, similar to the previous simulation, we see that the cases with position error beat the no position error cases at values of RDOA noise greater than 2 dB.

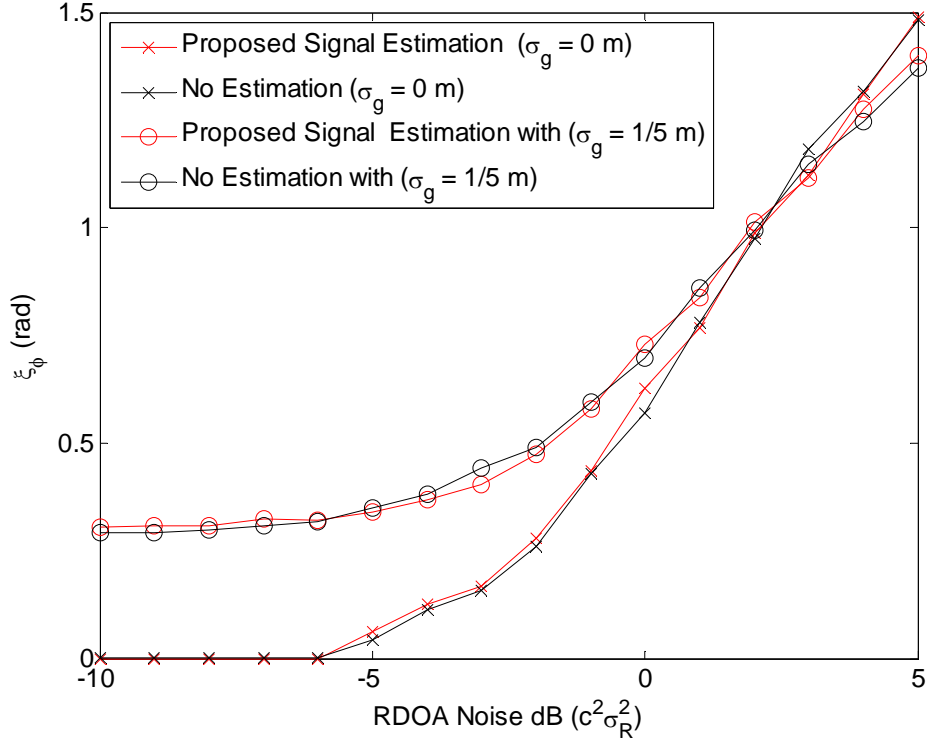


Figure 51. Root mean-square error Phase  $\xi_\phi$  versus RDOA noise. Results based on 10,000 trials with,  $N_s = 10$ ,  $r_a = 200$  m, and  $\omega_t = [2000 \text{ m}, 15 \text{ deg}]^T$ .

### E. GRATING LOBE SUPPRESSION VIA VIRTUAL FILLING

From (55) and (56), we know that increasing the distance  $r_a$  between the outer and center stacks (see Figure 6) will provide increased localization performance, but increasing this distance essentially increases the inter-node distance  $d$  in (28). If the inter-node distance of an array is greater than  $\lambda/2$ , multiple grating lobes will appear in the array factor [71]. Since grating lobes have the same magnitude response as the main beam, they will significantly reduce the array's interference rejection capabilities.

To combat the effects of grating lobes, we propose the use of virtual filling. Given that the directions of arrival of all signals are known, virtual filling interpolates the response of a virtual uniform linear array based on signal estimates from the real array [76]. In virtual filling, any gap between array nodes larger than  $\lambda/2$  is filled in with virtual complex signal data.

With the ASLA symmetrically populated only along the x-axis and centered on the origin, the position of the  $n^{\text{th}}$  virtual node is expressed as

$$x_{v,n} = -r_a + n_v d_a, \quad n_v = 0, 1, \dots, N_v - 1 \quad (172)$$

where the virtual inter-node distance  $d_a = \lambda / 2$  and  $N_v$  is the total number of virtual elements given as

$$N_v = \frac{2r_a}{d_a} + 1. \quad (173)$$

To fill in the complex data of the virtual array, we begin by populating the vector  $A_n$  from (51) with the signal estimates  $\Omega_n$ . Using the least-squares method described in Chapter II, an estimate of each signal's magnitude and phase is obtained. The response of the  $n^{\text{th}}$  virtual node is then expressed as

$$\Omega_{v,n} = \sum_{i=1}^{N_R} V_{t,i} e^{j\phi_{t,i}} e^{j\beta(x_{v,n} \sin \theta_{t,i})} \quad (174)$$

where  $N_R$  is the number of signals present,  $i = 1, \dots, N_R$ , and  $V_{t,i}$ ,  $\phi_{t,i}$ ,  $\theta_{t,i}$  are the  $i^{\text{th}}$  signal's magnitude, phase, and bearing, respectively. Once filled out, the ASLA then becomes a virtual uniform linear array. Since the internode distance is now  $\leq \lambda / 2$ , the presence of grating lobes is significantly reduced. Furthermore, various tapering methods (see Chapter II) can be applied to manage the remaining sidelobes.

With no errors present, the array factor of an  $N_s = 5$  ASLA configured network is shown in Figure 52. For this simulation,  $\lambda = 1$  m and  $r_a = 200 \lambda$ . From the plot, we can see that with  $r_a \gg \lambda / 2$ , there are numerous grating lobes and side lobes in the array factor.

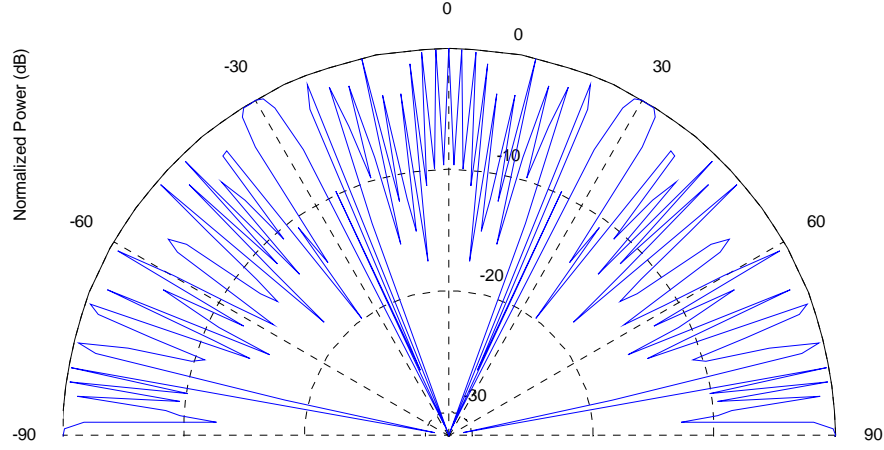


Figure 52. Normalized Array factor of an  $N_s = 5$  ASLA phase shift beamformer before virtual filling process. Simulation based on  $r_a = 200$  m, and  $\omega_t = [2000 \text{ m}, 45 \text{ deg}]^T$ .

Now, with virtual filling and tapering applied, the array factor of the ASLA is shown in Figure 53. With the virtually filled array having no inter-node spacing greater than  $\lambda/2$ , we can see from the plot that all the grating lobes have been eliminated. By applying a binomial taper (see Chapter II) the sidelobes have also been suppressed, resulting in a strong main beam lobe.

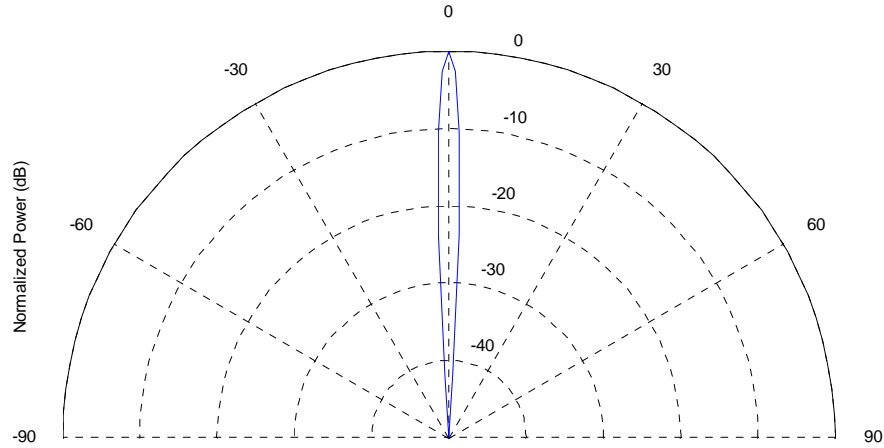


Figure 53. Normalized Array factor of an  $N_s = 5$  ASLA phase shift beamformer with virtual filling process with binomial tapering. Simulation based on,  $r_a = 200$  m, and  $\omega_t = [2000 \text{ m}, 45 \text{ deg}]^T$ .

A comparison of the signal estimation scheme with and without virtual filling is shown in Figure 54 and Figure 55. In this simulation, there is an interfering signal in addition to the target signal,  $\lambda = 1$  m, uniform position error  $\delta_p = 1/20$  m, and the ASLA formation consists of  $N_s = 10$  with  $r_a = 100$  m. The target signal's  $\theta_t = 0$  deg,  $V_s = 1$ , and  $\phi_s = 60$  deg. The interfering signal's  $\theta_i = 55$  deg,  $V_s = 1$ , and  $\phi_s = 25$  deg.

The magnitude and phase estimate values of the main beam for 100 trials without virtual filling are shown in Figure 54. From the results, we can see that the interfering signal corrupts the target signal, thus resulting in an erroneous main beam response. In contrast, the main beam signal values using virtual filling are shown in Figure 55. From the results, it is clear that the virtual filling has reduced the effects of the interfering signal and has improved the signal estimate.

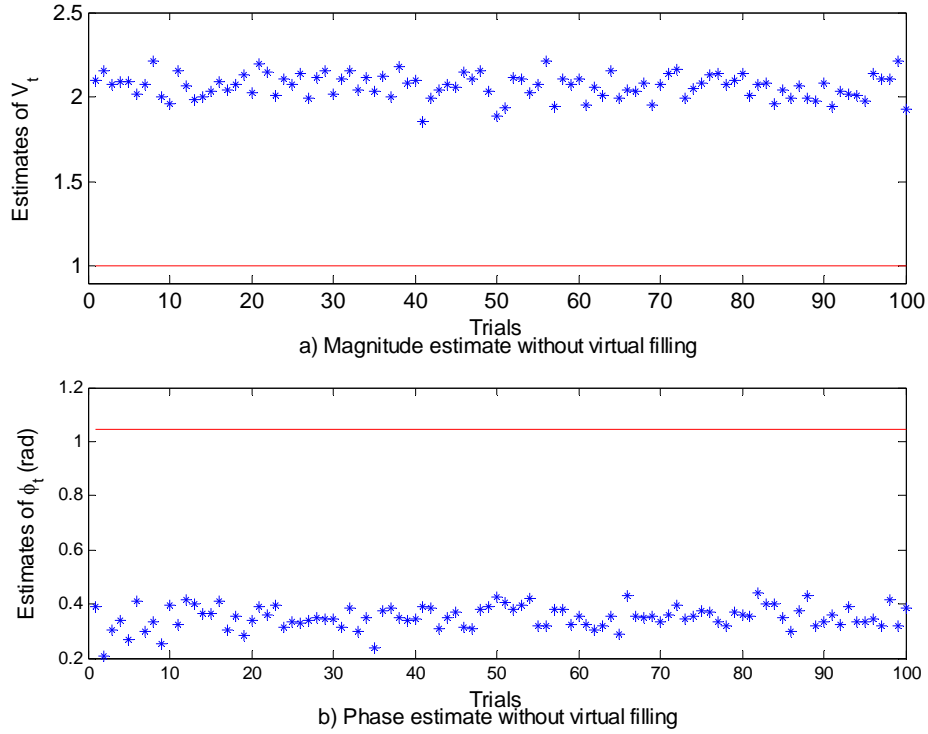


Figure 54. Signal Estimation without virtual filling. Simulation based on,  $r_a = 100$  m, target signal's  $\theta_t = 0$  deg,  $V_s = 1$ , and  $\phi_s = 60$  deg. The interfering signal's  $\theta_i = 55$  deg,  $V_s = 1$ , and  $\phi_s = 25$  deg. The true signal phase and magnitude is shown in red.

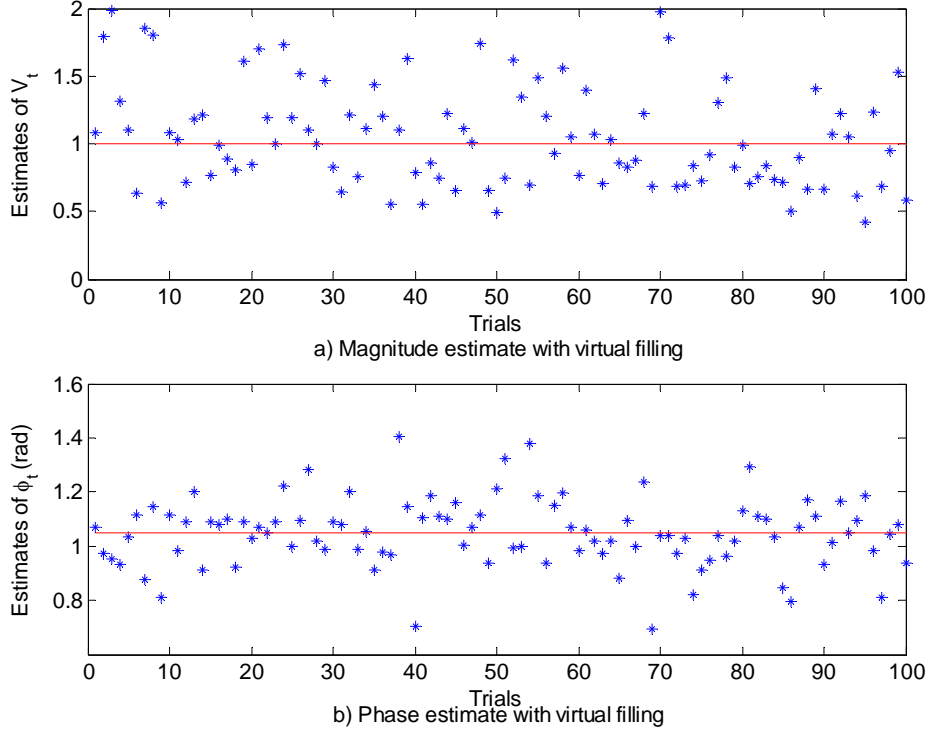


Figure 55. Signal estimation with virtual filling. Simulation based on,  $r_a = 100$  m , target signal's  $\theta_t = 0$  deg ,  $V_s = 1$ , and  $\phi_s = 60$  deg . The interfering signal's  $\theta_t = 55$  deg ,  $V_s = 1$ , and  $\phi_s = 25$  deg . The true signal phase and magnitude is shown in red.

A comparison of the main beam's angular root mean squared error  $\xi_\phi$  for the proposed scheme with and without virtual filling as a function of maximum uniform position error  $\delta_p$  is shown in Figure 56. In this simulation, there is one signal-of-interest and one interfering signal, the target signal's  $\theta_t = 0$  deg ,  $V_t = 1$ , and  $\phi_t = 60$  deg , the interfering signal's  $\theta_t = 55$  deg ,  $V_t = 1$ ,  $\phi_t = 25$  deg , and  $r_a = 100$  m ; and all data points are the result of 1,000 trials. From the results, we see in the no virtual filling case that the benefits of the signal estimation are nullified by the presence of an interfering signal. In contrast, when virtual filling is applied, the interfering signal is significantly reduced, thus improving the signal phase estimate. Overall, this result demonstrates the proposed scheme's effectiveness in the presence of both position errors and an interfering signal.

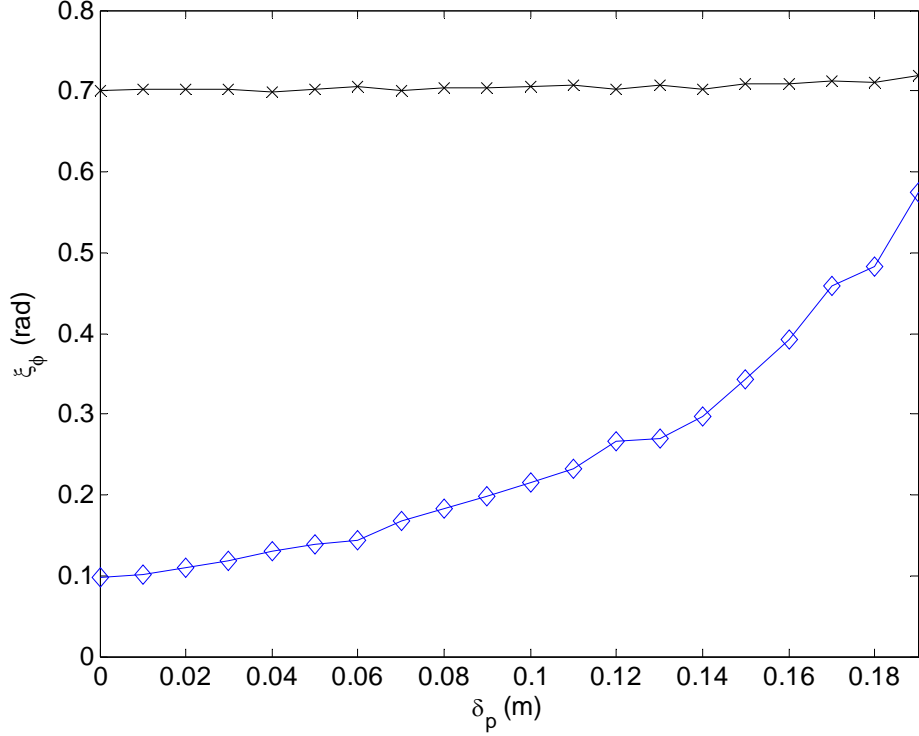


Figure 56. Proposed scheme's  $\xi_\phi$  with virtual filling (blue) and without (black) versus maximum uniform position error  $\delta_p$  in the presence of one interfering signal. In this simulation,  $r_a = 100$  m, the target signal's  $\theta_t = 0$  deg,  $V_t = 1$ , and  $\phi_t = 60$  deg, the interfering signal's  $\theta_i = 55$  deg,  $V_i = 1$ , and  $\phi_i = 25$  deg, and all data points are the result of 1,000 trials.

In this chapter, we studied collaborative signal collection in the presence of noise, sensor position errors, and interfering signals. We developed a signal estimation method that utilizes sampled array data and knowledge of the positional error statistics to combat these errors. We further enhanced its robustness against interfering signals by using a virtual filling and tapering techniques to minimize the array's grating lobes and side lobe response. Using simulation, we were able to validate the proposed scheme's effectiveness in the presence of such errors and achieve the intended objective of this dissertation.

## VI. CONCLUSION

Performing collaborative beamforming from an elevated, mobile wireless sensor network requires a coordinated interplay of many different signal processes and technologies. The objective of this research was to maximize signal collection performance in the presence of various signal and sensor related errors from an elevated, mobile wireless sensor network. To accomplish this objective, we proposed a signal collection scheme that exploits an elevated, mobile network to maximize the collaborative collection of a target signal.

The proposed scheme begins with an accurate source localization technique, which is used to determine the signal's position and bearing. This information was then used by a collaborative beamformer to maximize the collection of that target signal. Both of these phases are enhanced by the versatile nature of an elevated, mobile network. The mobility allows for the reconfiguration of the sensor network's topology to help create an ideal sensor-target geometry. This geometry allows for optimal localization estimates to be obtained. The ability of an elevated network capable of creating sensor stacks allows for robust signal collection operations in the presence of uniform and Gaussian sensor position errors.

In the localization technique, to obtain precise localization in the presence of noise and uniform position errors, we proposed the use of two sequential location estimators. This technique consists of an initial weighted least-squares estimate followed by a maximum-likelihood estimate. The second estimate uses the initial estimate to reorient the network. This reorientation creates an ideal sensor to target geometry [17]. This new orientation minimizes the geometric dilution of precision [52], minimizing the maximum-likelihood estimator's error variance. Simulation results showed the proposed localization technique to be efficient, i.e., the variance of the estimation error approaches the Cramer-Rao lower bound.

To enhance the localization technique's performance, we developed a measurement outlier rejection process that mitigates the effects of measurement and

sensor position errors. This technique uses a combination of single case diagnostics and the Mahalanobis distance to identify and remove erroneous measurements from the least-squares estimate. Through simulation, we demonstrated this technique to be effective in the presence of both measurement and position errors. For the case where only position errors are present, the technique was found to be effective only for high levels of position errors.

For the signal collection technique, we began by analyzing the effects of sensor position errors on the array factor and its main beam gain. We then derived an expression for the effects of both uniform and Gaussian position errors on the array's main beam gain. Through simulation, we validated our results and showed that the mean value of the main beam signal phase was unaffected by position errors. To enhance the signal collection performance in the presents of these errors, we developed a signal estimator for both uniform and Gaussian position errors. Simulation results yielded an improvement in array gain of approximately 37 percent for the standard deviation of position error values greater than 0.4 m.

Taking advantage of the concept of a unique elevated, mobile wireless sensor network realized through the use of multirotor UAVs, our scheme used two existing localization techniques to deliver a precise source location estimate. Using this information with statistical knowledge of the sensor position errors in a signal estimator, we derived a novel collaborative signal collection scheme. This scheme was shown to be capable of collecting and amplifying a target signal in the presence of such errors. With all these techniques in concert, the objective of this dissertation to maximize signal collection in the presence of various signal- and sensor-related errors was achieved.

## **A. SIGNIFICANT CONTRIBUTIONS**

With the objective to maximize signal collection performance in the presence of various signal and sensor related errors, a novel scheme for robust signal collection from an elevated, mobile network was proposed.

To enable the signal collection, a localization step was required. To accomplish this task, a two-stage localization technique was proposed. Using an optimal ASLA

sensor formation for target localization, we minimized the network's geometric dilution of precision, effectively lowering the estimate's Cramer-Rao lower bound. By utilizing two unique location estimators in sequence, we created a hyperbolic location estimate capable of approaching the Cramer-Rao lower bound.

To enhance the localization robustness, a measurement outlier rejection process was proposed. Using the Mahalanobis distance as a measure of solution divergence, we were able to identify and remove erroneous measurements from the location estimate. As a result, the localization estimation technique demonstrated increased resilience to both measurement and sensor position errors.

To better understand the effects of position errors in collaborative beamforming, an expression for uniform and Gaussian sensor position error effects on an ASLA formation's main beam gain were developed. The main result was the validation that position errors in the ASLA formation have no effect on the mean value of the signal phase, which was instrumental in the development of a novel signal estimator used to compensate for such errors.

Finally, a signal collection scheme that combines a novel signal estimator and collaborative beamforming to successfully collect a target signal despite the effects of sensor position errors was proposed. Compensating for both uniform and Gaussian errors, the signal estimator uses sampled array data, sensor stack formations, and knowledge of the positional error statistics to accomplish this task. Through simulation we were able to demonstrate significant improvement over the conventional beamforming. To further enhance the collection capability for noise and interference rejection, we also adapted the use of virtual filling and tapering to manage the array's grating lobes and sidelobes.

## **B. FUTURE RESEARCH**

With the research and development of localization and signal collection consistently changing and growing, there are a number of possible extensions to the research presented in this dissertation.

The key error parameter evaluated in this research was sensor position errors modeled as a uniform or Gaussian random variable. The assumption of specific probability density functions affects many aspects of each of the techniques and methods developed in this research. Further research focused on a general approach to treat position errors independent of a probability distribution should be considered in order to fully investigate their effects on signal collection.

The robust source localization technique presented here focused on a single case diagnostic. This method assumes that single data points act alone to offset the true solution. It has been shown that multiple points in unison may also have a stronger effect than an individual data point [18]. Given this, exploring the use of outlier subset rejection in the context of hyperbolic localization may lead to more beneficial results.

Both source localization and collection operations presented here assume a line-of-sight signal path between each sensor and the transmitter. Further research is needed to adapt the scheme for use in a non-line-of-sight environment where there is also a multipath component to each signal path.

With all wireless signal processing operations, there must be a consideration for the wireless communication scheme as well. Further research is required to evaluate signal collection from an elevated, mobile network in the context of standard digital wireless modulation schemes, such as binary phase-shift keying, quadrature phase-shift keying, and quadrature amplitude modulation. Additional effort should be devoted to the orthogonal frequency-division multiple access signals [85].

## APPENDIX. SELECTED SIMULATION CODE

### Script Name: Two-Stage Localization Versus RDOA Noise

```

clc; close all; clear all; warning off; % Program
initialization.
L = 10000; % Number of
ensemble runs.
c = 3e8; %signal propagation speed;
LL = 400; %deployment diameter
r = 2500; %range from origin to source
theta_tx = degtorad(60); %This is from the x-axis
uo = [r*cos(theta_tx) r*sin(theta_tx)]';
% True source position.

NN=5; %Number of nodes per stacks, total sensor = 3*NN
x=[ 0*ones(1,NN) -(LL/2)*ones(1,NN) (LL/2)*ones(1,NN)];
% True sensor position matrix.
y=zeros(1,length(x));
S=[x; y];

M = size(S,2); % Number of sensors.
LM=length(x);
N = size(S,1); % Dimension of
localization.
MLE_runs = 1;
ro = sqrt(sum((uo*ones(1,M)-S).^2))'; % True source-
sensor ranges
rdo = ro(2:end)-ro(1);

R = (eye(M-1)+ones(M-1))/2; % covariance
structure of TDOA
R2 = (eye(LM-1)+ones(LM-1))/2;
NsePwrVecdB=-10:1:5;
TSweighted least-squares= zeros(2,1);
Linear_MLE = zeros(2,1);
fprintf('Simulation in progress');

for nseIdx=1:length(NsePwrVecdB), % vary measurement
noise level
    fprintf(' ');
    nsePwr = 10^(NsePwrVecdB(nseIdx)/10);
    Q = nsePwr * R; % Covariance matrix
of TDOA (range difference) noise
    Q2 = nsePwr * R2;
    crlb(nseIdx)=sqrt(trace(TDOALocCRLB_lin(S,uo,Q)));

```

```

        Linear_range =
        (((1/nsePwr)*c^2*(1/(c*(r)^2))^2*(LL/2)^4 *(LM/8))^( -1));
        crlb_LM(nseIdx)=sqrt(Linear_range);
%
        Linear_bearing = (((2/nsePwr)*c^2*(1/(c^2))*(LL/2)^2
*(LM))^( -1));
        crlb_LM_bearing(nseIdx)=sqrt(Linear_bearing);

        SimulationMSE1 = 0;
        SimulationMSE2 = 0;
        SimulationMSE3 = 0;

        SimulationMSE1_bearing = 0;
        SimulationMSE2_bearing = 0;
        SimulationMSE3_bearing = 0;

        for k = 1 : L,                                % Monte Carlo
Simulation.
            rdNse = sqrt(nsePwr/2) * randn(M,1);
            rdNse1 = sqrt(nsePwr/2);
            rd = rdo + rdNse(2:end)-rdNse(1);          % Noisy source
TDOAs (range differences).
            u1 = TDOALoc_LINEAR(S,rd,Q);
            [u2, senor_pos] =
Linear_second_stage_polar_RDOA(atan2(u1(2),u1(1)),LM,LL/2,M
LE_runs,[norm(uo,2),atan2(uo(2),uo(1))]',rdNse1,[norm(u1,2)
,atan2(u1(2),u1(1))]' );
            u2 = [u2(1)*cos(u2(2));u2(1)*sin(u2(2))];
            [u3, senor_pos1] =
Linear_second_stage_polar_RDOA(atan2(u1(2),u1(1)),LM,LL/2,M
LE_runs+3,[norm(uo,2),atan2(uo(2),uo(1))]',rdNse1,[norm(u1,
2),atan2(u1(2),u1(1))]' );
            u3 = [u3(1)*cos(u3(2));u3(1)*sin(u3(2))];

            SimulationMSE1 = SimulationMSE1 + norm(u1-uo,2)^2;
            SimulationMSE2 = SimulationMSE2 + norm(u2-uo,2)^2;
            SimulationMSE3 = SimulationMSE3 + norm(u3-uo,2)^2;
            SimulationMSE1_bearing = SimulationMSE1_bearing +
(atan2(u1(2),u1(1))-theta_tx)^2;
            SimulationMSE2_bearing = SimulationMSE2_bearing +
(atan2(u2(2),u2(1))-theta_tx)^2;

```

```

        SimulationMSE3_bearing = SimulationMSE3_bearing +
        (atan2(u3(2),u3(1))-theta_tx)^2;
    end;
    mse1(nseIdx) = sqrt(SimulationMSE1/L);
    mse2(nseIdx) = sqrt(SimulationMSE2/L);
    mse3(nseIdx) = sqrt(SimulationMSE3/L);
    mse1_bearing(nseIdx) = sqrt(SimulationMSE1_bearing/L);
    mse2_bearing(nseIdx) = sqrt(SimulationMSE2_bearing/L);
    mse3_bearing(nseIdx) = sqrt(SimulationMSE3_bearing/L);
end;
fprintf('\n');

figure(1); plot(NsePwrVecdB,(mse1),'xk','MarkerSize',8);
hold on;
plot(NsePwrVecdB,(mse2),'*r','MarkerSize',8); hold on;
plot(NsePwrVecdB,(crlb),'k');
hold on;
plot(NsePwrVecdB,(crlb_LM),'--g');
grid on; hold off;
xlabel('RDOA Noise STD dB(c\sigma)');
ylabel('RMSE Position (m)');
legend('1st Phase weighted least-squares Estimate','2nd
Phase ML Estimate','1st Phase CRLB RMSE Position', '2nd
Phase CRLB RMSE Position');

figure(3);
plot(NsePwrVecdB,(mse1_bearing),'xk','MarkerSize',8); hold
on;
plot(NsePwrVecdB,(mse2_bearing),'*r','MarkerSize',8); hold
on;
plot(NsePwrVecdB,(crlb_LM_bearing),'-g');
grid on; hold off;
xlabel('RDOA Noise STD dB(c\sigma)');
ylabel('RMSE Bearing (rad)');
legend('1st Phase weighted least-squares Estimate','2nd
Phase ML Estimate','2nd Phase CRLB RMSE Bearing');

```

### Script Name: Signal estimator versus wavelength for uniform position errors

```
clc
clear all
close all
num_run = 1000;
rand('seed', 0)
randn('seed', 0)
c = 3e8;
f = 50:100:2600;
f = f * 1e6;
lambda = c./(f);
k = 2*pi./lambda;

Number_of_real_nodes_Center = 10;
Number_of_real_nodes_Outer = Number_of_real_nodes_Center;
ML = Number_of_real_nodes_Center*3;
%Signal 1
Vs_1_real = 1;
Phase_1_real = degtorad(0);
DOA_1_real = 0;

deploy_radius = 200;

X_center = 0;
Y_center = 0;

X_outer = deploy_radius;
Y_outer = 0;
X = 0;
Y = 0;

SNR = 5;
%%creating random receive matrix
a = -1/10;
b = -a;
aa = -.9e-3;
bb = -aa;
Signal_estimates = zeros(6,1);
Signal_estimates_from_mean = zeros(2,1);
deltaX = b;
deltaY = b;
DOAn = bb;
Tans_weighted_least-squaresE = zeros(2,1);
I_Q_data = zeros(3,1);
DOA_ESTIMATES = zeros(num_run,1);
```

```

RMSE = zeros(4,length(Number_of_real_nodes_Center));
num_pts = Number_of_real_nodes_Center;
for MCR = 1: length(k)

    MCR
    % this is the -15 dB run
    Tans_weighted_least-squaresE = 0;
    for xx = 1:num_run

        XnC = (a + (b-a).*rand(num_pts,1));
        YnC = (a + (b-a).*rand(num_pts,1));
        XnOL = (a + (b-a).*rand(num_pts,1));
        YnOL = (a + (b-a).*rand(num_pts,1));
        XnOR = (a + (b-a).*rand(num_pts,1));
        YnOR = (a + (b-a).*rand(num_pts,1));

        DOA_1_est = Locator_Function([2000;degtorad(70)],-
10) - degtorad(70);

        Rx_sig_center = Vs_1_real.*exp((1i).*(Phase_1_real
+ k(MCR).*((X_center + XnC).*sin(DOA_1_est) + (Y_center +
YnC).*cos(DOA_1_est))));
        Rx_sig_center_w_AWGN = awgn(Rx_sig_center, SNR);
        %Summend Center Signal
        Center_IQ_Est = sum(Rx_sig_center);

        Rx_sig_outer_left =
Vs_1_real.*exp((1i).*(Phase_1_real + k(MCR).*((-
deploy_radius+ XnOL).*sin(DOA_1_est) + (Y_outer +
YnOL).*cos(DOA_1_est))));
        Rx_sig_outer_left_w_AWGN = awgn(Rx_sig_outer_left,
SNR);
        %Estimate Mag and Phase for Left Cluster
        Left_IQ_Est = sum(Rx_sig_outer_left);

        Rx_sig_outer_right =
Vs_1_real.*exp((1i).*(Phase_1_real +
k(MCR).*((deploy_radius+ XnOR).*sin(DOA_1_est) + (Y_outer +
YnOR).*cos(DOA_1_est))));
        Rx_sig_outer_right_w_AWGN =
awgn(Rx_sig_outer_right, SNR);
        %Estimate Mag and Phase for Right Cluster
        Right_IQ_Est = sum(Rx_sig_outer_right);

```

```

        Sig_IQ_est =
abs(sum([Center_IQ_Est;Left_IQ_Est;Right_IQ_Est]))/ML;

        Tans_weighted least-squares = [Tans_weighted least-
squaresE Sig_IQ_est];

    end

    Tans_weighted least-squares = Tans_weighted least-
squaresE(2:end);
    RMSE(1,MCR) = mean(Tans_weighted least-squaresE);

    Tans_weighted least-squares = 0;
    for xx = 1:num_run

        XnC = (a + (b-a).*rand(num_pts,1));
        YnC = (a + (b-a).*rand(num_pts,1));
        XnOL = (a + (b-a).*rand(num_pts,1));
        YnOL = (a + (b-a).*rand(num_pts,1));
        XnOR = (a + (b-a).*rand(num_pts,1));
        YnOR = (a + (b-a).*rand(num_pts,1));

        DOA_1_est = Locator_Function([2000;degtorad(70)],-
5) - degtorad(70);

        Rx_sig_center = Vs_1_real.*exp((1i).*(Phase_1_real
+ k(MCR).*((X_center + XnC).*sin(DOA_1_est) + (Y_center +
YnC).*cos(DOA_1_est))));
        Rx_sig_center_w_AWGN = awgn(Rx_sig_center, SNR);
        %Summend Center Signal
        Center_IQ_Est = sum(Rx_sig_center);

        Rx_sig_outer_left =
Vs_1_real.*exp((1i).*(Phase_1_real + k(MCR).*((-
deploy_radius+ XnOL).*sin(DOA_1_est) + (Y_outer +
YnOL).*cos(DOA_1_est))));
        Rx_sig_outer_left_w_AWGN = awgn(Rx_sig_outer_left,
SNR);

        %Estimate Mag and Phase for Left Cluster
        Left_IQ_Est = sum(Rx_sig_outer_left);

        Rx_sig_outer_right =
Vs_1_real.*exp((1i).*(Phase_1_real +
k(MCR).*((deploy_radius+ XnOR).*sin(DOA_1_est) + (Y_outer +
YnOR).*cos(DOA_1_est))));
        Rx_sig_outer_right_w_AWGN =
awgn(Rx_sig_outer_right, SNR);

```

```

    %Estimate Mag and Phase for Right Cluster
    Right_IQ_Est = sum(Rx_sig_outer_right);

    Sig_IQ_est =
abs(sum([Center_IQ_Est;Left_IQ_Est;Right_IQ_Est]))/ML;

    Tans_weighted least-squaresE = [Tans_weighted
least-squaresE Sig_IQ_est];

end
    Tans_weighted least-squaresE = Tans_weighted least-
squaresE(2:end);
    RMSE(2,MCR) = mean(Tans_weighted least-squaresE);
end
    figure(1)
    plot(lambda,RMSE(1,:),lambda,RMSE(2,:))
    xlabel('Lambda(\lambda)');
    ylabel('Average Normalized Gain');
    legend('RDOA noise STD (-10 dB)','RDOA noise STD (-5
dB)');
    figure(2)
    plot(f./1e6,RMSE(1,:),f./1e6,RMSE(2,:))
    xlabel('Lambda(\lambda)');
    ylabel('Average Normalized Gain');
    legend('RDOA noise STD (-10 dB)','RDOA noise STD (-5
dB)');

```

THIS PAGE INTENTIONALLY LEFT BLANK

## LIST OF REFERENCES

- [1] International Telecommunication Union. (Apr. 2014) ICT facts and figures. [Online]. Available: <http://www.itu.int/en/ITU-D/Statistics/Pages/facts/default.aspx>
- [2] H. Ochiai, P. Mitran, H. V. Poor and V. Tarokh, "Collaborative beamforming for distributed wireless ad hoc sensor networks," *IEEE Trans. Signal Process.*, vol. 53, no. 11, pp. 4110-4124, Nov. 2005.
- [3] J. Krim and M. Viberg, "Two decades of array signal processing research: The parametric approach," *IEEE Signal Processing Mag.*, vol. 13, pp. 67-94, July 1996.
- [4] B. D. Steinberg, *Principles of Aperture and Array System Design*, New York: John Wiley and Sons, 1976.
- [5] Y. T. Chan and K. C. Ho, "A simple and efficient estimator for hyperbolic location," *IEEE Trans. Signal Process.*, vol. 42, no. 8, pp. 1905-1915, Aug. 1994.
- [6] B. D. V. Veen and K. M. Buckley, "Beamforming: a versatile approach to spatial filtering," *IEEE ASSP Mag*, vol. 5, no. 2, pp. 4-24, Apr. 1986.
- [7] J. H. Lee and C. C. Wang, "Adaptive array beamforming with robust capabilities under random sensor position errors," *IEE Proc. Radar, Sonar and Navigation*, vol. 152, no. 6, pp. 383-390, Dec. 2005.
- [8] K. M. Ahmed and R. J. Evans, "Robust signal and array processing," *IEE Proc. F, Commun. Radar Signal Process.*, vol. 129, no. 4, pp. 297-302, Aug. 1981.
- [9] M. H. Er and A. Cantoni, "Derivative constraints for broad-band element space antenna array processors," *EEE Trans. Acoust. Speech Signal Process.*, vol. 31, no. 6, pp. 1378-1393, Dec. 1983.
- [10] J. Li, P. Stoica and Z. Wang, "On robust Capon beamforming and diagonal loading," *IEEE Trans. Signal Process.*, vol. 7, no. 1702-1715, p. 51, July 2003.
- [11] C. Lee and J. Lee, "Robust adaptive array beamforming under steering vector errors," *IEEE Trans. Antennas Propag.*, vol. 45, no. 1, pp. 168-175, Jan. 1997.

- [12] A. Caron, "Surface impact location system," in Proc. *Ocean*, Newport, RI, Sept. 1972.
- [13] B. T. Fang, "Simple solutions for hyperbolic and related position fixes," *IEEE Trans. Aerosp. Electron. Syst.*, vol. 26, no. 5, pp. 748–753, Sep. 1990.
- [14] H. Cramér, *Mathematical Methods of Statistics*, Princeton, NJ: Princeton University Press, 1946.
- [15] J. M. Mendel, *Lessons in Digital Estimation Theory*, Englewood Cliffs, NJ: Prentice-Hall, 1987.
- [16] W. Hahn and S. Tretter, "Optimum processing for delay-vector estimation in passive signal arrays," *IEEE Trans. Inf. Theory*, vol. 19, no. 5, pp. 608–614, Sept. 1973.
- [17] K. C. Ho and L. M. Vicente, "Sensor allocation for source localization with decoupled range and bearing estimation," *IEEE Trans. Signal Process.*, vol. 56, no. 12, pp. 5773–5789, Dec. 2008.
- [18] P. J. Rousseeuw and A. M. Leroy, *Robust Regression and Outlier Detection*, New York: John Wiley and Sons, 1987.
- [19] P. C. Mahalanobis, "On the generalised distance in statistics," *Proc. Nat. Inst. of Sci., India*, vol. 2, no. 1, pp. 49–55, Apr. 1936.
- [20] R. D. Cook, "Detection of influential observation in linear regression," *Technometrics*, vol. 19, no. 1, pp. 15–18, 1977.
- [21] J. S. Picard and A. J. Weiss, "Bounds on the Number of Identifiable Outliers in Source Localization by Linear Programming," *IEEE Trans. Signal Process.*, vol. 58, no. 5, pp. 2884–2895, May 2010.
- [22] M. McGuire, K. N. Plataniotis and A. N. Venetsanopoulos, "Data fusion of power and time measurements for mobile terminal location," *IEEE Trans. Mobile Computing*, vol. 4, no. 2, pp. 142–153, Apr 2005.
- [23] K. Yang, G. Wang and Z. Luo, "Efficient Convex relaxation methods for robust target localization by a sensor network using time differences of arrivals," *IEEE Trans. Signal Process.*, vol. 57, no. 7, pp. 2775–2784, July 2009.

- [24] K. H. Choi, W. Ra, J. B. Park and T. S. Yoon, "Compensated robust least-squares estimator for target localisation in sensor network using time difference of arrival measurements," *IET Signal Process.*, vol. 7, no. 8, pp. 664–673, Oct. 2013.
- [25] T. Arampatzis, J. Lygeros and S. Manesis, "A Survey of Applications of Wireless Sensors and Wireless Sensor Networks," in *Proc. MED*, Limassol, Cyprus, 2005.
- [26] N. Jin, R. Ma, Y. Lv, X. Lou and Q. Wei, "A novel design of water environment monitoring system based on WSN," in *Proc. ICCDA*, Qinhuangdao, June 2010.
- [27] M. A. Hussain, P. Khan and K. K. Sup, "WSN research activities for military application," in *Proc. ICACT*, Phoenix Park, Korea, Feb. 2009.
- [28] W. ying and W. Kaixi, "The building of logistics management system using RFID and WSN technology," in *Proc. ICSESS*, Beijing, China, June 2012.
- [29] I. F. Akyildiz, W. Su, Y. Sankarasubramaniam and E. Cayirci, "A survey on sensor networks," *IEEE Commun. Mag.*, vol. 40, no. 8, pp. 102–114, 2002.
- [30] Y. Wu, Q. Chaudhari and E. Serpedin, "Clock Synchronization of Wireless Sensor Networks," *IEEE Signal Process. Mag.*, vol. 28, no. 1, pp. 124–138, Jan. 2011.
- [31] H. Kopetz and W. Ochsenreiter, "Clock Synchronization in distributed real-time systems," *IEEE, Trans. Comput.*, vol. 36, no. 8, pp. 933–940, Aug. 1987.
- [32] V. K. Garg, *Wireless communication and networking*, San Francisco, CA: Elsevier, 2007.
- [33] T. A. Ngo, M. Tummala and J. C. McEachen, "Optimal wireless aerial sensor node positioning for randomly deployed planar collaborative beamforming," in *Proc. HICSS*, Hawaii, Jan. 2014.
- [34] G. C. Carter, "Variance bounds for passively locating an acoustic source with a symmetric line array," *J. Acoust. Soc. Am.*, vol. 62, pp. 922–926, Oct. 1977.
- [35] C. Meesookho, S. Narayanan and C. S. Raghavendra, "Collaborative classification applications in sensor networks," in *Proc. SAM*, Rosslyn, VA, Aug. 2002.

- [36] G. T. Sibley, M. H. Rahimi and G. Sukhatme, “Robomote: a tiny mobile robot platform for large-scale ad-hoc sensor networks,” in *Proc. ICRA*, Washington, DC, May 2002.
- [37] P. Martin, W. Etter and R. Mangharam, “Demo abstract: R.A.V.E.N. — Remote autonomous vehicle explorer network,” in *Proc. IPSN*, Chicago, IL, Apr. 2011.
- [38] R. Mahony, V. Kumar and P. Corke, “Multirotor aerial vehicles: modeling, estimation, and control of quadrotor,” *IEEE Robot. Automat. Mag.*, vol. 19, no. 3, pp. 20–32, Sept. 2012.
- [39] H. Lim, J. Park, D. Lee and H. J. Kim, “Build your own quadrotor: open-source projects on unmanned aerial vehicles,” *IEEE Robot. Automat. Mag.*, vol. 19, no. 3, pp. 33–45, Sept. 2012.
- [40] L. Meier, P. Tanskanen, F. Fraundorfer and M. Pollefeys, “PIXHAWK: A system for autonomous flight using onboard computer vision,” in *Proc. ICRA*, Shanghai, China, May 2011.
- [41] F. Fraundorfer, L. Heng, D. Honegger, G. H. Lee, L. Meier, P. Tanskanen and M. Pollefeys, “Vision-based autonomous mapping and exploration using a quadrotor MAV,” in *Proc. IROS*, Vilamoura, Portugal, Oct. 2012.
- [42] M. Schwager, B. J. Julian, M. Angermann and D. Rus, “Eyes in the sky: Decentralized control for the deployment of robotic camera networks,” *Proc. IEEE*, vol. 99, no. 9, pp. 1541–1561, Sept. 2011.
- [43] S. R. Santos, S. N. Givigi and C. L. Nascimento, “Autonomous construction of structures in a dynamic environment using Reinforcement Learning,” in *Proc. SysCon*, Orlando, FL, Apr. 2013.
- [44] E. Yanmaz, R. Kuschig and C. Bettstetter, “Channel measurements over 802.11a-based UAV-to-ground links,” in *Proc. GC Wkshps*, Houston, TX, Dec. 2011.
- [45] *Flying qualities of piloted aircraft MIL-STD-1797A*, Department of Defense, Washington, DC, June 1995.
- [46] R. Mahony, V. Kumar and P. Corke, “Multirotor aerial vehicles: modeling, estimation, and control of quadrotor,” *IEEE Robot. Automat. Mag.*, vol. 19, no. 3, pp. 20–32, Sep. 2012.

- [47] K. Alexis, G. Nikolakopoulos and A. Tzes, "Constrained-control of a quadrotor helicopter for trajectory tracking under wind-gust disturbances," in *Proc. MELECON*, Malta, Apr. 2010.
- [48] S. L. Waslander and C. Wang, "Wind disturbance estimation and rejection for quadrotor position control," in *Proc. AIAA Infotech Aerospace Conf.*, Seattle, WA, Apr. 2009.
- [49] I. Guvenc and C. Chong, "A survey on toa based wireless localization and nlos mitigation techniques," *IEEE Comm. Surv. and Tut.*, vol. 11, no. 3, pp. 107–124, 2009.
- [50] R. Yamasaki, A. Ogino, T. Tamaki, T. Uta, N. Matsuzawa and T. Kato, "TDOA location system for IEEE 802.11b WLAN," in *Proc. WCNC*, New Orleans, LA, 2005.
- [51] N. Patwari, J. N. Ash, S. Kyperountas, A. O. Hero, R. L. Moses and N. S. Correal, "Locating the nodes: cooperative localization in wireless sensor networks," *IEEE Signal Processing Mag.*, vol. 22, no. 4, pp. 54–69, July 2005.
- [52] D. J. Torrieri, "Statistical theory of passive location systems," *IEEE Trans. Aerosp. Electron. Syst.*, vol. 20, no. 2, pp. 183–198, Mar. 1984.
- [53] P. C. Chen, "A non-line-of-sight error mitigation algorithm in location estimation," in *Proc. WCNC*, New Orleans, LA, 1999.
- [54] S. Venkatesh and R. M. Buehrer, "A linear programming approach to NLOS error mitigation in sensor networks," in *Proc. IPSN*, Nashville, TN, 2006.
- [55] R. M. Bethea, B. S. Duran and T. L. Boullion, *Statistical Methods for Engineers and Scientists*, New York: Marcel Dekker Inc., 1995.
- [56] G. Strang, *Introduction to applied mathematics*, Wellesley, MA: Wellesley-Cambridge Press, 1986.
- [57] A. Bjorck, *Numerical Methods for Least-squares Problems*, Philadelphia: SIAM, 1996.
- [58] H. Cramér, *Mathematical Methods of Statistics*, Princeton, NJ: Princeton Univ. Press., 1946.

- [59] M. L. Boas, *Mathematical Methods in the Physical Sciences*, NJ: John Wiley and Sons, 2006.
- [60] R. O. Schmidt, "Multiple emitter location and signal parameter estimation," *IEEE Trans. Antennas Propag.*, vol. 34, no. 3, pp. 276–280, Mar. 1986.
- [61] M. M. Abdallah and H. C. Papadopoulos, "Beamforming algorithms for information relaying in wireless sensor networks," *IEEE Trans. Signal Process.*, vol. 56, no. 10, pp. 4772–4784, Oct. 2008.
- [62] R. Mudumbai, G. Barriac and U. Madhow, "On the feasibility of distributed beamforming in wireless networks," *IEEE Trans. Wireless Commun.*, vol. 6, no. 5, pp. 1754–1763, May 2007.
- [63] J. Litva and T. K. Lo, *Digital Beamforming in Wireless Communications*, MA: Artech House, 1996.
- [64] B. D. Steinberg, "Digital beamforming in ultrasound," *IEEE Trans. Ultrason. Ferroelectr. Freq. Control*, vol. 39, no. 6, pp. 716–721, Nov. 1992.
- [65] R. A. Soni, R. M. Buehrer and R. D. Benning, "Intelligent antenna system for cdma2000," *IEEE Signal Processing Mag.*, vol. 19, no. 4, pp. 54–67, July 2002.
- [66] C. Pan, J. Chen and J. Benesty, "Performance study of the MVDR beamformer as a function of the source incidence angle," *IEEE Trans. Speech Audio Process.*, vol. 22, no. 1, pp. 67–79, Jan. 2014.
- [67] M. Souden, J. Benesty and S. Affes, "A study of the LCMV and MVDR noise reduction filters," *IEEE Trans. Signal Process.*, vol. 58, no. 9, pp. 4925–4935, Sept. 2010.
- [68] E. L. Holzman, "A different perspective on taper efficiency for array antennas," *IEEE Trans. Antennas Propag.*, vol. 51, no. 10, pp. 2963–2967, Oct. 2003.
- [69] A. V. Oppenheim, R. W. Schaffer and J. R. Buck, *Discrete-Time Signal Processing*, Upper Saddle River, NJ: Prentice Hall, 1999.
- [70] S. J. Orfanidis, *Introduction to Signal Processing*, New York: Prentice Hall, 1996.
- [71] R. J. Mailloux, *Phased Array Antenna Handbook*, Boston, MA: Artech House, 1994.

- [72] A. Nuttall, "Generation of Dolph-Chebyshev weights via a fast fourier transform," *IEEE Process.*, vol. 62, no. 10, p. 1396, Oct. 1974.
- [73] J. F. Kaiser and R. W. Schafer, "On the use of the IO-sinh window for spectrum analysis," *IEEE Trans. Acoust., Speech, Signal Process.*, vol. 28, no. 1, pp. 105–107, Feb. 1980.
- [74] C. McCormack and R. Haupt, "Antenna pattern synthesis using partially tapered arrays," *IEEE Trans. Magn.*, vol. 27, no. 5, pp. 3902–3904, Sep. 1991.
- [75] F. J. Harris, "On the use of windows for harmonic analysis with the discrete Fourier transform," *IEEE Proc.*, vol. 66, no. 1, pp. 51–83, Jan. 1978.
- [76] B. Feng and D. C. Jenn, "Grating lobe suppression for distributed digital subarrays using virtual filling," *IEEE Antennas Wireless Propag. Lett.*, vol. 12, pp. 1323–1326, Oct. 2013.
- [77] T. K. Sarkar and O. Pereira, "Using the matrix pencil method to estimate the parameters of a sum of complex exponentials," *IEEE Antennas Propag. Mag.*, vol. 37, no. 1, pp. 48–55, Feb. 1995.
- [78] A. Satici, H. Poonawala and M. W. Spong, "Robust optimal control of quadrotor UAVs," *IEEE Access*, vol. 1, pp. 79–93, May 2013.
- [79] J. Abel and J. O. Smith, "Source range and depth estimation from multipath range difference measurements," *IEEE Trans. Acoust., Speech, Signal Process.*, vol. 37, no. 8, pp. 1157–1165, Aug. 1989.
- [80] H. C. Shau and A. Z. Robinson, "Passive source localization employing intersecting spherical surfaces from time-of-arrival differences," *IEEE. Trans. Acoust., Speech, Signal Processing*, Vols. ASSP-35, pp. 1223–1225, Aug. 1987.
- [81] K. Mardia, J. Kent and J. Bibby, *Multivariate Analysis*, New York: Academic Press, 1979.

- [82] J. W. Tukey, *Exploratory Data Analysis*, MA: Addison-Wesley, 1977.
- [83] P. S. Horn, L. Y. Li and A. Pesce, “Effect of outliers and nonhealthy individuals on reference interval estimation,” *Clinical Chemistry*, vol. 42, no. 12, pp. 2137–2145, 2001.
- [84] K. V. Mardia, *Statistics of Directional Data*, New York: Academic Press, 1972.
- [85] T. T. Ha, *Theory and Design of Digital Communication Systems*, Cambridge, UK: Cambridge University Press, 2011.
- [86] C. W. Therrien and M. Tummala, *Probability and Random Process for Electrical and Computer Engineers*, Boca Raton, FL: CRC Press, 2012.
- [87] K. Lange, *Applied Probability*, New York: Springer Science+Business Media, 2010.

## **INITIAL DISTRIBUTION LIST**

1. Defense Technical Information Center  
Ft. Belvoir, Virginia
2. Dudley Knox Library  
Naval Postgraduate School  
Monterey, California